UCC

University College Cork, Ireland
Coláiste na hOllscoile Corcaigh

# Biosensors Using Photonic Crystal Fibres

*Monika Sylwia Rutowska*

Thesis submitted for the degree of Doctor of Philosophy

National University of Ireland, Cork
Department of Physics
Tyndall National Institute, Photonics Systems Group

**February 2014**

*Head of Department: Prof. John McInerney*
*Supervisors: Dr. Fatima Cristina Garcia Gunning and Prof. Andrew Ellis*

# Contents

i

# Declaration

This thesis is a presentation of my original research work. Wherever contributions of others are involved, every effort is made to indicate this clearly, with due reference to the literature, and acknowledgement of collaborative research and discussions.

Monika Sylwia Rutowska

# Acknowledgements

I would like to thank to my supervisor Dr. Fatima Cristina Garcia Gunning, for offering me the opportunity to research this project. Especially I want to thank to my co-supervisor Prof. Andrew Ellis, who always found time for helpful discussions, thesis reviewing and his support during this PhD project. Many thanks to all members of Photonics Systems Group. I am grateful to Prof. Wacław Urbańczyk, from the University of Technology in Wrocław, Poland for lots of discussion and support.

Thank you to all of the people in Tyndall National Institute in Cork, Ireland for the fantastic atmosphere and first-class opportunity for realisation of this research project. Particularly, I want to thank to my friends Dr. Patrycja (*nee* Heinrich) Niewosz for invaluable help during my PhD, and to Dr. Jarosław Pulka and Dr. Laura Horan. Special thanks to my friend Dr. Pouneh Saffari for a fantastic support and *k.a.* at the last steps of the PhD.

The realization of this project would not have been possible without the financial support of Science Foundation Ireland (grant number 06/IN/I969), and I wish to thank the following companies: The OakWood (Marcin Rutowski, Ireland) and Compuserv GmbH (Andrzej Jawurek, Germany) for financial support and IT equipments.

And, now I would like to thank to my Internal Examiner Dr. Frank Peters and External Examiner Prof. Jonathan Knight for all their work and help with the PhD thesis defence.

I am happy to thank my family: Maja and Marcin for always believing in me and being with me every day. Dziękuje.

*I would like to dedicated this PhD thesis to the memory of my grandmother.*

# Publications

## Patent Application

- <u>M. Rutowska</u>, L. Horan, G. Khara and F.C. Garcia Gunning,
  *"Nanoscale Viscometer Device"*, University College Cork, Ireland, UK 1104547.3,
  Applied: 18th of March 2011

## Journal Papers

- <u>M.S. Rutowska</u>, F. Kivlehan, E. Moore, D. Brennan, P. Galvin, and F. C. Garcia
  Gunning
  *"Integration of 3D hydrogel matrix within a hollow core photonic crystal fibre
  for DNA immobilization"*, Measurement and Science Technology, vol. 21,
  no.094016, 8pp, 2010

## Conference Papers

- <u>M. Rutowska</u>, L. Horan, and F.C. Garcia Gunning
  *"Photonic Crystal Fibres: Selective Filling Delays."*, Proceedings of IEEE,
  European Conference on Lasers and Electro-Optics (CLEO), Munich, Germany,
  2009 paper:CH3

- <u>M. Rutowska</u>, L. Horan, and F.C. Garcia Gunning,
  *"Photonic Crystal Fibres: Selective Filling Delays"*, Photonics Ireland, Kinsale,
  Ireland, 2009

- <u>M. Rutowska</u>, F. Kivlehan, E. Moore, D. Brennan, P. Galvin, and F.C. Garcia
  Gunning
  *"DNA immobilisation within 3D hydrogel matrix in Hollow-Core Photonic Crys-
  tal Fibre"*, Proceedings of SPIE, 20th Conference on Optical Fiber Sensors,
  Edinborough, UK, 2009, vol. 7503, paper: PDP 08

- <u>M. Rutowska</u>, P. Galvin, and F.C. Garcia Gunning,
  *"Optical Properties of Hydrogel-Filled Hollow Core Photonic Crystal Fibres"*,
  Proceedings of SPIE, 4th European Workshop on Optical Fibre Sensor, Porto,
  Portugal, 2010, vol:7653, paper: 76531P-4

- <u>M. Rutowska</u>, J. Lu, F.C. Garcia Gunning, and A.D. Ellis
  *"DNA Probe Detection within 3D Hydrogel Matrix in a Hollow-Core Photonic Crystal Fibre"*, Proceedings of SPIE, 21st Conference on Optical Fiber Sensors, Ottawa, Canada, 2011, vol.7753, paper: 7753-417

- <u>M. Rutowska</u>, F.C. Garcia Gunning, W. Urbańczyk, A.D. Ellis,
  *"DNA Immobilisation and Hydrogel Matrix Formation in Suspended-Core Optical Fibre"*, Proceedings of IEEE, European Conference on Lasers and Electro-Optics (CLEO), 2011, Munich, Germany, paper: CH4-2

- L. Horan, G. Khara, <u>M. Rutowska</u>, A.D. Ellis, and F.C. Garcia Gunning,
  *"Potential glucose monitoring of blood plasma using hollow core photonic crystal fibre"*, Proceedings of SPIE, 21st Conference on Optical Fiber Sensors, Ottawa, Canada, 2011, vol.7753, paper: 7753-177

# Abstract

In this thesis, we present the unique properties of hollow-core photonic crystal fibres (HC-PCFs) for sensing applications in terms of viscosity detection and DNA sensing using a special poly(ethylene) glycol (PEGDA) hydrogel. The low loss HC-PCFs ensure a long interaction length between the sample and the optical signals. Thus in this thesis, we report the characterisation of filled HC-PCFs and the development of a selective filling process. For the first time, we report the investigation of a new viscometer device, and a new device for DNA sensing development, and also the chemical process for hydrogel growth was adapted to the fibres. By combining HC-PCFs with the hydrogel we enable 3D volumetric sample confinement within the HC-PCF, further increasing the interaction between the sample and the optical signal. However, the hydrogel has a large influence on the guidance properties of the HC-PCF and the HC-PCF has a strong influence on the growth process for the hydrogel itself. When we integrate the hydrogel and HC-PCFs we detect concentration levels as low as 400 $nM$ of labelled DNA. However, using our technology for fluorescence detection we can achieve results two orders of magnitude better than those previously reported.

# Introduction

## 1.1 Motivation

Photonic crystal fibres (PCFs) belong to a group of optical fibres which are characterised by their unique, periodic structure, in which air channels in the cladding run through the length of the fibre. They can be called microstructured fibres or holey fibres, but despite the difference in terminology, they all refer to the same fibre type. These fibres were first proposed in 1991 by P. St. Russell in his notebook and published by T. Birks et al. in *Electronic Letters* in 1995 [1]. Owing to their specific geometry, PCFs have been used for a number of new applications and have generated many active research areas in the field of photonics. One interesting example presented in this thesis, is the generation of the supercontinuum signal. Using a highly-nonlinear PCF (HNL-PCF), a broad spectrum is generated within the fibre thanks to the collective action of several nonlinear effects. Unlike standard optical fibres, light can be propagated with a modified index-guiding or photonic bandgap (PBG) effect. In the first case, light is confined within the core of the fibre which has a higher refractive index material compared to the surrounding microstructure cladding. In the second case, owing to the geometry of the fibre, it is possible to confine light within the core of the fibre. The core has a lower refractive index than the cladding allowing only certain wavelengths to be propagated in a PBG [2–6]. In this thesis we investigate a hollow-core PCF (HC-PCF), which was first proposed in 1998 [1, 7–10]. The HC-PCF has a large, air channel at its centre, which is the fibres core, and is surrounded by the microstructure cladding. Since light can be guided in air using a PBG, this fibre is characterised by an anomalous dispersion and high power signal transmission with low attenuation.

One research topic, that has been widely studied in recent years is the use of PCFs for sensing. It is facilitated by filling the air-capillaries of PCFs by a specimen [10, 11]. The insertion of the sample into the fibre allows the enhancement of light-matter interaction. However, it depends on the refractive index of the sample, which cannot be greater than the refractive index of the fibre material (i.e. glass). An advantage of such a system is that the fibre length can be adjusted from a few centimetres to tens

of centimetres increasing the light-matter interaction and sensitivity [12, 13]. In addition, it was shown that the sample introduced to the structure of PCFs may be in either gas or liquid state [2, 11–18]. Owing to the microscopic-size of the capillaries of the PCF structure and the commonly used lengths being 10 *cm* to 40 *cm*, only nano-litre volumes of samples are required. One of the first liquid-filled fibres was presented in 2003, when a solid core PCF was filled with a liquid-crystal to implement a novel optical switch [3]. As well, the immobilisation of DNA within the capillaries of PCF was presented, where spectroscopy techniques were used to verify the presence of the DNA in aqueous solution [12]. This approach was further extended to detect the presence of antibodies and proteins. However, such specificity can be achieved not only in bio-detection, but can be extended to controlling particle levitation, refractive index measurements, viscosity, etc. More examples can be found in [6, 19–31].

In this thesis we report two developments of a new sensor using a HC-PCF for viscosity measurements and DNA detection for the first time. A new viscometer device is proposed, and it is based on recording the filling time of a certain length of the fibre with a liquid sample. Knowing the viscosity of liquids is essential for fluid analysis [32]. In the chemical and manufacturing industry, for example, constant control of viscous parameters of fluids is required. Investigation has shown that monitoring viscosity of bodily fluids is essential in medicine. Viscosity analysis determines internal body implications, surgery complications, and diseases at a cellular level [33–37]. For instance, the monitoring of such changes of viscosity in blood is required during cardio-vascular surgery [38, 39]. Other examples are a monitoring of viscosity are necessary in urology, neurology (cerebrospinal fluid) [33], and ophthalmology (tear film lipid layer) [34, 40, 41].

Commonly available viscometers are designed to analyse and control the viscosity of fluids in production lines, and are quite large, requiring complex analysis of the fluids. An example of a simple viscometer is a capillary viscometer [42]. It was one of the first methods utilized for analysis of the fluid's viscosity based on the Lucas-Washburn model [43]. A glass capillary is filled with a sample without any external pressure and the movement of the meniscus is observed. The capillary length and the time of meniscus travel determines the viscosity. However, the density and surface tension of the fluid are required to determine viscosity accurately. One drawback of using this type of viscometer is that the viscosity of the sample cannot be controlled *in-vivo*. The proposed here the fibre viscometer could be useful for monitoring viscosity of nano-litre samples, in horizontal and vertical positions in a very short period of time, perhaps a few seconds. The time detection set-up could be improved in comparison to standard techniques by connecting the fibre to a light source and using special optical detectors. The optical detectors could monitor the filling time due to changes in the fibre during the filling process. The proposed viscometer could provide high

precision measurements, have a small size and light weight due to the size of the HC-PCF. Therefore it may be integrated with medical equipment to control the viscosity of bodily fluids and in point-of-care methods [44].

In the case of DNA detection proposed here, a labelled DNA probe is immobilised in a gel that volumetrically fills the channels of HC-PCFs, instead of only coverage of the inner surface [45, 46]. The main reason the hydrogel was chosen was for its ability to be chemically attached to the silica surface and its a three-dimensional matrix growth structure. This biomaterial was specially design to enclose (i.e. immobilise) biomolecules inside its structure. In comparison to two-dimensional surface coverage, there may be one hundred times more biomolecules *per* unit volume [47–49]. It may therefore be a highly sensitive device. The hydrogel was characterised as a material with a good hydrophilic character, stable with controllable growth. By encapsulating DNA within its porous structure, it is considered to be a special medium for DNA molecules [50–52]. In addition, this hydrogel was developed not only for DNA probe immobilisation, but also the hydrogel has a unique property to select DNA probes known as DNA hybridisation. This, in short, entails selecting and matching DNA strands in order to identify mutations and diagnose genetic diseases.

DNA probe immobilisation and hybridisation within the hydrogel on microchips have been studied since the 1980s. In such tests, microchips contained 64 elements of the hydrogel with a size of $40 \times 40 \times 20 \ \mu m$ [48, 49]. Labelled DNA immobilisation was tested with the assistance of an epi-fluorescence microscope by scanning the entire chip surface. The tested sample volume was $64 \times 32 \ pL$ which equals approximately $2 \ nL$.

The integration of the hydrogel with the HC-PCF is therefore proposed here, as an alternative to microchips. Taking into consideration its core size (of $\approx 5 \ \mu m$ radius) and an average length of $\approx 10 \ cm$, the hydrogel volume could be close to $7 \ nL$. Compare this to 2D microchips, the number of DNA probe molecules attached to the hydrogel, in this case, could increase by at least 3 times due to its volumetric nature. As well, the process of scribing the gel sample (i.e. preparing the gel to be placed on the chip surface) as described in paper [49] would not be necessary, reducing the growth complexity. Here we propose the unique technique to grow the hydrogel directly inside the fibre. This process may be possible by polymerising the hydrogel by light propagation through the fibre. In this case, the fibre must be filled with a pre-polymer solution, and then polymerised into the hydrogel. However, the most important aspect of insertion the sample into HC-PCFs is the significant change of its light guidance properties. The most important is the change in the refractive index within the fibre channels, which affects the light guidance by a blue-shifting the bandgap. The optical field can still propagate through the core (under certain conditions analysed in Chapter 2), and these new wavelengths may be used to excite well-known fluorochromes

(or fluorescent tags), and detect labelled DNA probes. In addition, the fibre can be integrated with an optical device such as a laser and sensitive optical detectors. Also, as was described for the viscometer device, a new DNA sensor can have a small dimension and light weight due to HC-PCFs dimension. Considering here the optical advantages of HC-PCFs and the properties of the highly sensitive hydrogel, we propose a new point-of-care DNA device.

## 1.2 Overview

To give the reader an overview of the thesis, the following is a review of the highlights of each chapter:

**Chapter 2:**

This chapter gives the background to the development of new sensors using HC-PCFs. First, the HC-PCF is presented and the light propagation mechanism is explained. In order to propose HC-PCFs as the viscometer device, we present in this chapter, the physics of filling the fibre with a liquid sample. For the DNA sensor, first we define and present the hydrogel, including the theory of chemical process of growing the hydrogel. Finally, the DNA probe is described with an explanation of the luminescence process at the molecular level.

**Chapter 3:**

In this chapter, the theory of light propagation in HC-PCFs is supported with numerical modelling using a finite element method. In addition, three scenarios of refractive index contrast presenting spectral profiles in the fibre are investigated. Finally, an experimental demonstration is shown, using the supercontinuum sample. Here, we also investigate the optical modes for three of the modeled scenarios, using a numerical model and near-field imaging observation.

**Chapter 4:**

Here we present a novel application of a nano-litre fibre viscometer using the HC-PCF. This is introduced with an experimental presentation of the filling process of HC-PCFs including an analysis of selective filling techniques. Also, the filling of the fibre with and without the use of external overpressure is described.

**Chapter 5:**

In this chapter, hydrogel morphology and the complete process of integration of the hydrogel with HC-PCFs is demonstrated. This is followed by an analysis of the hydrogel distribution along the fibre length.

**Chapter 6:**

In order to develop a sensitive optical device for labelled-DNA probe detection, the optical properties of the hydrogel such as the refractive index and attenuation are verified here. The transmission spectrum with near-field images of the fibre with the hydrogel and water are then compared and analysed.

**Chapter 7:**

In this chapter, we show the fluorescence detection for the fibre selectively filled with Alexa-750 aqueous solution, where we try to achieve a minimal concentration detection of nanoMol/litre using the supercontinuum light source. As a proof of concept, Cy-5 DNA probe immobilised in the hydrogel with the hydrogel grown inside the fibre is demonstrated for the first time. Then the Cy-5 DNA probe immobilised in the hydrogel grown within HC-PCF is detected in terms of using various DNA concentrations for the fibre with a length of about 10 *cm*.

**Chapter 8:**

Considering the fact that the hydrogel has a stronger attenuation than water, it is required to improve the hydrogel distribution along the fibre length. This technique was further explored for implementation within suspended-core optical fibre. In this case, the evanescent field interacts with the hydrogel. Nevertheless, a broadband light is propagated through its solid core with lower loss, while still enabling DNA-probe immobilisation and detection. Herein, the suspended-core optical fibre is characterised with numerical modeling and transmission spectra. The integration of this fibre and the hydrogel is also presented, with DNA immobilised within the hydrogel.

**Chapter 9:**

This is the final chapter of the thesis and contains the conclusions for developing HC-PCFs as a viscometer and DNA probe detection device. A plan for possible future work is outlined here.

# Background

## 2.1 Introduction

The chapter begins with a presentation of the fundamental properties of HC-PCFs. Its structural properties and optical guidance model are demonstrated using geometrical representations with an accompanying physical explanation. The study continues with an analysis of the consequences of the refractive index variations within the fibre. The theoretical introduction is followed by a discussion of the optical changes of a filled fibre in terms of its use as a sensor. Next, the theoretical background for capillary filling and the fluid parameters that affect the filling process are described. Finally, the hydrogel is introduced with a description of chemical structure along with a chemical procedure for hydrogel growth. At the end of this chapter, biomolecule detection techniques such as fluorescence and phosphorescence are explained.

## 2.2 Fundamental properties for HC-PCFs
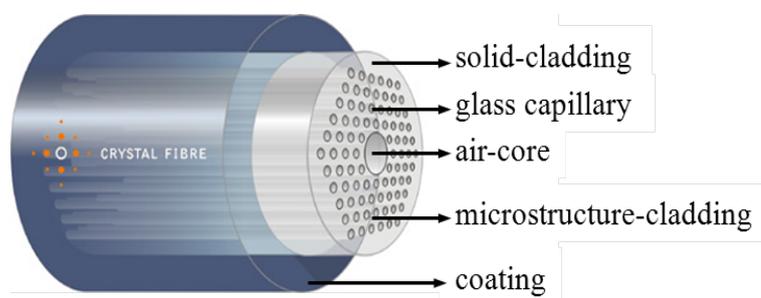
### 2.2.1 Geometry and fabrication



Figure 2.1: *Holey fibre, courtesy of NKT Photonics A/S*

Fig.2.1 shows a 3D representation of a *holey* fibre. The fibre has three main layers. The first layer (outer) is the solid cladding. It can be formed using fused silica, bismuth glass, or soft glasses such as oxides, fluorides, chalcogenides and lead-silicate

[25, 53, 54]. The second layer of the cladding is called the microstructure cladding, as it contains numerous glass capillaries (channels). The glass region between each channel is called the bridge.



Figure 2.2: *The scheme of the fibre structure, where the pitch is shown for a) solid-core and b) air-core fibre*

The distance between the centre of one air hole to the centre of another is called the pitch ($\Lambda$) [55], as illustrated in Fig.2.2. The centre of the fibre is the core. This can either be a solid centre, as shown in Fig.2.2a, or an air-filled capillary demonstrated in Fig.2.2b.



Figure 2.3: *Schematic illustration of PCFs fabrication process, courtesy of NKT Photonics A/S*

A detailed fabrication process is described elsewhere [56]. Fig.2.3 shows the overall schematic of the procedure. The glass rod and capillaries are positioned into a preform. The preform is then heated to high temperatures (shown within the heating zone in Fig.2.3) and is pulled out into the fibre spool [13, 55, 57, 58]. The final product (fibre) has micro-size diameter capillaries running along the entire length. The pulling process deforms the original shape of each glass tube. This leads to a shape closer to a hexagon with curved corners rather than a circle. For a HC-PCF, the core is formed during the fabrication process by removing seven or nine glass tubes (cells) from the centre of the preform [59]. It is simply an additional larger air-channel within the fibre structure.

## 2.2.2   Light guidance properties

In order to understand the physical model behind the light propagation mechanism in HC-PCFs, where it is said that light is guided due to the PBG effect, we analyse following scheme (Fig.2.4).



Figure 2.4: *Schematic drawing of optical rays' path in the hollow-core PCF, where rays with a navy blue colour indicate wavelengths, which are not propagated in the air-core (resonant wavelengths), and the wavelengths which propagate within the core (red rays) (antiresonant wavelengths)*

Fig.2.4 shows a representation of the light propagation in a hollow-core PCF. The two dimensional fibre cross-section is composed by a multilayered stack of silica glass ($n_{silica} = 1.45$) and air ($n_{air} = 1.00$). The refractive index profile is shown on the left-side of Fig.2.4 (green lines). On the right-side of Fig.2.4 are marked: the fibre core with diameter ($D_{core}$) and the silica layer surrounding the core ($d_{sur}$). Also there are the silic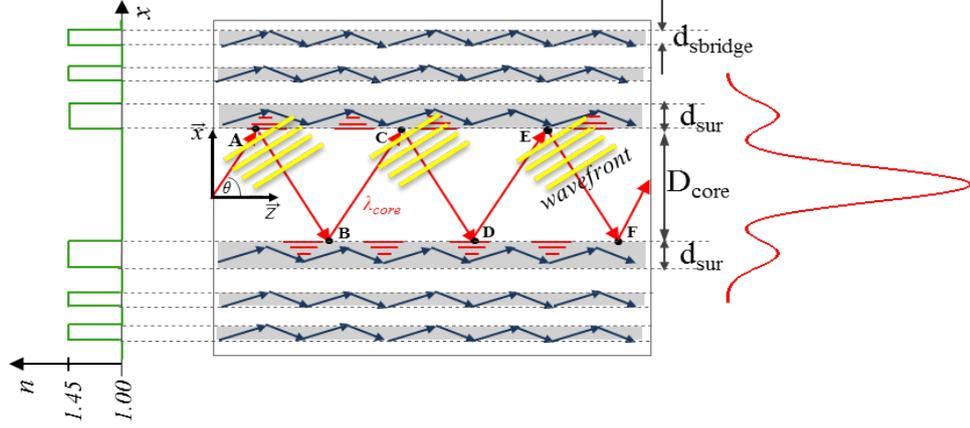a layers in the cladding ($d_{sbridge}$). However, these ones have a different thickness in comparison to $d_{sur}$. By illustration, we considered an optical ray (red ray) launched at certain degree ($\theta$) (i.e. the angle of incidence) from the *z-axis*. A certain wavelength ($\lambda_{core}$) propagates through the core along the fibre in the low-index material, in this case air with a propagation constant ($\beta$). $\beta$ is defined as the wavevector in the *z-axis* ($\vec{k_z}$) and equals $\beta = k \cdot n_{core} \cdot \sin\theta$ with $n_{core}$ being the refractive index of the core. The multilayered stack of silica and air act as a highly reflective dielectric mirror. Hence, the core of the fibre is surrounded by a curved reflecting surface, and the fibre as a whole may be regarded as a *mirror tube*. Inside the mirror tube is a medium, in this case air. For this particular example we can say that this mirror resembles a Fabry-Perot resonator [60, 61]. In order to create such a glass resonator for a particular wavelength, for example $\lambda_{core}$, the internal diameter of the *mirror tube* has to be several times greater then the $\lambda_{core}$. In addition, the radius of the *mirror tube* has to match to the wavefront of $\lambda_{core}$. Determining the path length within the fibre core as A-

B-C-D... points in Fig.2.4, $\lambda_{core}$ reflects from one of the mirror boundaries (say, at "A"). It propagates to the other boundary ("B") and is reflected again, and so forth. The wavefront (straight yellow lines) associated with the ray A-B must constructively interfere with the wavefront associated with the ray C-D. This means that the phase difference between the parallel rays at the same vertical points (B and D) must be an integer multiple of $2\pi$, and hence satisfy following condition [61]:

$$\delta = 2 \cdot n_{core} \cdot k_0 \cdot D_{core} \cdot \cos\theta = 2\pi N \tag{2.1}$$

with $k_0$ is a free space wave number ($k_0 = \frac{2\pi}{\lambda}$), and $N$ the order of the interference. Then, $\lambda_{core}$ has its maximum intensity in the fibre core, and create an optical mode profile as this shown in the right-panel of Fig.2.4. In Fig.2.4 we can also observe that $\lambda_{core}$ also leaks into the resonator walls. According to [60], it was calculated that the thickness of the resonator wall ($d_{sur}$) is crucial in terms of guiding the $\lambda_{core}$ along the air-core. Analysing only the fibre core ($D_{core}$) with the refractive index ($n_{core} = 1.00$) and the glass layer surrounding the core with $n_{sur} = 1.45$ we may estimate the $\lambda_{core}$ and $d_{sur}$. Taking into calculations the modal cut-off conditions for the waveguide with high and low refractive index material layers, which support the optical modes, the $\lambda_{core}$ can be represented by Equation [62, 63, 66]:

$$\lambda_{core} = \frac{2d_{sur}}{N} \cdot \sqrt{n_{silica}^2 - 1} \tag{2.2}$$

However, this condition is valid only for $\frac{\lambda_{core}}{D_{core}} << 1$.

The $\lambda_{core}$ interfere destructively within the resonator walls [63, 64], and a low loss guidance along the fibre core is affected by the thickness of $d_{sur}$ and its refractive index. As an example, the fibre designated HC-PCF 1060 guides a signal at a wavelength 1060 $nm$ along its air-core. In order to estimate $d_{sur}$ for the fibre HC-PCF 1060, $N = 1$ (i.e. for the first, resonance order), the fibre core diameter $D_{core} = 9.8$ $\mu m$ with the silica of the refractive index $n_{silica} = 1.45$ are taken into calculations. According to these parameters and Equation 2.2, $d_{sur}$ should be thick as 0.5 $\mu m$.

The presence of the microstructure cladding such as high-index cladding layers $d_{sbridge}$ separated also by low-index medium can be attributed to anti-resonant reflecting optical waveguide (ARROW) [62, 63, 65–70]. Clearly, wavelengths which do not interfere destructively in the resonator walls will be not as strongly guided in the air-core as those which do, and may propagate in the cladding layers. In Fig.2.4 we can see, that some blue rays are present in the silica layer ($d_{sbridge}$) of the microstructure cladding. These wavelengths are called *resonant wavelengths*, and have a minimum intensity in the low-index core. However, the $\lambda_{core}$, which satisfies Equation 2.2 is called *antiresonant wavelength*. In addition, it can be also considered that each layer of high-index

cladding layers form also the Fabry-Perot resonators. Here, light should not be propagated along air in the cladding capillaries due to their small diameter ($d_h \approx 2\ \mu m$). However, the number of layers is also a crucial factor for the transmission loss of the antiresonant wavelength. The transmission loss decreases by increasing the number of the cladding layers.

Here, we define an *effective index* ($n_{eff}$) for such a fibre (HC-PCF), as a ratio of the propagation constant ($\beta$, defined in Fig.2.4) to the free space wave number:

$$n_{eff} = \frac{\beta}{k_0} \tag{2.3}$$

Hence, considering the constant propagation ($\beta$) Equation 2.3 gives:

$$n_{eff} = n_{core} \cdot \sin\theta \tag{2.4}$$

If we assumed, the refractive index of air-core as ($n_{core} = 1.00$), then:

$$n_{eff} = \sin\theta \tag{2.5}$$

In this case, the effective index of optical modes is always lower than unity ($n_{eff} < 1.00$) for the incident angle $\theta < 90°$. Note that, even if the core of the fibre is not an air-core, but with a refractive index ($n_{core} > 1$), the $n_{eff}$ would be always lower than $n_{core}$ and light would still propagate [71].

One more important parameter to describe the HC-PCF structure should be referred to here. It is an *air-filling fraction (aff)*. It describes the ratio of the low-index capillary area to the high-index rod area, with a $d_h$ as the capillary hole diameter [56]:

$$aff = \frac{\pi}{2\sqrt{3}} \frac{d_h^2}{\Lambda^2} \tag{2.6}$$

It is worth noting here, that using the *aff* parameter we can reconstruct the microstructure cladding structure. In order to achieve guidance in the air-core the *aff* parameter (Equation 2.6) has to be proportionally high, which is related to a ratio: ($\frac{d_h}{\Lambda}$).

Referring to prior publications, we know that light is confined in the air-core due to the PBG effect. However, in this section we describe the light mechanism as ARROW. It has to be explained here, that the fibre microstructure cladding resembles a two-dimensional (2D) photonic crystal [7, 10, 68]. The primitive cell for the fibre is a hole area (low-index cylinders) surrounded by rod area (high-index materials). They can create a triangular, square, honeycomb, hexagonal, or *kagome* lattice [54, 56, 73]. Here, it is necessary to refer that the photonic crystals create within their propagation profile a *forbidden band* so called a *photonic bandgap* (PBG) [56, 74–76]. The PBG should be regarded as a stop band for the propagation constant [74]. When the photonic

crystal structure is *broken* at some point, a certain wavelength within the PBG appears. These wavelengths are allowed to be propagated within the PBG region [74]. For this reason, it is concerned that the fibre microstructure cladding forms a PBG, too. Introducing the larger hole at the centre of the fibre, which is the fibre core breaks the cladding periodicity. It holds light at a certain wavelength within the bandgap [55, 68, 77–81]. In our case, to maintain the propagation of light along the PCF in the *z*-axis (i.e. along the fibre), the refractive index contrast within the microstructure cladding can be low in comparison to propagation through photonic crystals materials [56, 65]. During numerous calculations, it also was found that the guidance along the fibre requires a number of air-channels repeated only transversely. A strict periodicity is not necessary [67, 82]. Nevertheless, we can assume that the guidance phenomena in the low-index core depends on the geometry of the cladding and the core [10, 56, 58]. However, a full understanding of light guidance within the HC-PCFs requires an analysis of the band diagram described elsewhere [72].

In this thesis, we adapted the terminology described in the literature. We define the antiresonant wavelength as the wavelength which is guided due to the PBG effect. In Chapter 3 we investigate numerically and experimentally the spectral profile (i.e. the band diagram) for the HC-PCF, with a discussion of field patterns for this fibre.

### 2.2.3 HC-PCFs as a sensor

The introduction of a material into the air-channels of PCFs induces changes to the refractive index contrast, which causes waveguide propagation changes. This has been previously studied for fluid filled fibres [17, 82, 83] and we here review the results of these studies in this section.

**Impact of changing refractive index**

In order to investigate the influence of the refractive index changes within the fibre, there are two scenarios to analyse. The first case involves a change of the refractive index in the core and the microstructure cladding. In this scenario, the light is still guided by the PBG. The bandgap is shifted to a new wavelength region. The shift may be calculated by the scaling equation [82, 83]:

$$\lambda_s = \lambda_0 \sqrt{\frac{1 - \left(\frac{n_g}{n_m}\right)^{-2}}{1 - \left(\frac{n_g}{n_a}\right)^{-2}}} \qquad (2.7)$$

where $\lambda_s$ is the shifted wavelength, $\lambda_0$ indicates the main bandgap wavelength, $n_g$ is the refractive index of the fibre material (glass), $n_m$ is the refractive index of a new filling material, and $n_a$ is the refractive index of a previous filling (for example air).



Figure 2.5: *Graph of photonic bandgap shift guidance in HC-PCFs, due to changes in the refractive index within the fibre*

Fig.2.5 shows the wavelength shifts ($\lambda_s$) depending on the refractive index of the filling material for a fibre sample HC-PCF 1060.



Figure 2.6: *Graph of index-guiding, with a green line indicating a core-mode guidance within the region between the water index and the total-internal reflections (TIR) edge - shown with black-dashed lines. The blue lines (in the dark area) illustrate the guidance in the fibre cladding, courtesy of [17]*

The second scenario involves a change to the refractive index only in the fibre core. If the refractive index of the core is sufficiently high in comparison to the refractive

index of the surrounding cladding, light guidance is dominated by an index-guiding mechanism [17, 56]. Instead of propagating a certain wavelength in the core of the fibre we may expect a broad range of wavelengths can be guided [17]. Fig.2.6 shows a reproduction of a theoretical model of the HC-PCF with the following parameters: $\Lambda = 0.9\ \mu m$, $d_{claddinghole} = 0.648\ \mu m$ and the core diameter $D_{core} = 2.35\ \mu m$ with the refractive index changed to 1.33 only in the core of the fibre, as analysed by [17]. Similar to the described analysis for the air-core (see Equation 2.3) where $n_{eff} = n_{core} \times \sin\theta$, and that $n_{core} = n_{water}(\approx 1.33)$, $n_{eff}$ as in Equation 2.4 will be, in this case, less or equal to $n_{water}$. For this reason, the propagation along the core is limited by the water line index (black dashed line). The light propagates with an optical mode observed only within the fibre core (*core modes*), as indicated by the green line. The dashed yellow line presents an analytical mode-line estimated using equations from [17, 84]. However, the transmission window is also limited by a black dashed line indicating the total-internal reflections (TIR) line. There is no light confinement in the fibre core, but only in the fibre cladding (blue solid lines).

**Light attenuation**

In this section, we investigate light attenuation caused by guiding light within the medium according to Beer-Lambert's law
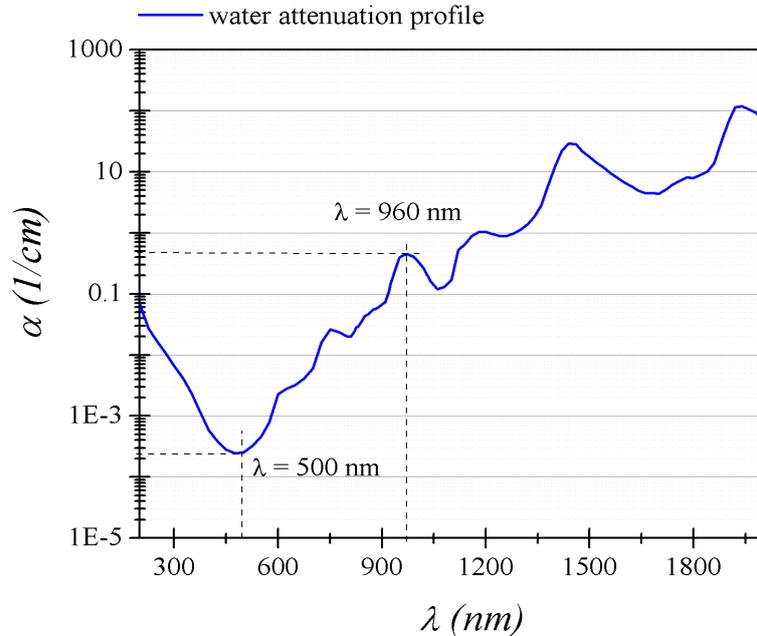


Figure 2.7: *The water attenuation profile adapted from reference [86]*

The attenuation of an incident beam of intensity $I_0$ at wavelength $\lambda$ shows an exponen-

tial decay whereby the output intensity $I$ is given [71, 85]:

$$I = I_0 e^{-\alpha L} \tag{2.8}$$

where $\alpha$ is a linear attenuation coefficient, and $L$ indicates length of interaction light and sample. In order to illustrate the impact of the attenuation coefficient and the decay of light intensity travelling through an absorbing medium, the water attenuation profile was chosen as an example.

Fig.2.7 presents the attenuation coefficient ($\alpha$ ($1/cm$)) as a function of wavelength in the range of wavelengths from 200 $nm$ to 2 $\mu m$ adapted from [86]. Analysing this water profile, it can be observed, that minimal water attenuation occurs at the visible range and increases in the near-infrared wavelengths region. As an example, Equation 2.8 suggests that the output intensity at $\lambda \approx 500$ $nm$ ($\alpha \approx 0.0002$) decreases by 2.5% after 1 $m$ propagation along the water, and at 960 $nm$, where the attenuation is appreciably higher ($\alpha \approx 0.4200$) the intensity decreases by 34% after propagation through only 1 $cm$ of water.

However, the reduced ratio of light signal guided through the medium can also be expressed with an absorbance *(A)* which equals:

$$I = I_0 \cdot 10^{-A} \text{ then } A = log_{10}(\frac{I_0}{I}) \tag{2.9}$$

where $A$ is the absorbance. In order to find the relation to the $\alpha$ linear attenuation coefficient, the absorbance of both equations are equalised (2.8 and 2.9):

$$A = L \cdot \log e^{\alpha} \tag{2.10}$$
$$A = 2.302\alpha \tag{2.11}$$
$$\alpha = \frac{A}{2.302} \tag{2.12}$$

In the case, where the signal travels through a solution (i.e. chemical species) rather than a pure liquid, we can calculate its attenuation using absorbance and a *molar extinction coefficient ($\phi$) [$M^{-1}cm^{-1}$]*. This parameter describes the ability of chemical species to absorb the light with respect to the interaction length and concentration. Then, the absorbance of the solution equals:

$$A = \phi \cdot L \cdot C \tag{2.13}$$

where $C$ is the concentration of the solution. Then, we may estimate the attenuation of this solution by combining above discussed equations:

$$I = I_0 e^{-\frac{\phi \cdot C}{2.302} \cdot L} \tag{2.14}$$

Note here, that in this thesis, we are only focused on calculating light attenuation caused by introducing an absorbing material. Any other losses such as signal dispersion, signal scattering etc. are neglected due to the fact that the fibre length is always as short as $10 - 30$ *cm* and the fibre was kept straight for all measurements.

## 2.3   Theory of fibre filling process

In order to explain the PCFs filling process, we use the explanation of the filling process of an arbitrary cylindrical glass capillary. This process can be described by a set of parameters dictated by flow characterisation. Fig.2.8 displays the flow characterisation and Fig.2.9 required parameters for the description of the filling process.



Figure 2.8: *The schematic of fluid flow characterisation*

As we can see in the left-panel (Fig.2.8), the first parameter which describes the flow is Reynold's number (*Re*). *Re* is given by: [87–89]

$$Re = \frac{2rv\rho}{\mu_d} \tag{2.15}$$

where *r* is a capillary radius, *v* is velocity, $\rho$ is the fluid density, and $\mu_d$ is dynamic viscosity. Here the viscosity is defined as a flow property and can be called *dynamic viscosity* ($\mu_d$), or *viscosity* ($\mu$), or *absolute viscosity* ($\mu$) *[Pa · s]*. All three terms describes for a liquid the ratio of shear stress to shear rate [89].

$$\mu = \frac{\text{shear stress}}{\text{shear ratio}} \tag{2.16}$$

where *shear stress* is the frictional force (*N*) and depends on the area of contact between fluid layers, while *shear ratio* is the fraction of the velocity difference between two points (of the fluid layers), divided by the distance between those two points (*dx*). Viscosity can be also defined as *kinematic viscosity* ($\mu_k$) which is the dynamic viscosity divided by the density ($\rho$) of the liquid. Fluid is considered to be linear, Newtonian fluid. For these liquids, viscosity is constant when the pressure is applied. When the viscosity value varies under applied pressure, the fluid exhibits non-Newtonian properties [89]. Following Fig.2.8, if the value of *Re* > 2000 the fluid flow is *turbulent*. Then, the flow is an unsteady process, characterised by fluid mixing (e.g. whirlpool effect). If the value of *Re* < 2000, the flow is a laminar flow. This is a linear process characterised by smooth flow and parabolic velocity distribution. In our case, taking into the consideration the PCFs dimension, we calculated that the *Re* < 2000. For this reason, we can describe the flow as laminar.



Figure 2.9: *Fluid parameters in a capillary cross section*

In addition, as it is shown in Fig.2.9, when the flow is laminar it satisfies Poiseuille's law. The value of Reynolds number is proportional to a capillary radius. If radius is small, then we can observe capillary action [32, 43, 88, 90]. Here, the flow characterisation is accompanied by the flow parameters. Fig.2.9, presents the set of parameters. For instance, Poiseuille's law requires the value of the capillary radius, length of the capillary (*L*), and the fluid viscosity. In order to estimate the capillary action the surface tension of the fluid ($\sigma$), the contact angle between the fluid and the capillary wall ($\theta$), the fluid density ($\rho$), and also the capillary radius must be known. Knowing all parameters and dynamics of the system, the filling time of the capillary may be calculated

from the sum of all acting forces using Newton's second law [91]:

$$\sum \vec{F} = m\vec{a} \tag{2.17}$$

$$\sum \vec{F} = m\frac{d\vec{v}}{dt} \tag{2.18}$$

$$\sum \vec{F} = \vec{F_c} - \vec{F_f} + \vec{F_p} - \vec{F_g} \tag{2.19}$$

$$\frac{d}{dt}\left(\frac{m \cdot \vec{v}}{dt}\right) = \vec{F_c} - \vec{F_f} + \vec{F_p} - \vec{F_g} \tag{2.20}$$

where $m$ is mass, $a$ is acceleration, $v$ is velocity, $t$ is time, $\vec{F_c}$ is the capillary force, $\vec{F_f}$ is the friction force, $\vec{F_p}$ is an external pressure force, and $\vec{F_g}$ is the gravitational force.

We first analyse the capillary action, which gives us the capillary force. The capillary action describes the action of a liquid in a circular capillary with a radius ($r$), a liquid with a density ($\rho$) that is pulled into the tube without any external pressure or force, reaching a self-filled $L$ length of the capillary which is proportional to the surface tension ($\sigma$) of this liquid and the contact angle ($\theta$) between the liquid and the internal surface of the capillary. We have selected a sign convention such that when the $\theta$ is less than 90° for a low density liquid, the liquid creates a concave meniscus. When this angle is greater than 90° for a high density liquid, the liquid creates a convex meniscus. It depends on the surface tension of the liquid [87, 88, 92–95]. The force associated with the capillary action is then given by

$$L = \frac{2\sigma\cos\theta}{rg\rho} \text{ then } \vec{F_c} = 2\pi\sigma\cos\theta \tag{2.21}$$

which is fully described at Appendix B, and here $g$ is the gravitational constant $g = 9.81\ m/s^2$. The parameters described above (radius, density, gravitational constant and length) can be used to describe the volume of the capillary. From the left half of the capillary action Equation, the gravitational constant is left over. The product of the gravitational constant and mass equal a force (as explained in Appendix B). Then the left half of Equation ($\vec{F_c}$) equals the right half as shown in Equation 2.21.

Next we consider the frictional force, which may be used to describe Poiseuille's law (the flow rate $Q$) [43], as presented in Equation below. Friction opposes the filling of a capillary, due to the viscosity of the liquid. As presented in Appendix B the frictional force is given by:

$$Q = \frac{\pi r^4 P_p}{8\mu_d L} \text{ then } \vec{F_f} = 8\pi\mu_d L\vec{v} \tag{2.22}$$

where $P_p$ is external pressure. Initially, from Poiseuille's equation, a pressure is estimated, and the flow rate is replaced as the relation of a liquid velocity and the area

of the capillary. Then we can replace the pressure as a fraction of force to area, and reduce the area on both sides of the equation.

In addition, external pressure may be used to fill the capillary. The force ($\vec{F}_p$) associated to this can be expressed as the product of the external pressure ($P_p$) per unit area (as explained in Appendix B) [92]:

$$\vec{F}_p = \pi r^2 P_p \tag{2.23}$$

The last concern is the gravitational force ($\vec{F}_g$), which can be defined as:

$$\vec{F}_g = \pi g \rho r^2 L \tag{2.24}$$

For the gravitational force we adapted the results presented in the article of K.Nielsen et al. [87]. As was presented in this paper, three different silica capillary tubes with radii of 1 $\mu m$, 5 $\mu m$ and 10 $\mu m$ were tested in terms of the filling time. For these three capillaries, six filling times were estimated (using water parameters) for horizontal and vertical positions. The authors observed that for vertical and horizontal position of the capillary (10 $\mu m$ radius) the filling time was different. However, the various positions of two capillaries with smaller radius did not change the filling time. For this case, we can conclude that the vertical or horizontal position of a capillary of radius less than or equal to 5 $\mu m$ does not have an impact on the filling time. The flow direction is associated to the gravitational force. For capillaries ($r \leq 5 \mu m$) the gravitational force can be neglected. For this reason, considering small capillaries of PCFs fibres, we also neglected the gravitational force ($\vec{F}_g = 0$), and assumed that the fibre can be positioned vertically or horizontally without changes to the filling time [87].

The sum of these four forces, as in Equation 2.20, gives the final equation for $L$ as a function of $t$ filling time for this capillary (see Appendix B) [91, 96]:

$$L(t) = \sqrt{\frac{A}{B}t - (1 - e^{-Bt})\frac{A}{B^2}} \tag{2.25}$$

where:

$$A = \frac{4\sigma \cos \theta + 2P_p r}{r\rho} \tag{2.26}$$

$$B = \frac{8\mu}{r^2 \rho} \tag{2.27}$$

Unit calculations are attached to Appendix B.

Then, the $(1 - e^{-Bt})\frac{A}{B^2}$ part of Equation 2.25 tends to zero, due to much greater value of constant $B$ in comparison to constant $A$. Then, Equation 2.25 can be simplified to

following form:

$$L(t) = \sqrt{\frac{A}{B}t} \tag{2.28}$$

The filling time function has a square root profile. With Equation (2.28), the filling time $t$ $(s)$ of the cylindrical glass capillary as a function of the filled length $L$ $(cm)$ may be demonstrated. In order to estimate the filling time of PCFs, for example, the HC-PCF 1060 is considered as a bundle of glass capillaries with a circular shape. The core radius is approximated to $r_{core} = 4.85$ $\mu m$ and the cladding capillaries radius to $r_{hole} = 1.29$ $\mu m$. Using water and isopropyl alcohol (IPA) parameters (see Table 2.1) and HC-PCF 1060 core dimensions we may observe the differences in the filling time.

| Fluid | density $(\rho)$ $(kg/m^3)$ | surface tension $(\sigma)$ $(dyn/cm)$ | viscosity $(\mu)$ $(mPa{\cdot}s)$ |
|---|---|---|---|
| Water | 1000 | 72 | 1.01 |
| Methanol | 792 | 23 | 0.50 |
| IPA alcohol | 785 | 23 | 2.40 |
| NOA 73 | 1260 | 40 | 300.00 |
| Glycerol | 1261 | 63 | 934.00 |

Table 2.1: *Fluids parameters as in [97]*



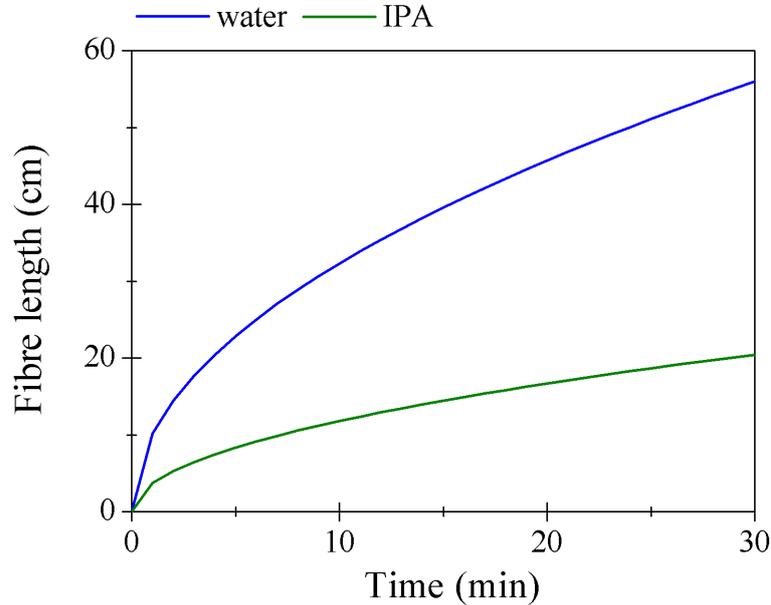Figure 2.10: *Graph of simulated time of filling the core of HC-PCF 1060 with water (blue line) and IPA (green line)*

Fig.2.10 presents the graph of two cases, where blue line indicates the filling of the fibre with water, and the green line the filling of the fibre with IPA. As we can see, for a lower viscosity liquid (as water) the $\frac{A}{B}$ equals $34.82^{-6}$ $\frac{m^2}{s}$. If IPA parameters are

considered, the $\frac{A}{B}$ equals $4.64^{-6}$ $\frac{m^2}{s}$. For the high viscous liquids, the constant $B$ is greater, and the value of the fraction decreases. The slope is lower. For this case the fibre core should be filled quicker with water than with IPA. Then, the coefficient $\frac{A}{B}$ of Equation 2.28 is associated to the slope of function and velocity of the fibre filling. Also, we can observe that until the first minutes the slope has a greater angle to the *x-axis*. Here, we may expect that the beginning of the filling is much quicker process, and at the same stage the process slows down.
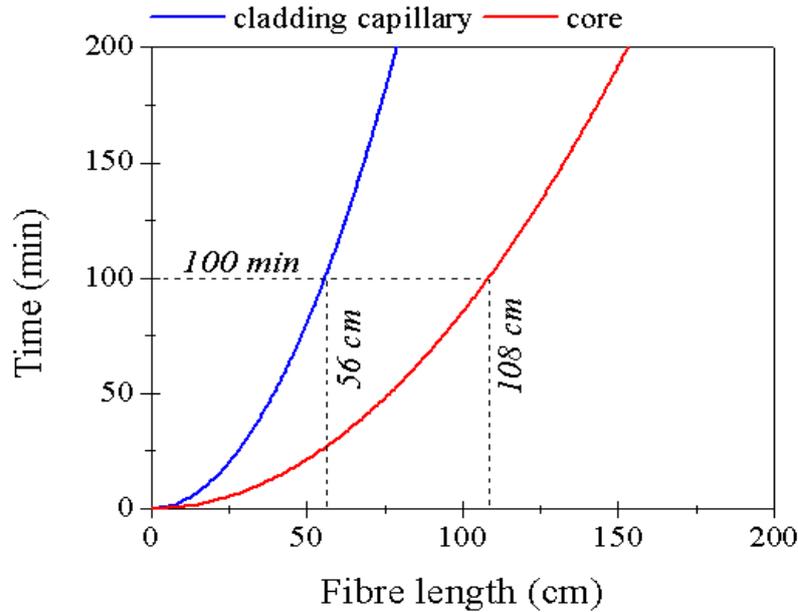


Figure 2.11: *Graph of simulated time of filling the core (blue line) and one of the cladding holes (red line) for HC-PCF 1060 with water*

However, we are interested to predict the filling time for a particular length of the fibre. Due to this fact we associate the filling time *(t)* with the fibre length *(L)* in Equation 2.28. This is plotted for the filling time on the *y-axis* against the fibre length on the *x-axis*. Here we simulate the filling of the fibre core (HC-PCF 1060) in comparison to the filling the cladding capillary with water (Fig.2.11). As you can see from Fig.2.11, the core of the fibre (red line) is filled first due to its larger diameter than the capillaries in the cladding (blue line). In 100 *min*, 108 *cm* of length of the core and 56 *cm* length of the channel in the cladding are filled with water. In addition, we analysed the filling of the fibre core with a range of fluids, the parameters of which are provided in Table 2.1. the contact angle is assumed to be $0°$ ($\cos\theta = 1$).

Fig.2.12 shows that by filling the core with fluids with a high value of viscosity such as glycerol (purple line) or NOA (orange line) it would require a longer filling time in comparison to fluids with low viscosity, such as methanol (green line) or isopropyl alcohol (IPA) (pink line). For a filling time of 15 *min*, 1 *cm* of the fibre is filled with

Figure 2.12: *Graph of simulated time of filling the core with different liquids: pink line is for methanol, green line is for IPA, orange line is for NOA 73, and purple line is for glycerol*

glycerol in comparison to 14 *cm* when filled with IPA. However, one more fluid parameter can change the filling time. The viscosity is very sensitive to temperature [98]. Thus any filling time measurement and recording of the position of the meniscus has to be followed with a controlling the temperature of the liquid.



Figure 2.13: *Graph of dynamic viscosity of water with temperature changes*

Fig.2.13 presents a variation of the viscosity of water with respect to changes in temperature ° Celsius is shown. When temperature increases, the sample viscosity decreases.

21

The viscosity of water undergoes a change of up to 12.9 % for a 5 ° Celsius change in temperature, and approximately 0.1 ° Celsius temperature change results in a 0.25 % change in viscosity. The filling time of the fibre (HC-PCF 1060) for an 11 *cm* length takes 65 *s* for water at 20° Celsius and 70 *s* for water at 23 ° Celsius. Then a change of 2° Celsius of water changed the viscosity by about 6.9%, which consequently also changes the filling time by around 7%.

## 2.4 Hydrogel

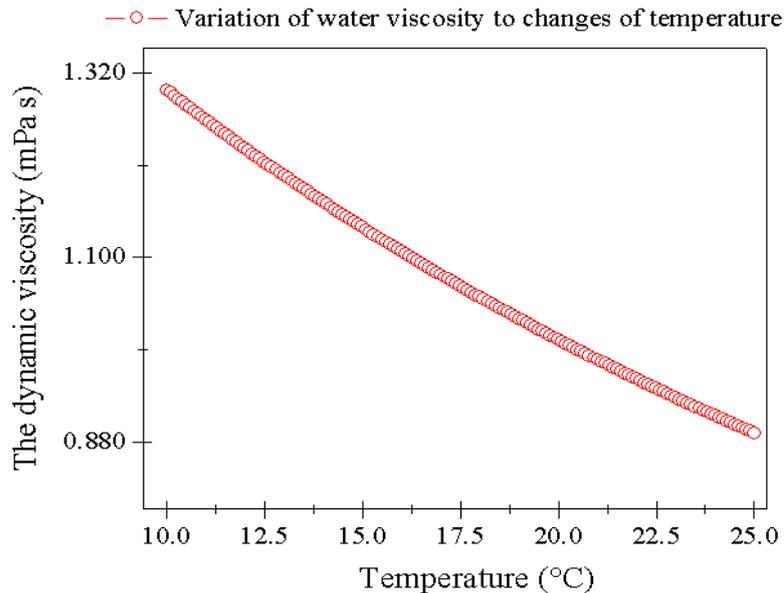In this thesis, we propose to integrate the HC-PCF with a biomaterial. In this section we define and present the biomaterial, called a hydrogel. The hydrogel is a three-dimensional, polymer widely used in medicine [51]. This is attractive for tissue engineering, as it is used as matrix for repairing and regenerating a variety of tissues and organs [51, 99–103]. One of the first research programs to design such polymer for human use, dates back to the 1950s [99]. The first target was in ophthalmology in the designing of soft contact lenses. In the 1980s hydrogel was employed in rhinoplasty and cell-encapsulation [51]. Other applications using hydrogel range from actuators and sensors for drug delivery to bioseparators [48, 99–102]. Hydrogel may be combined with enzymes, protein mimics, and antibodies to design controllable actuators [51, 99]. Hydrogel is widely used in pill capsules, oral ingestion (e.g. bioadhesive carriers), coatings for implants or inside capillary walls, membranes, sheets, e.g. reservoirs in a transdermal drug delivery patch [51, 102]. A wide range of polymer compositions have been used to fabricate hydrogel, using either natural polymers as: collagen and gelatin, hyaluronate, fibrin, amongst others [51, 102]; or synthetic polymers such as poly(acrylic acid) and its derivatives, poly(ethylene oxide), poly(vinyl alcohol), polyphosphazene, and polypeptides [51, 102].

| hydrogel type | A | B |
|---|---|---|
| stability | reversible character | permanent character |
| bonding mechanisms | molecular entanglements | cross-linked polymers |
| ancillary forces | secondary forces (inc. ionic) H-bonding and hydrophobic forces | conversion of hydrophobic to hydrophilic polymers |
| uniformity | non-homogeneous | non-homogeneous |

Table 2.2: *Characteristic of hydrogel groups A and B*

Hydrogel, as the name suggests, has a significant water content [104]. In general hydrogel can be classified according to its properties, and shared between two groups A and B as summarised in Table 2.2 [51, 105]. Hydrogel is known to be pH sensitive,

and also sensitive to ion concentration, temperature, solvent composition and electric potential. These parameters cause a change in phase, shape mechanics, recognition, permeation etc. [51]. Hydrogel is an elastic and flexible material [106]. One critical parameter of hydrogel is their biocompatibility, i.e.: *"a material ability to exist within the body without damaging adjacent cells or lead to significant scarring or otherwise to elicit a response that detracts from its desired function"* [104].
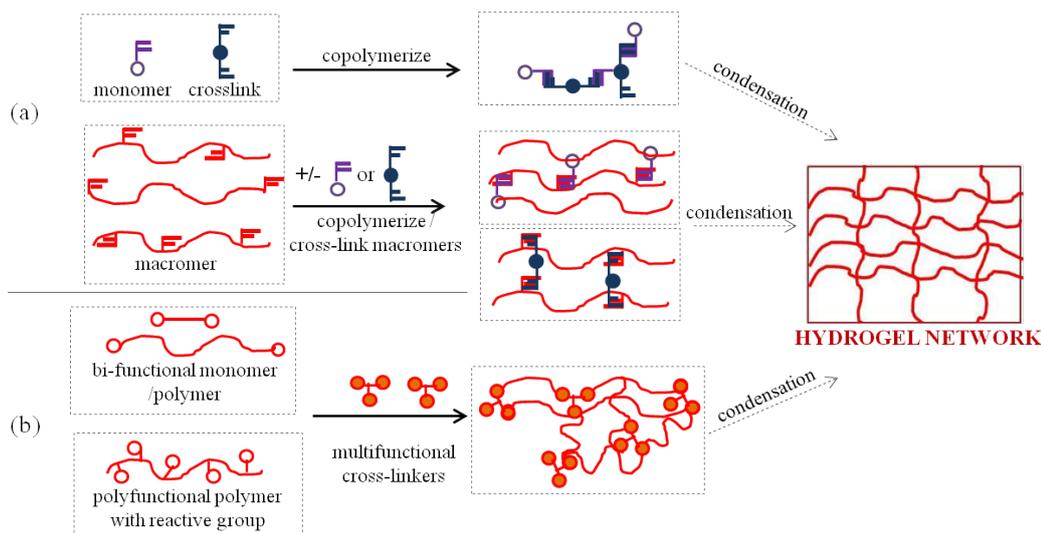


Figure 2.14: *The schematic illustration of two methods for forming cross-linked hydrogel by (a) free radical reactions or (b) condensation reaction of multifunctional cross-links*

Fig.2.14 shows a simplified scheme to form the hydrogel matrix of type B. Hydrogel is an insoluble cross-linked polymer network with structures composed of hydrophilic, homo- or hetero-co-polymers. Cross-links, called tie-points or junctions, can form a covalent bond, permanent physical entanglements or microcrystalline regions [106]. For example, the monomers can be attached to each other with a cross-link, as is shown in Fig.2.14a. Using the free radicals, hydrogel may be formed using macromers, with double bonds, which can be connected either with a cross-link or a different monomer. Fig.2.14b illustrates a connection of a macromer with multi-functional cross-links. It can be summarised that, for all of the described examples, chains are condensed to form a polymer network [99, 104, 107]. Depending on the rigidity of the original polymer chains, types of cross-link molecules, and the cross-link density [51], the properties below can be observed:

*a) Hydrogel swelling*

Hydrogel is a highly hydrophilic material, i.e. it has the ability to absorb water into its structure. First, the water enters the network matrix and hydrates the hydrophilic groups, which is called *primary bound water*. The hydrogel is hardly ever dehydrated,

due to the presence of *primary bound water*. Then the network swells. This is the so called *secondary bound water*. The network absorb additional water, due to the osmotic driving force of the network chains. This is so called *free* or *bulk* water. The water fills an empty volume between the polymers chains (i.e. pores, voids) [51]. As an application the swelling character might be tailored to allow the control of drug release [99, 100, 108, 109].

*b) Presence of pores*

The permeability of the hydrogel depends on the size of pores, defects, or voids in the network which are formed during the polymerisation process. From an experimental point of view, the estimation of the pore size is important in order to control the transportation of proteins, oxygen, or the release of drugs, or antigens through its matrix. The pore size is strongly determined by the composition of the cross-links [51, 110, 111].
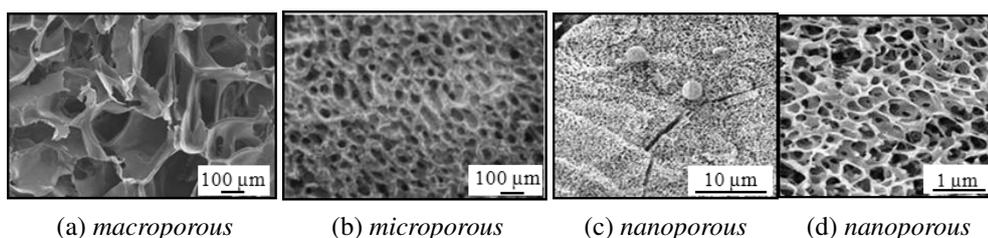


| (a) *macroporous* | (b) *microporous* | (c) *nanoporous* | (d) *nanoporous* |

Figure 2.15: *The SEM images of porous hydrogel, where (a) is macroporous hydrogel [112], (b) is microporous hydrogel [113], (c) and (d) are nanoporous hydrogel shown in [114]*

In terms of porosity, hydrogel can be classified as macroporous ($d_{pore} > 10 \ \mu m$), microporous ($1 \ \mu m < d_{pore} < 10 \ \mu m$), and nanoporous ($d_{pore} < 1 \ \mu m$) [112, 115]. For example, the illustrations of Fig.2.15 present (a) macroporous hydrogel based on 2-hydroxyethyl methacrylate [112], (b) microporous hydrogel based on poly(vinyl methyl ether) [113], and (c) and (d) are nanoporous hydrogel based on hydrocarbon-PEO-fluorocarbon [114].

In this work we focus on the hydrogel based on poly(ethylene) glycol diacrylate (PEGDA) due to its immobilisation and hybridisation character for DNA probes [49, 109, 115–120]. The growth of the PEGDA hydrogel requires the presence of photo-sensitive molecules, such as Eosin Y, to polymerise the PEG solution into the hydrogel [104, 119, 121–125]. In this work the PEGDA hydrogel was grown on a silica surface (either on the side of a microscope slide or on the internal walls of a glass optical fibre capillary). The polymerised PEGDA was then covalently attached to the surface. The entire hydrogel growth process follows the steps: surface preparation (silanisation), surface chemical treatment (PEGDA) and photo-initiation (polymerisation and cova-

lent attachment). The background for the steps of growing the PEGDA hydrogel are described in the next subsections.

Here, the author would like to acknowledge Dr.Francine Kivlehan and Dr.Paul Galvin, who developed the PEGDA hydrogel growth process on glass.

### 2.4.1 Silanisation process

Silanisation is defined as a method of bonding chemical components to a surface. It forms a *silane* group on the glass, i.e. attaching the organic molecules to the glass surface [104, 122]. It is necessary to prepare the surface in order to covalently attach a PEGDA hydrogel. The silanisation process follows a strict protocol, which can be divided into two parts: (a) bonding a silanising agent to the glass surface, and (b) bonding the photo-sensitive molecule Eosin Y to the silanising agent.

*(a) APTMS - the silanising agent*

The silanising agent aminopropyltrimethoxysilane, which is known as APTMS, is frequently used [126]. This agent is able to trap organic and non-organic molecules near the glass surface. Specifically, the APTMS bonds with its silane group to the glass surface, and its amino-group bonds to other molecules.



Figure 2.16: *The attaching process of the silanising agent APTMS to a glass surface (part 1)*

Fig.2.16 shows an illustration of the silanisation procedure, where APTMS is diluted with methanol *(MeOH)* and distilled water *(H$_2$O)*, shown as *MeOH* : *H$_2$0*. Then the product of the solution bonds silane groups of molecules together and forms a monolayer at the glass surface due to the condensation process.

The next step of the bonding of APTMS is presented in Fig.2.17. It shows the drying process of the glass. The hydrogen is disconnected from APTMS, which then bonds covalently to the glass surface with its oxygen molecule. Finally, the glass surface is covered with silane groups, i.e. with APTMS reagent covalently attached to the glass surface.

Figure 2.17: *Scheme of an attaching silanising agent APTMS to a glass surface (part 2)*

*(b) Eosin Y molecule and protocol*

The second part of the surface treatment includes bonding Eosin Y to the APTMS reagent, already attached to the glass surface. Fig.2.18 represents the chemical structure of Eosin Y. The Eosin Y is a disodium salt of 2′, 4′, 5′, 7′ tetrabromofluorescein ($C_{20}H_8Br_4O_5$).



Figure 2.18: *Graph of the absorption and emission profile as a function of wavelength, and inset shows the Eosin Y chemical structure*

The absorbance profile and emission of Eosin Y is plotted in Fig.2.18 where on the *y-axis* is the normalised value for absorbance and fluorescence, and on the *x-axis* is wavelength *($\lambda$)*. The main absorption peak is centred at $\lambda = 525$ *nm*, and the fluorescence peak is shifted to $\lambda = 545$ *nm*. Eosin Y is characterised by its high phosphorescence efficiency. Herein, it can be assumed that the excitation of Eosin Y is followed with photon emission [85, 127]. In order to attach Eosin Y into the glass surface covered with APTMS, another chemical procedure was followed and is schematically shown in Fig.2.19. Eosin Y and EDAC (1-ethyl-3-(3-dimethylaminopropyl) carbodiimide hydrochloride $C_8H_{17}N_3 \cdot HCl$ react with sodium hydroxide (NaOH) and sodium dihydrogen phosphate ($NaH_2PO_4$).

The solutions NaOH and $NaH_2PO_4$ reduce the pH and allow Eosin Y to be diluted in

Figure 2.19: *Scheme of EDAC and Eosin Y reaction within a lower pH solution, to form a O-acylisourea intermediate*

a shorter time than with water of neutral pH. In this case EDAC was used due to its ability to activate carboxyl or phosphate groups in order to form amine bonds, which are marked within Fig.2.19.



Figure 2.20: *Scheme of bonding O-acylisourea intermediate and amine group of APTMS*

The product *O-acylisourea intermediate*, which is unstable, is illustrated on the right side of Fig.2.19. There is an amine-bond, with which prepared Eosin Y is attached to APTMS. The reaction between O-acylisourea and APTMS is illustrated in Fig.2.20.



Figure 2.21: *Scheme of the silanised glass surface and the rest of EDAC*

On the left side, the O-acylisourea intermediate bonds its amine group with APTMS amine group. Products of this reaction are the attached Eosin Y with APTMS and the residual EDAC molecule, as shown in Fig.2.21. The silanisation process is thus completed.

## 2.4.2 Chemical treatment

The chemical treatment of the hydrogel growth process involves treating the glass with a solution of three chemical composites diluted in a phosphate saline buffer (PBS). The PEG/VP/TEOA (PVT) is a precursor solution made up of three chemicals. The basic chemical structure of each of the three compounds used is shown in Fig.2.22.



(a) $H(OCH_2CH_2)_n$      (b) $C_6H_9NO$      (c) $(HOCH_2CH_2)_3N$

Figure 2.22: *The chemical structure of (a) poly(ethylene) glycol (PEG), (b)1-Vinyl-2-pyrrolidinone (VP) and (c) Triethanolamine (TEOA)*

Poly(ethylene) glycol (PEG): $M_w$ 700, as shown in Fig.2.22a, is a macromer. PEG is non-toxic, hydrophilic, and has a high ability to be cross-linked [122]. Fig.2.22b shows the second compound 1-Vinyl-2-pyrrolidinone (VP), which is the second polymer. It is polymerised into hydrogel with the PEG polymer. The VP is also a catalyser for the polymerisation process and it is commonly named a polymerisation accelerator [50, 128]. The last chemical ingredient of the solution is triethanolamine (TEOA) shown in Fig.2.22c. It is not a monomer, but it acts as a co-initiator. It is known as an electron donor, creating a free radical. The free radical is understood as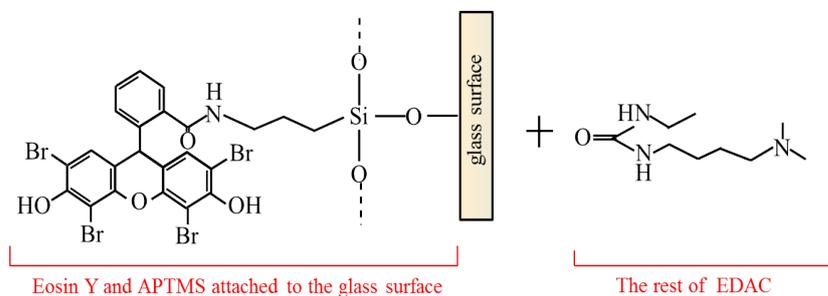 a molecule which has one unpaired electron [129]. Both Eosin Y and TEOA are free radical chains, which are carrying a polymerisation process [125].

Depending on the concentration of the three components (Fig.2.22), the properties of the hydrogel may change. It has been demonstrated that it is possible to control the PEGDA hydrogel thickness, permeability and arrange a cross-link density [117, 123, 124, 128]. Adjusting the ratio between PEG and VP concentrations, it is possible to control the thickness of the hydrogel matrix. When the concentration of PEG increases, the hydrogel volume increases [123]. Another important parameter of the hydrogel, is the cross-link density. The cross-link density may be understood, as the number of cross-links *QBP* per polymer chain number (see: Fig.2.27). In [123] it was shown that the higher the value of the cross-link density, the less permeable the membrane is. Likewise, for PEG, as concentrations increase higher cross-link density is obtained, which means lower permeability. If however the concentration of TEOA is increased, the opposite impact occurs for the cross-link density. Furthermore, the hydrogel cross-link density depends on the thickness of the layer. This means that in the different layers of hydrogel there can be different values for cross-link density

[123]. The concentrations of the PVT solution used in this thesis and morphology of the grown hydrogel are described in Chapter 5.

### 2.4.3 Polymerisation



Figure 2.23: *Idealised representation of PEGDA network [111]*

The polymerisation is based on the cross-linked structure of poly(ethylene glycol) (PEG), which is polymerised using free radicals, resulting in a covalently bonded network. An idealised representation of PEGDA hydrogel is illustrated in Fig.2.23, which shows examples of cross-links at the left and right ends of network, bonding to PEG at the centre of structure [111].



Figure 2.24: *Complete process of the PEGDA hydrogel polymerisation*

In this work free radicals of Eosin Y and triethanolamine (TEOA) were used to cross-link polymers to the PEGDA hydrogel [122]. This photo-polymerisation process is nonlinear and polymers chains are formed through propagation of free radicals. This

photo-polymerisation process can be understood by analysing in Fig.2.24. The simplified schematic has four stages.

In the first stage of polymerisation, (I quadrant Fig.2.24) Eosin Y in the presence of the PVT solution is excited using the wavelength 525 $nm$. Eosin Y absorbs light and its electron changes its state from a ground state to a triplet. It is indicated by ($EosinY^*$). This is a phosphorescence process, which is explained in the next Section 2.5. The excited Eosin Y collects an electron from the donor TEOA.



Figure 2.25: *Scheme of proton loss from TEOA$^\bullet$+ to neutral radical TEOA$^\bullet$, that allows polymerisation*

In order to explain the II quadrant of Fig.2.24, Fig.2.25 is given. Here the reduced triethanolamine cation radical TEOA$^{\bullet+}$ is accompanied by a loss of a proton ($H^+$). The $\alpha$-amino radical (TEOA$^\bullet$) is the free radical ($\alpha-amino$) that may allow polymerisation [119, 122].



Figure 2.26: *Scheme in which the proton is transferred from Eosin Y$^{\bullet-}$ and gives a free radical to Eosin Y$^\bullet$*

Moving to the third part of Fig.2.24 (III quadrant), here the third stage of the polymerisation begins. In Fig.2.26 the lost proton ($H^+$) of TEOA initiates the molecule Eosin Y$^{\bullet-}$ to become the free radical Eosin Y$^\bullet$ ($\alpha-amino$). It is believed, that these radicals polymerise PEG/VP into a gel state. The $\alpha$-amino radical (TEOA$^\bullet$) is generated in dense liquid, when Eosin Y$^\bullet$ is mostly bonded to the surface. The $\alpha$-amino radicals

of Eosin Y$^{\bullet}$ form a stable bond to allow growth of the polymer onto the glass surface, when TEOA$^{\bullet}$ radicals diffuse from the surface and initiate polymerisation within the PEG precursor. It has been verified that the polymerisation process may be initiated only with $\alpha$-amino radicals of Eosin Y$^{\bullet}$. However, this process is very slow [122].



Figure 2.27: *Scheme of the polymerisation process of PEG/VP chains and free radicals, to the PEGDA hydrogel*

The last quadrant (IV) of Fig.2.24 presents the last stage of polymerisation, of which details are illustrated in Fig.2.27. Here it specifies details of the polymers' formation with reaction steps between PEG and VP chains and free radicals. This process is a bonding of monomers/macromers with free-radical chains creating a polymer structure. A free radical chain (Eosin Y$^{\bullet}$ or TEOA$^{\bullet}$) is joined together with a PEG chain. PEG is a macromer and has a pendant double bonds (*PDB*) at both sides of the chain *PDB*, illustrated in Fig.2.27 as a short red line. One end of the free radical is attached to *PDB*. However, it is still a free radical, and for this reason it is called a *live radical with PDB*. It needs to bond to another free radical in order to neutralise this molecule. Then another free radical bonds the molecule that creates a *branch dead polymer*. Following Fig.2.27, an identical process happens at the another end of the *branch dead polymer*, the free radical chain bonds to free *PDB*, and then, is named *branch live polymer*. The live branch polymer may be bound to another *branch live polymer* and finally the polymer is created. A *cross-link* is a *quaternary branch point (QBP)* such that four chains are interconnected. The PEGDA hydrogel polymerisation is thus completed [124, 125].

## 2.5   DNA microarray and luminenscence

DNA is a nucleic acid. It has a double-helix polymer structure, in which the two strands are linked by a pair of bases (nucleotides). One pair is adenine - *A* and guanine - *G*, and the other pair is thymine - *T*, and cytosine - *C*. Usually DNA is double stranded, where nucleotide pairs are complementary to each another, for example: A-T and G-C. The order of nucleotides identifies the genetic code, and it carries instructions for the synthesis of RNA molecules and proteins. A unique sequence of DNA is found in all organisms, and in many viruses [130]. For our purposes, DNA is assumed as a large molecule attached within the hydrogel structure. The DNA probe used for experiments in this project, was originally prepared (i.e. sequence, length, and attaching fluorochrome molecule to DNA probe) in Metabion International AG Germany. The amino-modified oligonucleotides have a sequence of 21 pieces with the following order:

(1) (Cy-5)-TACAGGCTTACCGTCATAGGT-C7-Aminolink

(2) (Cy-5)-GCCTAAGCCCTCTTTCTCAGT-C7-Aminolink



Figure 2.28: *The scheme of DNA probe connection with a NHS-cross-link and the PEG polymer*

Fig.2.28 demonstrates a chemical scheme of bonding the labelled DNA probe to PEGDA polymer. At the right-side, Fig.2.28 presents the DNA molecule with the attached fluorochrome molecule: cyanine dye orange-red (Cy-5) (indicated by red star). In addition, DNA had the attached aminolink ($H_2N$ in Fig.2.28) to a seven carbon spacer. The aminolink supported bonding between DNA and PEGDA polymer. However, it was required to use linker stabilisator which was called a *cross-linker*, and it is shown in the middle section of Fig.2.28. For our purpose, we used NHS-PEG-acrylate powder. At the left-hand side of Fig.2.28 is shown a chemical structure of PEGDA polymer.

### 2.5.1   Luminescence detection

Luminescence is a process of interaction of light within molecules. One of the key applications of luminescence is the ability to determine biomolecules. For instance, this process allows the verification of DNA existence, determines the location,

and observes reactions within.

In order to describe the luminescence mechanism, we here concerned that the total energy in the molecule is the sum of the three energies: electronic, vibrational and rotational. The electron becomes excited due to an external process; these processes are recognised as: physical (e.g. absorption of light), mechanical (e.g. friction), or chemical (e.g. reactions). The electron transits from a ground state $(S_0)$, the lowest electronic level to the excited absorption state $(S_1)$. The spontaneous emission process returns the electron from the excited state to the ground state. Here, photons can be emitted [85, 131]. This is luminescence and can be named fluorescence or phosphorescence. In order to explain a difference between the fluorescence and phosphorescence it is useful to refer to Jabłoński's diagram [85, 131], which is illustrated in Fig.2.29.



Figure 2.29: *Jabłoński's diagram for fluorescence excitation, with VR-vibrational relaxation, IC-internal conversion, and ISC-internal system crossing*

The electron transit can be described as follows: (a) radiative when the photon is emitted (straight arrows in Fig.2.29) and (b) non-radiative (wavy arrows in Fig.2.29). A photon is absorbed by an electron (red dot). It changes its energy state to the second excited state $S_2$. At each of the excited levels are energy vibrational levels (solid lines). The electron falls through these levels, as in *stair-steps*. This movement is called *electronic-vibrational state coupling* or *vibrational relaxation (VR)* and takes picoseconds. No photon is emitted, but a quantum of mechanical vibration (energy) called a *phonon*. Next, the electron transits from the $S_2$ singlet state to the first excited singlet state $S_1$, where this path is called *internal conversion (IC)* (violet-wavy arrow). There are only a few molecules known to have radiative emission from the $S_2$ state.

Again, the electron vibrates through the vibration levels of state $S_1$, with non-radiative transmission. Finally, the electron returns to the ground state $S_0$ and a photon is emitted. The wavelength of the emitted photon is usually longer in comparison to the initial excitation photon, due to loss of energy through non-radiative transitions. The difference between the excitation and emitted wavelength in longer wavelength directions is called *Stokes shift*. This is fluorescence, with a short lifetime *((t))* and it is typically a nanosecond.

The lifetime *(t)* is defined as the mean time that the electrons occupy a given excited state [131] and inversely proportional to the electron decay rate *(Γ)*. The rate of decrease of electrons in the excited state is proportional to the number of electrons in the upper state *(N$_2$)*, and the decay can be expressed as:

$$\frac{dN_2}{dt} = -N_2\Gamma \tag{2.29}$$

where the number of electrons in the upper state then decays exponentially with the lifetime, as below:

$$N_2 = N_2^{(t=0)}e^{-\Gamma t} \tag{2.30}$$

In a conventional fluorescence process, only two excited states are involved, and all electrons transitions occur without a change of spin [85, 131]. However, for some molecules, the electron does not return to the ground state, but changes its spin and transits to another energy state $T_1$. This is *internal system crossing (ISC)* (blue-wavy arrow). The $T_1$ triplet state has lower energy compared to the first excited state $S_1$. This state is characterised by a different spin than the $S_1$ singlet state. Here, also the vibrational states exist. Thus, the electron vibrates through the triplet state with a non-radiative process and falls into the ground state with a photon emission. However, this causes a spin-violation to occur due to the spin-orbit coupling. Therefore, the phosphorescence is characterised by a much longer lifetime, in the range of seconds [85, 127, 131]. One phosphorescence example is the Eosin Y emission process.

In this project, the fluorescence time domain measurements were performed using a Photo-Multiplier-Tube (PMT) (Hamatsu H9656-20), and two different fluorochrome: Cy-5 dye and Alexa-750.

Fig.2.30 shows the excitation and emission profile of Cy-5 fluorochrome. The maximum excitation wavelength is $\lambda \approx 649$ *nm*, and the maximum emission wavelength is $\lambda \approx 670$ *nm*. The Stokes shift equals 21 *nm*. The lifetime of Cy-5 equals about 1 *ns*. Here, we also determined one more parameter associated to the fluorescence, the molar extinction coefficient $(\phi)$ for Cy-5 dyes equals $\approx 250000$ $M^{-1}cm^{-1}$ [132].

Fig.2.31 presents the excitation and emission profile of Alexa-750 fluorochrome. The

Figure 2.30: *The excitation and emission profiles for Cy-5 fluorochrome*



Figure 2.31: *The excitation and emission profiles for Alexa-750 fluorochrome*

maximum excitation wavelength is $\lambda \approx 749$ *nm*, and the maximum emission wavelength is $\lambda \approx 775$ *nm*. The Stokes shift is 26 *nm*. The lifetime of Alexa-750 equals around 0.7 *ns*, and the molar extinction coefficient $\phi \approx 240000$ $M^{-1}cm^{-1}$ [132].

## 2.6 Summary

Summarising this chapter, the structure of the HC-PCF and light guidance model was demonstrated. The guidance is related to the arranged air-channel, which creates the microstructure cladding along the fibre length. The core of the HC-PCF is assumed to be an additional defect within the fibre structure, which allows light guidance within bandgaps due to the ARROW mechanism. The changes in light guidance for the filled fibre with absorbing material were discussed and limited to the influence of the refractive index and attenuation coefficient. The changes in the refractive index within the fibre resulted in a bandgap shift or changes to an index-guiding mechanism.

The physics of filling the fibre was explained. The fibre filling process can be applicable for a broad choice of liquid samples. It was presented that the core as a larger capillary is filled first in comparison to capillaries in the cladding. High viscous liquids fill the fibre for a longer time in comparison a low viscous liquids.

The PEGDA hydrogel was presented and proposed to be a suitable material within which the DNA probe can be attached. The process of preparing the glass surface for bonding hydrogel was discussed, including the hydrogel growing conditions (the photo-polymerisation). In order to verify the DNA presence within the hydrogel, a proposal was made to use the fluorescence technique. This process was explained in the final part of this chapter.

# Light guidance within HC-PCFs

## 3.1 Introduction

In this chapter we report the detailed analysis carried out in this thesis in order to use HC-PCFs in sensing. To do this, we present the numerical and experimental analysis of light guidance in HC-PCFs. This discussion is supported by the observation of optical modes. We also analyse and test the changes of refractive index within the air-channels of the HC-PCFs.

The numerical analysis of light propagation within HC-PCF 1060 begins by creating an image of the fibre structure used for the numerical model. Wave equations are then applied to the fibre image. In order to find the solution of the wave equations, numerical methods have to be applied. There are a number of well known methods to calculate light propagation [56]. One example is the plane-wave method (PWM). This is one of the first methods developed to illustrate the guidance parameters for PCFs. Here, the microstructure cladding of the fibre is assumed to be a two-dimensional photonic crystal. Following this interpretation, calculations are based on the reciprocal space of this crystal and operate within a fibre supercell. There are other methods: biorthonormal basis method (BBM), multipole (MPM), Fourier decomposition method (FDM), a finite difference method (FDTD), and a beam propagation method (BPM) [56, 58, 80, 133–135]. Details of all these methods may be found in [56]. In this project, the finite element method (FEM) was used to solve the Helmoholtz equation for HC-PCFs. However, calculations using this method are well known and can be reproduced accurately by a commercial available numerical package called Comsol Multiphysics v3.5a. At first, it is necessary to implement the fibre structure image in the software. Next, the applied object was divided into a subset of small elements called *elementary subspaces*. These small elements are concentrated at points where the structure has changed either in shape or refractive index forming a *mesh*. For each mesh element one solution of the wave equation is calculated. The combination of these solutions is calculated to give information about the effective indices in a frequency domain. The solver also presents distributions of the electric field (or magnetic field) over the fibre image. More details about calculations of this method and the

Comsol solver can be found in the literature [56, 136].

The experimental investigations of the light propagations within HC-PCF 1060 starts with a presentation of the broad light source, which is the supercontinuum and follow with the transmitted spectra and optical modes anlysis. In the last section of this chapter, we present the spectrum of the supercontinuum signal transmitted through a fibre which is fully filled with water.

## 3.2 Simulation of light propagation in HC-PCFs

The aim of this section is an investigation of optical modes of HC-PCFs and any guidance changes, when the fibres capillaries are filled with a material with a refractive index greater than air, but lower than fibre glass (silica).



Figure 3.1: *Cross-section of HC-PCF 1060, courtesy of NKT Photonics A/S*

Fig.3.1 shows the cross section of the HC-PCF 1060. The fibre was designed to propagate wavelength at $\lambda = 1060$ $nm$ in its air-core, and was manufactured by NKT Photonics A/S. The core diameter was $D_{core} \approx 9.8$ $\mu m$, and the pitch $\Lambda = 2.75$ $\mu m$ (i.e. a spacing between cladding holes, which is described in Chapter 2). The holey region had a diameter $d_{holey} \approx 50$ $\mu m$. Total fibre diameter was $d_{fibre} \approx 123$ $\mu m$. The fibre contained around $aff = 94\%$. In addition, two different fibres were investigated. Full description of these fibres can be found in Appendix A. Here, we only focus on the results with HC-PCF 1060.

In order to simulate light properties within PCFs, it is required to reproduce the fibre structure. As we can see, this structure is complex. Also, a discrepancy in the implemented dimensions compared to the real ones may cause incorrect light characteristic [69, 137–139]. For this reason, the fibre structure for the simulations should be designed as realistically as possible. For some of the numerical models it is possible to

import a bitmap image of the fibre cross-section [140]. However, for most of the numerical models, the fibre structure has to be drawn. In this project, the fibre structure was created employing AutoCad software. Afterwards the fibre drawing was exported to the Comsol programme.

**AutoCad drawing**

AutoCad is an advanced drawing software that allows detailed reproduction of complex structures including in this project the fibre structure containing deform actions which occurred during the fabrication process. The shapes of the cladding hole and the core were adapted from reference [77]. However, the fibre dimensions were implemented in the drawing using real parameters of the HC-PCF 1060 given by the manufacturer data sheet.



(a) *Single units*  (b) *Full structure*

Figure 3.2: *Scheme of the fibre drawing for a simulations, where in (a) are shown individual units: (1) is a base unit, (2) is one of two units of the first hole's ring, (3) is the other unit of the first ring, and (4) is the core, (b) complete created fibre structure*

The microstructure cladding of HC-PCF 1060 resembles a triangular lattice of air holes. Each air hole looks like a hexagonal shape with curved corners. This hexagon is then a base unit of the lattice. Using Equation 2.6 for the *aff*, we can reproduce the proportions of the fibre structure elements. Then, the air filling fraction ($aff_{HC-PCF}$) specifically for HC-PCF 1060 equals:

$$aff_{HC-PCF} = (\frac{d}{\Lambda})^2[1-(1-\frac{\pi}{2\sqrt{3}})(\frac{d_c}{d})^2] \tag{3.1}$$

where $d_h$ is the width of the cladding hole (hexagon), $\Lambda$ is the pitch, and $d_c$ describes the curvature of the corners of the hexagon [58, 77, 141]. According to the NKT manufacture data sheet, the pitch and air filling fractions were assumed to be $\Lambda = 2.75\ \mu m$ and $aff = 94\%$, respectively. Taking into account both values, we can find all

necessary dimensions of elements. For example, the hexagon width is the ratio of $d_h/\Lambda$ [77]. It equals 0.98, which gives $d_h = 2.7 \ \mu m$. The curvature of the hexagon corners equals $d_c \ / \ \Lambda = 0.44$, which is 1.21 $\mu m$. Fig.3.2a presents the drawn hexagon. It is marked as (no.1). These hexagons create a triangular lattice, as shown in Fig.3.2b (red dashed triangle). This lattice structure is the fibre microstructure cladding. In order to model the fibre core, seven hexagons from the centre of the lattice were removed. In a separate area of the drawing, seven hexagons were connected to each other. The internal lines were erased. Fig.3.2a shows the shape formed (i.e. the core) as (no.4). An outer edge of the created shape was curved in two places. An internal curvature equals the ratio of $D_{cv} = 0.59 \times D_{core}$ [77], where $D_{core}$ is the diameter of the core (9.8 $\mu m$). Therefore the rounding equals $D_{cv} = 5.74 \ \mu m$. The outer curvature is derived from the ratio of $D'_{cv} = 0.202 \times D_{core}$ [77] and equals $D'_{cv} = 1.44 \ \mu m$. However, to fit the core in the empty space in the centre of the lattice, it was necessary to reduce the size of the first hexagons to the empty space at the centre. Fig.3.2b shows the sequence of twelve cut units alternately placed around the core. Six of them are larger, and have width $l = 1.93 \ \mu m$. The cut line had to be curved as well. The curved cut edge then has the rounding of ratio $d'_c/\Lambda = 0.1$, being 0.28 $\mu m$. This element is illustrated in Fig.3.2a as (no.2). The (no.3) unit in Fig.3.2a is the smallest unit. The hexagon was cut to a width of $l = 1.55 \ \mu m$. The cut edge has the same rounding as that for the (no.2) unit. Unit cells (i.e. no.2 and no.3) around the core were placed at a 0.5 $\mu m$ distance to keep the Fabry-Perot resonator for the wavelength 1060 $nm$ for the first magnitude order (explained in Chapter 2). Also this number was recommended in the literature [137, 142]. The model structure was cut to a square of dimension 19.25 $\mu m$ with the core in the centre. It was referenced in the literature [77] that this square is a supercell of HC-PCFs. For this reason, we assumed that this structure is an accurate representation of a real HC-PCF 1060, and can be used for further calculations in terms of localisation propagation regions.

**Comsol package**

The created image of the fibre as shown in Fig.3.2b was imported to the Comsol module. Using subdomain settings of the numerical model, the internal area of holes had refractive index 1.00, just like air. The area between the holes and black lines for silica glass had refractive index 1.45. The fibre structure was assumed to be uniform along the $z$-axis. Only the $x,y$-planes of the image were considered for the calculations. The Comsol programme simulates light characteristics using the FEM. For this reason, the fibre model structure was split into a mesh.

Figure 3.3: *Applied mesh of the fibre structure*

Fig.3.3 presents a fitted, normal mesh to the applied fibre structure. It contains 61860 subspaces as triangles and quadrilaterals. Each subspace had homogeneous refractive index material. Edges of the image (of the cladding) indicated boundaries for further calculations. The solver assumed that the electric and magnetic fields have a zero value at the edge of the model structure. The initial and boundary conditions were applied by the Comsol using its default settings. This software derived an eigenvalue equation for the electric field $(\vec{E})$ from the Helmholtz equation for each element of the mesh. The Helmholtz equation is derived from Maxwell's equations. This is the electro-magnetic (EM) wave equation for cylindrical coordinates assuming that the fibre is linear, isotropic and non-magnetic material [56, 71]. It describes the EM field distribution along the fibre and guiding modes. It is given by [71]:

$$\vec{\nabla}^2 \vec{E} + n^2(\omega) \frac{\omega^2}{c^2} \vec{E} = 0 \tag{3.2}$$

where $n$ is refractive index in the angular frequency domain, $\omega$ is angular frequency, and $c$ is speed of light in vacuum. The effective index for a particular wavelength, is:

$$n_{eff} = \frac{\beta}{k_0} \tag{3.3}$$

where $\beta$ is an out-of plane wave vector (in the $z$-direction) and $k_0$ is a free space wave number. This equation was also shown in Chapter 2.

The Comsol programme solves the Helmholtz Equation for a given wavelength, finding the largest effective mode index. According to the presented theory in Chapter 2 the effective index number of modes in the fibre core is lower, than the refractive index of the fibre core material. For example, in the case of air filled fibre core, the effective index should have a value close to 0.99. When the fibre core has changed its

refractive index to 1.33, the effective index should have a value close to the number 1.329. In addition, a range of calculated effective indices can be expanded. It allows to find higher order modes, which have lower effective indices than the fundamental-like mode. We collected ten different effective indices close to the numbers: 0.97, 0.98 and 0.99 for the (air) core fibre. Then, thirty effective indices for one wavelength were generated. The selection of the analysed wavelength range ($\lambda = 350\ nm$ to $\lambda = 1700\ nm$ using 10 $nm$ step) was dictated by operating the supercontinuum source and an optical spectro-analyser within this range, which are presented in the next section of this chapter. In order to plot light propagation within the fibre all determined effective indices and wavelengths were taken into account. It created 126 wavelengths multiplied by 30 effective indices giving a total of 3780 points. On the *x-axis* were wavelengths and on the *y-axis* were effective indices [77, 133, 143]. These graphs are presented in Fig.3.5, Fig.3.6 and Fig.3.7. However, before we analysed these graphs we briefly present an example for identifying the optical mode for a standard optical fibre adapted from [144, 145]. For the cylindrical waveguide such as an optical fibre, optical modes are described as *TE* (where $\vec{E}_z = 0$ the electric field in the *z*-direction) and *TM* (where $\vec{H}_z = 0$ the magnetic field in the *z*-direction) with the addition of hybrid modes such as *HE* and *EH*. The specific combination when the modes are linearly polarised can be represented as $LP_{lm}$ (L-linearly, P-polarised). There are two integers describing the mode: *l* radial eigenvalue, and *m* angular eigenvalue.



Figure 3.4: *Generated field patterns with the aid of the numerical modelling (Comsol): (a) is the fundamental-like mode $LP_{01}$-like, and higher order modes: (b-e) is $LP_{11}$-like for a different geometric orientation of the electric field as: (b) right-elliptical, (c) left-elliptical, (d) vertical, (e) horizontal, (f-g) $LP_{21}$-like, (h) $LP_{02}$-like, (i) $LP_{31}$-like, and (j) donut shape*

For example, $LP_{01} = HE_{11}$, is normally present in the core, with usually the highest intensity. Its profile shape is similar to a Gaussian profile. Higher order modes such as $LP_{11} = HE_{21} + TE_{01} + TM_{01}$ or $LP_{21} = HE_{31} + EH_{11}$ have more than one intensity

maximum [144, 145]. Some of the effective indices were attributed to optical modes such as core modes, cladding modes or surface modes. For each wavelength it was possible to obtain a number of propagating modes. To ensure that they are all found, it was necessary to initiate the numerical mode solver with a range of trial initial conditions. In this case, the initial conditions comprised these 30 trial effective indices. Each initial condition resulted in a mode profile and its associated index satisfying Equation 3.2 and the boundary conditions for the refractive index profile. Fig.3.4 shows examples of optical modes which were found at given wavelengths of the range: $\lambda = 950$ *nm* to $\lambda = 1200$ *nm*. Following Fig.3.4, Fig.3.4a shows a fundamental-like mode ($LP_{01}$-*like*). We observed two degenerated $LP_{01}$-*like*. These degenerated $LP_{01}$-*like* were also found in the literature [8, 77, 140, 143, 146, 147]. According to the probability of experimental generation of higher order modes, only a few were chosen to be represented here. Fig.3.4b-Fig.3.4e show higher order modes such as $LP_{11}$-*like* with the different geometric orientation of the electric field distribution [56, 140, 146–149]. Fig.3.4a and Fig.3.4b present $LP_{11}$-*like* with the right-elliptical and the left-elliptical orientation, respectively. In Fig.3.4c and Fig.3.4d, we can see $LP_{11}$-*like* with a vertical and a horizontal orientation, respectively. Fig.3.4f and Fig.3.4g present $LP_{21}$-*like*. These kind of modes were also observed by [147, 149]. In addition, higher order modes are shown here, such as: $LP_{02}$-*like* in Fig.3.4h and $LP_{31}$-*like* in Fig.3.4i [146–150]. Fig.3.4j illustrates a field distribution which has a *donut* shape. It is not a single optical mode, but can be associated with superposition of $TE_{01}$ and $HE_{21}$ type modes. This kind of field distribution has also been observed in the literature [151].

Fig.3.5 presents the $n_{eff}$ as a function of wavelength. The results were obtained by Comsol for optical modes that resemble *LP* modes. However, for the region of $950\,nm < \lambda < 1300\,nm$ we could observe three air-core modes, which resembles: $LP_{01}$-*like* (red dot), $LP_{11}$-*like* (blue dot), $LP_{21}$-*like* (purple dot). As well, for fundamental-like modes ($LP_{01}$-*like*) in the range close to: $950\,nm < \lambda < 1150\,nm$ we found in the simulation two degenerate fundamental-like modes. As expected, the effective index of the fundamental-like mode was about 0.99 and the effective index of higher order modes is lower than the effective index of fundamental-like mode (see Chapter 2). This region, where $LP_{01}$-*like* appeared, is close to the bandgap defined by the fibre used in [58, 77] (as explained in above sections). For this reason, the region (blue dashed area) was associated to be the main region of propagation for this fibre and is called: *the propagation band*. Note here that many other solutions outside the band were obtained as: surface modes and leaky modes (grey dots), $LP_{11}$-*like*, $LP_{21}$-*like*, $LP_{12}$-*like*, $LP_{31}$-*like* and $LP_{51}$-*like* and $LP_{61}$-*like*.

Figure 3.5: *Graph of the effective index and wavelength for hollow-core PCF 1060, where dots show the field pattern which resembles optical modes for standard optical fibre as dots: red LP$_{01}$-like, blue LP$_{11}$-like, purple LP$_{21}$-like, violet LP$_{12}$-like, dark yellow LP$_{31}$-like, yellow LP$_{51}$-like, magenta LP$_{61}$-like and light-grey dotes are surface and leaky modes, the dashed area represents the propagation band*

Simplifying interpretation of this graph, we may expect that the fibre with such a geometry (HC PCF 1060) supposed to guide (along its core) a certain wavelengths from the propagation band. The results of our simulation model are in agreement with the theory presented in Chapter 2 and in the literature [1, 58, 82, 140, 148].

Therefore, we can estimate the guidance changes when applying changes to the refractive index within air-channels. In the first test, the refractive index was changed inside each channel. Using the subdomain settings in Comsol the refractive index of all cladding holes and core were changed to 1.33 (see: Fig.3.2b).

Fig.3.6 illustrates the field pattern analysis for effective indices as a function of wavelength. This graph contains two layers. The first layer on the left *y*-axis shows the shifted band (green dashed area) located in the region close to 450 *nm* < λ < 650 *nm*. Here we can find the field pattern, which resembles optical modes like: *LP$_{01}$-like* (red dot) and higher orders: *LP$_{11}$-like* (blue dot), *LP$_{21}$-like* (purple dot), *LP$_{02}$-like* (black dot), and *LP$_{31}$-like* (green dot). In order to visualise the result of changing the refractive index, we attach the second layer in Fig.3.6. In this layer (on the right *y*-axis) is presented this band for the unchanged refractive index (blue dashed area). This is the same band, which was plotted in Fig.3.5, however, there are no more surface or leaky modes plotted. By comparing Fig.3.5 and Fig.3.6, we can observe that modes such as

Figure 3.6: *Graph of modes analysis for HC-PCF 1060, where the left y-axis shows the first layer and results for the changed refractive index for 1.33 within all air channels, the green dashed area shows a new shifted band. The right y show the second layer and results for the unchanged refractive index with the blue dashed area as the propagation band. Dots for both layers indicate optical modes as: red-LP$_{01}$-like, blue-LP$_{11}$-like, purple-LP$_{21}$-like, black-LP$_{02}$-like, green-LP$_{31}$-like*

*LP$_{01}$-like*, *LP$_{11}$-like*, and *LP$_{21}$-like* are shifted to a new propagation band, as expected by [83] and Equation 2.7. Also, in this band (at left side of the graph) we can also observe higher order modes such as *LP$_{02}$-like* and *LP$_{31}$-like*. It can be observed, that the shifted band looks narrower in comparison to this obtained for the air-core. This has been studied before in [82, 83]. Unlike a conventional fibre, the fibre core of HC PCF 1060 is not a perfect circle, but had a six fold symmetry and may cause a mode polarisations splitting [56, 82]. Due to that the propagation band for PCFs (for silica 1.45 and 1.00) is probably supported by two polarisation states of optical modes, however, shifted with respect to each other (for example we could create one band for just one kind of polarisation state). For the analysis described in Fig.3.5, polarisation states of any observed field patterns were not distinguished and we observed all patterns in one propagation band. However, reducing the contrast of the refractive index (silica 1.45 and water 1.33) causes overlap of the bands. As a result, the overall band (i.e the shifted band) looks *narrower* [56, 82].

Fig.3.7 presents the results of the second test. Here the core refractive index only was changed to 1.33. The refractive index of the microstructure cladding was not modified. We expect to observe the change from PBG guidance to index guiding, as explained in Chapter 2. The field pattern analysis was verified in the range: 500 *nm* < λ <

Figure 3.7: *Graph of mode analysis for hollow-core PCF 1060 with changed refractive index for 1.33 only within the core of the fibre; dots show the modes as: red-LP$_{01}$-like, blue-LP$_{11}$-like, violet-LP$_{21}$-like, black-LP$_{02}$-like, green-LP$_{31}$-like, the dashed area represents the transmission windows*

1700 *nm*. A model of light guidance was analysed to wavelength 1700 *nm* due to the detection limit of the Optical Spectrum Analyser (OSA) (see Section 3.3). However, we presented only the analysis up to wavelength 1000 *nm* (red dashed line). This is due to high water attenuation above this wavelength [86]. The fundamental-like mode, *LP$_{01}$-like*, and higher order modes were found for wavelength from 600 *nm*. For shorter wavelengths, the effective indices of the fundamental-like mode would have a higher value than the refractive index of the core material (blue solid line). For this reason, the analysis was limited to this point as shown with a red-dashed line at the left side f the graph. It is worth noticing that for this case, any leaky or surface modes were attached to the graph. However, such a broad transmission window presented inside the red dashed area suggests that the guiding mechanism is no longer due to PBG effect, but probably an index-guiding mechanism instead [17, 56, 143].

In order to verify the relation between the wavelength and refractive index filling of the core at which refractive index of the core equals to the effective index, additional analysis was implemented. Fig.3.8 represents only *LP$_{01}$-like* for the change of refractive index (only in the core) to 1.33 (blue dots) and to 1.34 (green dots). The guidance with the fundamental-like mode propagation was observed at the 600 *nm* wavelength for 1.33 (green solid line) and for 1.34 at 570 *nm* (blue solid line). Between two fundamental-like modes lines, we noticed a shift of 30 *nm* for the analysed wavelength. In this graph (Fig.3.8), we only present the transmission window for refractive

Figure 3.8: *Graph of the fundamental-like mode analysis for the filling core with a refractive index material: for n=1.33 (blue dots) and n=1.34 (green dots)*



Figure 3.9: *Graph of the effective index for the wavelength as a function of wavelengths (purple crossed circles)*

index of 1.33 and 1.34.

However, this shift was observed for many other refractive indices values. These results are shown in Fig.3.9. Here, the range of core refractive index material was changed between 1.23 and 1.43. The obtained effective indices for the wavelengths are shown as purple crossed circles within the range 300 *nm* to 900 *nm*. The relation between the wavelength for the first observed fundamental-like mode ($LP_{01}$-like) to the effective indices is linear. Also, the increment of the refractive index in the core causes a blue-shift of the window of propagation.

## 3.3 Experimental results for light transmission in HC-PCFs

### 3.3.1 Characterisation of the light source

The supercontinuum source is a well known broadband light source. In this work, the supercontinuum signal was used as the light source for all experiments. The supercontinuum signal is generated, due to a number of nonlinear effects that act together upon a pump beam. This causes spectral broadening of the original pump beam inside the PCF. The supercontinuum can be created by four mechanisms: soliton fission [152, 153], self-phase modulation, four wave mixing rules and stimulated Raman scattering [154, 155].
More details about supercontinuum generation can be found in [10, 154, 156–162].

**Optical set-up for supercontinuum generation**



(a) *optical configuration*  (b) *the fibre input*

Figure 3.10: *(a) The schematic optical setup to generate the supercontinuum signal, where: (1) indicates the Nd:YAG laser, (2) is the focusing lens, (3) is highly-nonlinear PCF (b) the cross-section of HNL-PCF*

The optical configuration used to generate the supercontinuum light is presented here. Fig.3.10a illustrates a schematic of the optical setup. First, a Q-switched semiconductor pumped Nd:YAG laser (JDS Uniphase NP-10820-100) was used, with the laser specification in Table 3.1.

The Nd:YAG laser (no.1 in Fig.3.10a) was positioned on an aluminum block allowing a heat flow. A $x,y,z$-stage (Newport, 562F-XYZ) was used to hold an objective microscope lens (no.2) (Newport, $M \times 40$, $NA = 0.65$, $FL = 4.5$ $mm$). This lens focused the pump into a highly nonlinear PCF (HNL-PCF) (no.3) also on an $x,y,z$-stage. This particular lens had been chosen specifically for the focal spot diameter, which according to Newport specification and the laser beam diameter ($d = 0.2$ $mm$ in Table 3.1), was calculated as $d_{focal} \approx 3\mu m$. This spot fits to the fibre core diameter. This

| Wavelength | $\lambda$ | 1064 $nm$ |
|---|---|---|
| Peak power | $P_{peak}$ | 19.56 $kW$ |
| Pulse energy | $E_{pulse}$ | 10.7 $J$ |
| Pulse repetition rate | $T_{pulse}$ | 6.85 $kHz$ |
| Pulse frequency | $f_{pulse}$ | 0.15 $ms$ |
| Peak width | $\Delta t$ | 0.55 $ns$ |
| Beam profile | $TEM_{00}$ | |
| Beam diameter | $d_{laser}$ | 0.2 $mm$ |
| Laser head dimension | $L \times W \times H$ | $100 \times 22.5 \times 31$ $mm$ |

Table 3.1: *The Nd:YAG laser specifications*

lens also was recommended by NKT Photonics since it provides a good result for supercontinuum generation using this particular fibre (HNL-PCFs). Fig.3.10b shows a cross-section of the input of HNL-PCF. This fibre was fabricated by NKT Photonics A/S. The fibre cladding diameter was a standard $d_{cladding} \approx 125$ $\mu m$ and the core diameter was $D_{core} \approx 4$ $\mu m$. The fibre length was close to 20 $m$ and was kept in its original fibre spool. One of the fibre ends was also held with a *x,y,z*-stage using a bare fibre connector (Newport, 561-FH). The small core sizes required critical alignment. In order to precisely position the fibre end-facet at the focal point of the lens (no.2), the *x,y,z*-stage holding the fibre was connected to nano-piezo-actuators (Newport, NanoPZ actuator PZA12). These actuators had a travel range of 12.5 $mm$ and minimum motion of 0.03 $\mu m$. It must be noted here that the quality of the fibre surface was crucial. Both fibre ends had to be cleaved and tested using an optical microscope before using this fibre. A standard cleaving fibre process (Fujikura High Precision Cleaver CT-32) was adequate for this purpose. In addition, one of the fibre ends, was connected to the FC fibre adapter. It allowed the fibre to be plugged into the optical spectrum analyser (OSA, ANDO AQ-6315E).

**Process of generating the supercontinuum**

The first issue to be addressed in generating the supercontinuum is careful alignment and this was achieved by observing the propagation of the light with a IR camera. While changing the *x,y,z*-stage once we could observe a light spot at the end of the fibre. Then, the fibre output (with a FC connector) was connected into the OSA. The laser peak at wavelength $\lambda = 1064$ $nm$ was normally detected. The OSA was set with a resolution of 2 $nm$ and a span 100 $nm$ centred at $\lambda = 1064$ $nm$. In this case, the scanning time of the OSA was fast enough to respond to any changes in the fibre position. When the fibre end-facet was closer to the focal point of the lens (the lens working distance was $WD = 0.5$ $mm$), the intensity of the signal ($\lambda = 1064$ $nm$) increased and started to

be broaden. At the final stage, the visible range of wavelengths was generated. This
caused the fibre to *glow*.



Figure 3.11: *The supercontinuum fibre in a spool, with example of the fibre glow*

This we can observe in Fig.3.11. Here the fibre has a *white* colour (pointed with arrow)
and we can see the fibre wrapped around the fibre spool. The supercontinuum beam,
at the output, was dispersed using a prism and directed to a screen. On the screen we
could see coloured light, which confirms the visible range generation.



Figure 3.12: *The supercontinuum profile detected with OSA, with a resolution* 10 *nm and inset
near-field image of the HNL-PCF fibre*

The observed spectrum from 500 *nm* to 1700 *nm* had almost constant intensity. At this
point the span of OSA was changed for its maximum detection range and resolution
to 5 *nm* or 10 *nm*. The inset in Fig.3.12 shows a near-field image of the output of the
supercontinuum fibre (i.e HNL-PCF). Fig.3.12 presents a spectral profile of generated
supercontinuum using the OSA (10 *nm* resolution). The spectrum begins at wavelength

$\lambda = 350\ nm$, and at wavelength $\lambda = 400\ nm$ the power decreases. It can be attributed to the negative value of group velocity dispersion ($GVD \approx -800\ ps/nm/km$) for the HNL-PCF at this wavelength [154, 157, 161, 163].



(a)

Figure 3.13: *Dispersion graph for HNL-PCF fibre according to [154]*

Fig.3.13 shows this dispersion curve for two optical modes: $LP_{01}$ and $LP_{11}$ according to [154]. Other characteristic points can be observed at wavelength $\lambda = 1064\ nm$. This belongs to the Nd:YAG laser pump. At wavelength, $\lambda \approx 1400\ nm$, we detected a light absorption peak due to the first order of OH-bond overtone [71].



(a)  (b)  (c)

Figure 3.14: *The cross-section images of HNL-PCF (a) with dusts on the fibre surface, (b) other example of the fibre contamination, (c) example of broken silica bridges in the microstructure cladding*

It is worth noting that the supercontinuum profile presented in Fig.3.12 was determined as the referenced spectrum. Any spectra that had a lower intensity and not a very broad spectral profile indicate that not enough beam power was launched into the fibre. One of the issues observed was very poor generation of the short wavelengths of the supercontinuum. This situation is also discussed and presented in the article on supercontinuum generation [157, 161]. In this case the following parameters should be cross

checked: beam deviation, lens cleanliness, and the fibre surface. The images below (Fig.3.14a, Fig.3.14b and Fig.3.14c) are examples of the HNL-PCF cross-section for which we could not obtain good results for the supercontinuum generation. Fig.3.14a shows the cross-section of HNL-PCF with some dust at the fibre surface. Fig.3.14b shows a clean fibre surface with only one speck of dust at the microstructure cladding (indicated with a red arrow). This fibre contamination was enough to cause difficulties with the supercontinuum generation as the referenced spectrum. The last image, Fig.3.14c, is the example of broken silica bridges between cladding holes (indicated with a red arrow). It can be attributed due to applying too strong a tension onto the fibre during the cleaving process.

## Optical configuration

This section presents light propagation within HC-PCF 1060 using the supercontinuum. The configuration shown in Fig.3.15 was used to study the transmitted spectra of HC-PCF 1060. The light source is the supercontinuum source as was demonstrated in the previous subsection.



Figure 3.15: *The experiment setup to detect transmission spectra, where: (1) shows the supercontinuum source, (2) is a collimating lens, (3) is a bandpass filter, (4) is a focusing lens, (5) is the fibre sample (HC-PCF 1060), (6) is a collimating lens (7) neutral density filters, (8) a CCD camera, (9) computer and software, (10) a collimating lens, (11) a multimode fibre, and (12) indicates an optical spectroanalyser*

A good alignment was ensured by using an optical rail. The SC light divergent from the fibre and was collimated by an infinity corrected lens (no.2) (Newport, $M \times 40$, $NA = 0.66$, $FL = 4.6\ mm$). In order to select particular wavelengths from the broad spectrum, a bandpass filter (no.3) was placed close to the lens (no.2). The filter was mounted inside a filter holder with 90° flip (Thorlabs, TRF90). It allowed quick insertion and removal of the filter into and from the beam line. Then, a focusing lens (no.4) was attached to the optical rail. The lens (no.4) was a microscope objective (Newport, $M \times 40$, $NA = 0.65$, $FL = 4.5\ mm$). It launched the beam into the fibre sample (HC-PCF 1060) (see no.5 in Fig.3.15). At this stage of configuring the optical elements, a

holding set-up for the HC-PCF 1060 had to be determined. The method for holding the fibre end depended on the fibre sample length. When the fibre length was $> 20$ $cm$, the fibre ends were supported by two elements. In addition, the fibres $> 30$ $cm$ had to be supported in order to keep them straight. However, a short fibres $< 10$ $cm$ were held by only one element. In this case, the fibre alignment was more difficult. Next, we added to the set-up an additional collecting lens (no.6), which was an infinity corrected lens (Newport, $M \times 40$, $NA = 0.66$, $FL = 4.6$ $mm$) to magnify the core image to the CCD. In order to ensure that light was correctly confined in the fibre core, we observed the fibre output. For this reason, we attached to the set-up a CCD camera (no.8) (Thorlabs USB 2.0) together with a neutral density filter (no.7). This filter protected the CCD camera and controlled the near-field images' contrast. According to the magnification of the lens (no.6) the image of the fibre end-facet was magnified $\times 40$. We also controlled capture recording and CCD integration time using the Thorlabs software (see no.9). When the field pattern analysis was completed, the CCD camera was taken out of the optical rail. In its place another detection element (lens (no.10)) was added. This lens collects the beam propagated through the HC-PCF 1060 and focused the beam into a detector. The microscope objective (Newport, $M \times 10$, $NA = 0.25$, $FL = 16.5$ $mm$) was placed in the working distance ($WD \approx 5.5$ $mm$) to the another element of the setup, which was a multimode (no.11) fibre (Thorlabs BFL 22-200, $NA = 0.22$, $d_{core} = 200$ $\mu m$, Vis-IR) with 3 $m$ of length. This fibre propagated wavelengths in the range of 350 $nm$ to 2500 $nm$. Both fibre ends were connected to FC fibre connectors. This allowed the fibre to be connected to the OSA (no.12) and test the fibre spectral profile. It is worth noting that all optical elements were held by a $x,y,z$ translation stages, which were controlled with micrometer actuators. These actuators were operated manually and adjusted the position over 0.2 $mm$ of travel with 0.1 $\mu m$ sensitivity. However, for the analysis of an unfilled fibre (HC-PCF 1060) we used nanoPZ-actuators (see section the supercontinuum generation) for high precision movement.

### 3.3.2 Experimental analysis for unfilled fibre

According to the optical configuration described above, the experiment began with the near-field image analysis. Two light beams were used. The first was the supercontinuum source. The second one was a filtered supercontinuum source. We selected the wavelength 1050 $nm$, using a bandpass filter (Thorlabs, centred at 1050 $nm$ with $\pm 10$ $nm$ full width at half maximum (FWHM)).

Fig.3.16 presents the observed modes for HC-PCF 1060. Fig.3.16a demonstrates the fundamental-like mode ($LP_{01}$-*like*) for HC-PCF 1060. This fundamental-like mode

(a) $LP_{01}$-like

(b) $LP_{11}$-like

(c) $LP_{11}$-like

(d) $LP_{11}$-like

(e) $LP_{11}$-like

(f) $LP_{21}$-like

(g) $LP_{donut}$

(h) leaky modes

Figure 3.16: *The near-field images, (a) $LP_0$1-like, (b-e) $LP_{11}$-like for different orientation of $\vec{E}$ field, (b) left-elliptical, (c) right-elliptical, (c) horizontal, (e) vertical, (f) $LP_{21}$-like, (f) $LP_{donut}$ and (g) leaky modes*

was also determined in the literature [83, 140, 164]. It was also possible to observe modes similar to higher order modes. Fig.3.16b to 3.16e presents the some higher order modes as: *$LP_{11}$-like*, in agreement with numerical model (see: Fig.3.4b to Fig.3.4e) [83, 140, 164]. In addition, higher order modes *$LP_{12}$-like* were also observed, as illustrated in Fig.3.16f. Fig.3.16g shows the higher order mode with a shape similar to a *donut* (*$LP_{donut}$*). On the other hand, Fig.3.16h presents *leaky modes* for which light is confined in the glass surrounding the core. In fact, leaky modes were also observed in

most cases.



Figure 3.17: *The transmitted spectrum for HC-PCF 1060 with a resolution 5 nm for the fibre length of 0.3 m*

Note, that the CCD camera had an attached IR filter. The observed colours for wavelengths of near infrared cannot be attributed to their colours. For example, wavelength 800 *nm* was found to be shown with a pink colour, the wavelength 1060 *nm* was recorded as blue. Colours observed in the visible range corresponded to their actual values.



Figure 3.18: *The transmitted spectrum for HC-PCF 1060 with a resolution 5 nm for the fibre length of 7 m*

Fig.3.17 shows the spectral profile of transmitted light through 30 $cm$ of HC-PCF 1060. The highest power is centred at $\lambda \approx 1060$ $nm$, as expected. We can observe also some intensity peaks at wavelengths $\lambda \approx 750$ $nm$, $\lambda \approx 560$ $nm$ and $\lambda \approx 470$ $nm$, respectively. These wavelengths may be also guided within the fibre core, however, with some higher order modes.

Furthermore, a longer fibre of 7 $m$ was also tested. Fig.3.18 shows a transmitted light for this fibre. The transmitted spectrum demonstrates that the wavelength ($\lambda \approx 1060$ $nm$) still dominates and does not change its power level. According to the fibre specification, this fibre was designed to only guide $\lambda = 1060$ $nm$ with an attenuation 0.1 $dB/m$ [83]. The 7 $m$ fibre should have only 0.67 $dB$ lower intensity at $\lambda = 1060$ $nm$. The situation changes at the left side of the spectrum. As we can see, the intensity peaks and light between these peaks have a lower intensity level. It can be associated to larger incident angles for higher order modes for HC-PCFs [60]. Similar effects of decreasing intensity of higher order as a function of the fibre length were observed in the literature [165].

In the following discussion, we once again investigate the PBG guidance observed in Fig.3.17. It was assumed that light with the highest power (as shown in Fig.3.17) was due to PBG guidance in the core, and probably with $LP_{01}$-*like* mode at 1060 $nm$. The remaining wavelengths were either highly attenuated as above or leaked through the cladding. The fibre of 30 $cm$ length was analysed once more. However, in this case the supercontinuum light was filtered at different wavelengths. The selection of particular wavelengths was determined by bandpass filters (Thorlabs). They were placed as shown in Fig.3.15 (see: (no.3)). The filter transmitted certain wavelengths (described for each image in Fig.3.19) with $\pm 10$ $nm$ of FWHM. We investigated the output of the fibre with CCD camera for the following wavelengths: 490 $nm$, $< 550$ $nm$, 560 $nm$, 650 $nm$, 740 $nm$, 750 $nm$, 800 $nm$, and 1060 $nm$. Fig.3.19a shows a near field image at wavelength 490 $nm$. We can see that the light is present within the microstructure cladding. We were expecting to observe light confined in the core of the fibre due to the observed fourth peak at 490 $nm$. However, it was not possible to couple light to the core, and only leaky modes were observed. For this reason, we replaced the bandpass filter for a low-pass filter at wavelength 550 $nm$. This filter transmits a number of wavelengths shorter than $\lambda < 550$ $nm$.

Fig.3.19b shows evidence of light in the core (white spot in the fibre core). It is assumed here that we can observe the mixture of modes. Fig.3.19c and Fig.3.19d are examples of light in the cladding and within the silica surrounding the core (green and red dots spread to the cladding) for wavelengths 560 $nm$ and 650 $nm$, respectively. Referring to 730 $nm$ light is confined in the core as shown in Fig.3.19e (bright orange

(a) 490 *nm*          (b) $< 550$ *nm*

(c) 560 *nm*          (d) 650 *nm*

(e) 740 *nm*          (f) 750 *nm*

(g) 800 *nm*          (h) 1060 *nm*

Figure 3.19: *The near field images for a different band pass filters (a, c-f), where (b) is for a low-pass filter*

spots in the core). In addition, we can observe a tiny red dot in the centre of the fi-bre core (Fig.3.19f) at wavelength 750 *nm* probably indicating coupling with a higher order-like mode such as $LP_{02}$-*like* . Longer wavelengths should also be leaked into the fibre cladding. This is shown in Fig.3.19g at $\lambda \approx 800$ *nm* as surface modes in the microstructure cladding appear (pink dots around the core). Finally, Fig.3.19h resem-bles the fundamental-like mode at 1060 *nm* which belongs to the propagation band as

expected due to Fig.3.5, but still showing leaking (or surface) modes.

### 3.3.3 Analysis for the filled fibre

In order to experimentally analyse the changes in the refractive index within all fibre capillaries, the fibre was fully filled with water. The refractive index of air-channels was changed to $\sim 1.33$, instead of 1.00.



Figure 3.20: *The transmitted spectrum of* 24 *cm HC-PCF filled with water, with attached near-field image at the upper corner*

Fig.3.20 presents the spectral profile for this fibre. Here the transmitted spectrum is shifted to the visible range as expected from Chapter 2, with the peak of the highest intensity observed at wavelength $\lambda \approx 600$ *nm*. No other peaks were observed for the applied region. The CCD image at Fig.3.20 (inset) shows strong coupling at the core (red colour) with some surface modes and light within the microstructure region. It was also observed that the shifted band looks narrower than that observed in Fig.3.6.

For selectively filled fibre (i.e. when only the core is filled, the refractive index changes to $\sim 1.33$) results are presented in Chapter 6.

## 3.4 Summary

In conclusion, the HC-PCF 1060 has been both numerically and experimentally investigated.

The fibre structure and light guidance characterisation were realistically represented using the Comsol. The mode analysis was investigated for wavelength as a function of effective index. We have demonstrated that there is the propagation band with the highest power for a mode resembling $LP_{01}$-*like* in the range of wavelengths from $\lambda = 950$ *nm* to $\lambda = 1150$ *nm*. We observed the presence of some higher order modes, surface and leaky modes. The numerically obtained field patterns were also found experimentally. We have shown that the fundamental-like mode propagation was experimentally generated only for wavelength $\lambda = 1060$ *nm* and belongs to PBG guidance. The simulated model is in good agreement with experimentally obtained results, and is in good agreement with other results reported in the literature [56, 82].

The light guidance within the air-core, according to the PBG effect is possible. The changes in refractive index resulting in a band shift were numerically found and experimentally shown.

In addition, we have presented a change in refractive index only for the core of the fibre which causes changes in light guidance. Instead of the PBG guidance, a broad transmission window was seen. We have also found a following relation between refractive index and spectrum. Increasing the refractive index of the core in comparison to the microstructure cladding causes a broadening transmission window, a decrease in the core index shifts the spectrum in the direction of longer wavelengths.

The numerical and experimental assessments here show that HC-PCF can be a good candidate for sensing. The sample can be positioned inside the fibre capillaries, modifying its guidance properties. Applications are discussed in Chapters 5 and 7.

# Fibre filling process

## 4.1 Introduction

In this chapter a new device to measure liquid viscosity is proposed which relates the observed filling time to the fluid viscosity. This is a new application of HC-PCFs, which we called *a nano-litre fibre viscometer* [44]. Forward testing the HC-PCF as a viscosity sensor, the filling of the capillaries of HC-PCFs must be investigated. The filling of HC-PCFs can be broadly placed into two categories: fully filled and selectively filled. The first occurs when all capillaries (the core and cladding) of the HC-PCF are filled with a fluid, which shifts the propagation band as shown in Chapter 2 and 3 [83]. Index-guiding, however, occurs when only the core is filled. This might also happen when the core and some of the surrounding capillaries are filled (but not all) [56]. The number of filled capillaries can be selected using well known methods established for selective filling techniques [20, 166, 167].

One of the first methods to fill the core of the fibre only is a multi-step injection cure cleave method. This method requires four steps of fibre preparation with UV curable polymer (NOA73) [166]. First, the NOA73 polymer is injected into the fibre capillaries (the core and claddings'). The fibre core has a larger diameter than the surrounding cladding capillaries; hence, it is filled in a shorter time, compared to the capillaries in the cladding. Then, the polymer is cured by ultraviolet (UV) radiation. The fibre length is side-scanned until a point is found, where the core is filled (but not the cladding). The fibre is cleaved at this location. The result is the fibre with a blocked core. At this stage, once again the fibre is filled (as the core is blocked): NOA73 polymer fills the cladding capillaries and the UV radiation cures the polymer. Once more, the fibre is side scanned and then again cleaved at the point where the core is empty and cladding holes are blocked. This results in a fibre, with blocked cladding holes and an empty core. This only allows the core to be filled when a liquid is introduced into the fibre. However, due to the four steps of the fibre preparation, this method is quite time consuming [87, 166, 168].

Alternatively, the core may be filled by forming a side hole that penetrates through the cladding and into the core. The method of creating a side hole in the fibre requires

the application of high pressure, to one of end of the fibre. First by the other end of the fibre must be sealed by heating the fibre (e.g. using a fusion splicer). At a sufficiently high pressure, the core expands at the weakest point (close to the collapsed region) creating a side hole and collapsed cladding holes [20].

The other common method of selectively filling the fibre is a fusion splicing method [167]. In comparison to the previously described methods, this technique requires only one step of fibre preparation. By carefully selecting the electrode power (called: arc power) and arc time from a programmable fusion splicer, it heats one end of the fibre exposed to the electrodes. It results in melting the cladding capillaries, leaving the core channel open. Due to the minimal number of steps in this procedure, this method was chosen in this experimental work.

This chapter presents tests of selective and non-selective fillings of HC-PCFs, and begins with an experimental presentation of the fusion splicing method. Also, the fibre filling study includes two scenarios: with and without external pressure. The background of the filling process is described in Chapter 2 [91].

## 4.2 Experimental investigations of the fusion splicing method

While the general principle used to block the capillaries of the fibre cladding is known [167], optimisation of the process for HC-PCFs was necessary and is reported here.



Figure 4.1: *The scheme of the collapsing process,(a) end-facet of the fibre before collapsing, (b) schematic drawing of a cross-section of the fibre during collapsing,(c) end-facet of the fibre after the collapsing process*

Fig.4.1 shows the schematic of preparing the HC-PCF for selective filling, using the fusion splicing method. With a fusion splicer (Fujikura FSM - 45PM), two previously cleaved ends of HC-PCFs, as shown in Fig.4.1a, were placed in the fibre holders and then placed in the splicer. One of the fibre ends was placed at the right side and another

at the left side at a (4 *mm*) distance from electrodes placed at the centre. The fibres were positioned perpendicularly to the two electrodes. Fig.4.1b presents a drawing of the side view of this fibre. The parameters in a fusion splicer have been modified. The gap was set to the maximal value (50 $\mu$m) and minimal overlap (1 $\mu m$). All pre-fusion parameters were switched off, the fusion power time (arc 1 time) was reduced to 480 *ms* (step of changing arc time was 10 *ms*) and the applied electrode power (arc 1 power: red arrows) was around 3.85 *W*. Fujikura Fusion Splicer 45PM gives the power in *bits*, which can be recalculated into *Watts* (25 *bits* = 3.85 *W*). The step for changing arc power was 1 *bit*. Both fibres were automatically moved one above the other between two electrodes. The electrodes were positioned perpendicularly to the fibres. Due to this fibres position, the power was applied at a distance of around 80 $\mu m$ from the fibre ends. Fig.4.1b shows a point (red arrows) where the arc power was applied. The arc power did not splice the fibre end-facets as a result of the changed parameters in the fusion splicer. This leads to the partial melting of the tips of the fibre without splicing. Fig.4.1c shows the changed cross-section of the fibre entrance. At the centre is a dark spot in the open core entrance surrounded by a white ring. This is melted glass in the cladding. After the arc power is applied the fibre is in a *collapsed* state from its original *uncollapsed* state.



|     |     |     |
| --- | --- | --- |
| (a) | (b) | (c) |

Figure 4.2: *SEM images of the tip of HC-PCF 1550 fibre, where (a) shows an example before collapsing, (b) an example of the fibre after collapsing, and (c) the same fibre output after collapsing with higher magnification*

Using a scanning-electron microscope (SEM) we could observe the tip of the fibre. In detail Fig.4.2a shows an example of the fibre HC-PCF 1550 before the collapsing process. Fig.4.2b and Fig.4.2c show the collapsed part of the fibre HC-PCF 1550 and with a higher magnification, respectively. Both the collapsed fibres' end-facets are shaped like a *donut*. Other examples of the modified HC-PCF 1060 fibre structures are shown in Fig.4.3. These pictures were captured using an optical microscope (Nikon Eclipse ME600).

For comparison, the side views of the fibre before melting the tip are shown in Fig.4.3a. Here, we can see the fibre channels as white shapes along the fibre. However, the

Figure 4.3: *(a) the side-view of the fibre before collapsing; the side images of collapsed fibres, where different arc time and arc power were applied for: (b) 6.16 W/2.5 ms, (c) 4.18 W/500 ms, (d) 3.85 W/480 ms, (e) 3.71 W/460 ms, (f) 3.25 W/70 ms, and a dashed line indicates where the core diameter was measured*

white lines at the outer part of the fibre are caused by light reflection at the edges. Fig.4.3b shows the end of the fibre, to which 6.16 *W* of arc power were applied for 2.5 *ms*. A white circular shape at the end of the fibre shows that it is completely melted and there is no access to any channel. In the middle of the image is a small dark triangle, which is an opening of the core channel. Fig.4.3c shows the fibre's side view, to which a reduced arc power of 4.18 *W* was applied for an increased time of 500 *ms*. We can observe the core channel along the fibre (bright line at the centre of the fibre). However, this core line in the fibre tip compared to the core line in the lower part of the fibre looks very narrow. It may have collapsed. At the dashed line, the core diameter was measured and equals $D_{core} \approx 2 \ \mu m$. Compared to the uncollapsed core diameter ($D_{core} = 9.8 \mu m$), this diameter is much narrower. This may or not be sufficient for the liquid samples to access the core. This depends on the sample viscosity and density. In Fig.4.3d, the arc power was reduced to 3.85 *W* with a time of 480 *ms*. Here, the tip of the fibre is no longer sealed and there is an open core channel (white line at the centre of the fibre) with a measured core diameter at the dashed line ($D_{core} \approx 10 \ \mu m$). The core diameter equals the original diameter even after application of the arc power. These parameters were found to be the best in achieving access only to the core channel, keeping the cladding capillaries closed. It was also observed, that in order to fill the core, the core itself cannot be affected by the arc power. It must keep the same diameter as before the collapsing process. This observation was established after a large number of experiments with filling the fibres. However, it was also observed that the access to the number of capillaries in the cladding may be controlled using the same rigour. Fig.4.3e is one example where the applied arc power was 3.71 *W* for 460 *ms*, resulting in a diameter of the uncollapsed channel at the dashed line of $D_{core} \approx 14 \ \mu m$. For this example, it is assumed that a

sample may access the core channel ($D_{core} = 9.8$ $\mu m$) and in addition to the capillaries of the first ring around the core ($d_h = 2.7$ $\mu m$). Then $d_h + d_h + D_{core} = 15.2$ $\mu m$. In the last example, Fig.4.3f shows the tip of the fibre, to which was applied 3.25 $W$ power for an extremely short time of 70 $ms$. Such power and time reduction causes only the collapse of the outer rings. The measured diameter of the uncollapsed part of the fibre as $d \approx 45$ $\mu m$. It is assumed that the sample fills the core and seven rings of cladding capillaries. The amount of control over the collapsed features of the fibre makes this method an optimum choice for selective filling purposes.



Figure 4.4: *Graph of data for collapsing fibre channels as a function of arc power*

The dashed line in Fig.4.3 shows how the diameter of the core channel was measured using Nikon software at the narrowest part of the collapsed section of the fibre. Taking into consideration measurements close to fifty fibre samples and presenting them as a function of the arc power and arc time, allows approximating an optimum of the arc power and time. Thus Fig.4.4 presents the changes of the fibres internal diameter by applying the arc power in the range of 3.72 $W$ to 3.85 $W$ (open purple circle). Fig.4.5 shows the changes within the fibre when a different arc time in the range of 440 $ms$ to 500 $ms$ was applied (open green triangles). Each data point in these graphs are an average over ten measured points. It is worth noting here that the aim of collecting this data was to find the optimum parameters of the fusion splicer in order to keep only the fibre core channel open for the sample. Here, we analyse the data points around 10 $\mu m$ (the HC-PCF 1060 core diameter) as for example the fibre tip shown in Fig.4.3d. During the number of observation, it was found that the fibres sample for which the measured diameter equal lower than 12 $\mu m$ (upper black line in Fig.4.4), also kept only the core channel open. According to the dimension of the cladding holes

($d_h \approx 2.7\ \mu m$), it is hardly ever possible that the core and some cladding capillaries would be not affected. For this reason, the 12 $\mu m$ was established as a critical value at which we may achieve only the core channel open. Furthermore, the diameter of 7.5 $\mu m$ (lower black line in Fig.4.4) also caused the collapsing of all capillaries except the core channel into the cladding. However, it was observed that the sample could not fill the fibre core. One may consider this observation as a consequence of the strong deformation of the core channel. For this reason the lower black line was introduced at 7.5 $\mu m$ as a critical value at which we may expect that only the fibre core is filled with the sample. Assuming that the target diameter at the narrowest point of the collapsed tip is in the range of 7.5 $\mu m - 12\ \mu m$ (area between black solid lines), within this range we have found 25 data points. Also, it was discovered that the arc power of 3.85 $W$ shows the highest concentration of points (14 of 25 points, which are in the target interval) close to the optimum value for keeping only the fibre core channel open. For the arc power lower than 3.85 $W$, it was observed that in addition to the fibre core, some other random capillaries of the first ring, located next to the fibre core, were also opened as for example the fibre sample shown in Fig.4.3e.



Figure 4.5: *Graph of data for collapsing fibre channels as a function of arc time*

Fig.4.5 presents the impact of the arc time on the fibre tip. Data points of this graph were collected by applying a fixed power for different periods of time to the fibre tip. Similar to the above analysis, one can observe that the highest number of points (11 of 25 points, which are in the target interval) is for the arc time of 480 $ms$. The arc time of 480 $ms$ was discovered to be optimum value in order to keep only the fibre core channel open. Fig.4.4 and Fig.4.5 indicate that decreasing the arc power and time

causes an increase to the number of open fibre channels within the collapsed fibre-tip.

| Uncollapsed fibre channels | Arc Power (W) | Arc Time (ms) |
|:---:|:---:|:---:|
| The fibre core | 3.85 | 480 |

Table 4.1: *The optimum parameters of arc power and arc time for keeping only the fibre core channel open*

In Table 4.1 are shown these parameters of arc power and arc time, which have been found as the optimum values (according to results presented in Fig.4.4 and Fig.4.5). It is worth noticing that these parameters (3.85 *W* for 480 *ms*) afterward were applied for most of collapsing fibre processes. It may approximately give more than 200 of the collapsed fibres. Empirically we confirmed that these parameters were the optimum parameters for keeping only the core channel open. However, these parameters were determined for this fusion splicer (Fujikura FSM - 45PM) only. Any electrode replacement may require additional optimisation to establish a new range of arc power and arc time.

### 4.2.1 Impact of the changed fibre tip

As the air channels in the fibre tip have changed shape, the filling factors may also have changed. Thus, in this section we discuss the impact of the changed fibre tip for any changes of the filling time of the fibre. Fig.4.6a shows a fibre tip: a modified core channel (marked with yellow lines). The fibre tip is composed of two parts: element 1 and element 2. In element 1, the core diameter is greater compared to the core of the fibre before the collapsing process. In element 2 we can observe that the core diameter is much narrower in comparison to the first part of the fibre tip and to the standard core diameter of this fibre. These measurements were provided using Nikon software, which is a one of commercially available operating software for CCD camera attached to Nikon ME600 optical microscope.

Therefore, an investigation was made to analyse the impact of the changing core diameter in the collapsed fibre tip when filling the fibre with liquids. The summary of these tests is shown in Fig.4.6b, Fig.4.6c and Fig.4.6d. The first example (Fig.4.6b) uses W.B.Young's method [169]. This method provides a simplification of the collapsed tip (green solid lines in Fig.4.6b). In element 1 the diameter of the core equals $D_1$ (red arrows) and the curvature of the core channel is simplified to a rectangle (Fig.4.6b) with length of $L_1$. In element 2 the core diameter is narrower than the input of the fibre, and is labeled $D_2$ (red arrows in Fig.4.6a and Fig.4.6b) with length $L_2$. Then, taking into account this simplified structure with diameters $D_1$ and $D_2$ in Fig.4.6b, the

Figure 4.6: *The calculated tests for a filling time delay in collapsed fibres for (a) the side-view of the collapsed tip of the fibre with yellow solid lines showing the core channel shape, and red solid lines presenting parts of the changed tip of the fibre scheme of the core shape; (b) shows a simplified fibre shape (green solid lines) used for W.B. Young's method calculations with red arrows presenting two core diameters, (c and d) display a simplified scheme of the core shape for the inclination angle method calculations with red arrows showing direction of the capillary force*

delayed time ($\Delta t$) may be calculated using:

$$\Delta t = \frac{2\mu\Pi}{\sigma\cos\theta} \text{ and } \Pi = 2L_t{}^2[\frac{1}{D_1}(\frac{L_1}{L_t})^2 + \frac{1}{D_2}(\frac{L_2}{L_t})^2 + (\frac{L_1}{L_t})(\frac{L_2}{L_t})(\frac{D_2{}^3}{D_1{}^4} + \frac{D_1{}^3}{D_2{}^4})] \quad (4.1)$$

Here, $\mu_d$ is dynamic viscosity, $\sigma$ is surface tension, $\theta$ is the contact angle between liquid and internal surface of the capillary, $\Pi$ is an auxiliary constant. $D_1$ is the diameter of element 1 and $D_2$ is the diameter of element 2, $L_t$ is total length of the element and $L_1$ and $L_2$ are lengths of elements 1 and 2, respectively [169]. We calculated the delayed time ($t_d = -0.5\ s$) for five different collapsed fibres.

On the other hand, Fig.4.6c and Fig.4.6d present the inclination angle ($\alpha$) method. We used this method to calculate delayed time for another five different collapsed fibres. In this case, this method considers the impact of the curvature of the core channel. Here, the curvature of the core (yellow line in Fig.4.6a) may change ($\alpha_i$) the angle of the capillary force. There are two scenarios (Fig.4.6c and Fig.4.6d). The first one, Fig.4.6c, presents the capillary force entering into the core with a 90° angle. The force angle is changed just in front of element 2. In the second example, Fig.4.6d, we can see that the angle of force is changed in the input of the fibre. It enters the core not with a 90° angle, but with an $\alpha_i$ (i.e angle of core curvature). In both cases the capillary force equals [93, 170–172]:

$$F_c = D\pi\sigma\cos\theta\cos\alpha_i \quad (4.2)$$

Here $F_c$ is a capillary force, $D$ is the diameter of the analysed element, $\sigma$ is the liquid sample surface tension, $\theta$ is the contact angle described above, $\alpha_i$ is the angle of inclination. For both scenarios of the inclination method, the delayed time equals $t_d = -0.08 \ s$.

For the three calculations presented here, the value of delayed time was less than $0.5 \ s$. The changed tip of the fibre was only $100 \ \mu m$ long, which for $10 \ cm$ fibre length was only $0.1\%$ of the total fibre. Consequently, variations in the dimensions of the input of the fibre should not affect data in terms of recording the time during the filling process for collapsed and uncollapsed fibres.

## 4.3   Data for filling the fibres

Here, the experimental side of the fibre filling process is discussed. The illustration of the described setup is shown in Fig.4.7. As can be seen, it is a schematic of the optical microscope used (Nikon ME600). The fibre, represented by a yellow tube, was held vertically under the microscope objective. The first step of the fibre filling experiment, the fibre (usually of $4-8 \ cm$ length) was cleaved at both sides. The fibre length was measured with a ruler, for which the error equals $\pm 1 \ mm$. The microscope sample holder was modified in order to hold a fibre holder (Fujikura, FH 125 $\mu m$) and hence allow monitoring one of the fibre ends. The incident light (orange arrows in Fig.4.7) was focused at the fibre end-facet and the reflected light (violet arrows in Fig.4.7) was forwarded to a CCD camera connected to the upper part of the microscope. The other end of the fibre was allowed to hang freely. The fibre filling tests were performed for distilled water at $20°$ Celsius using a glass beaker. The filled beaker was placed on a linear translation stage mounted to the microscope bench, and then moved up.

In order to indicate the moment, when the fibre end-facet made contact with the liquid surface, the CCD camera was blocked. This part of the experiment was operated manually. Simultaneously, when the camera was blocked with the shutter attached in front of the microscope objective, the beaker was moved using the actuator of the translation stage. When the fibre end came in contact with the liquid, the shutter in the CCD was opened. As this process was manual, an error of $\pm 1 \ s$ occurred when determining the filling time. The detection of the filling time was recorded as an array of frames (captures) in time using the Nikon software. For example, the recorded movie of the filling fibre process started with the image of the fibre end-facet, similar to this shown in the first image of the lower panel in Fig.4.7. For a few seconds the captures are black, and then fibre end-facet appeared back. This frame was marked as the first capture ($0 \ s$) of the filling process of the fibre and it is shown as the first image in the lower

Figure 4.7: *The schematic drawing of a microscope setup to record a fibre filling process; at bottom is an array of images of the fibre end-facet recorded during filling of* 3 *cm of the fibre*

panel of Fig.4.7. The process was recorded till the fibre was completely filled. Due to a quick process of filling short lengths of fibre ($3-6$ *cm* took less than 1 *min*), the frame speed was applied as 5 *frames/second*. Here, the time error is $\pm 1$ *s* instead of 5 *frames/second* (which may equal $\pm 0.2$ *s*). This is because the opening of the shutter was done manually. The accuracy obtained was superior than previous recorded analysis [87]. In the second image of the lower panel in Fig.4.7, we can observe a white dot in the core of the fibre. This indicates the presence of the water in the core. The fibre core was filled in $5 \pm 1$ *s*. It took another 19 *s* to fill the first channels in the fibre cladding (white dots in the microstructure cladding in the third, fourth and fifth images in Fig.4.7). The complete filling of the 3 *cm* fibre was observed after $47 \pm 1$ *s* (the sixth image of Fig.4.7).

## 4.3.1   Delayed filling times for HC-PCFs

Throughout the filling experiments explained in the above section and displayed in Fig.4.7, the same sample of fibre was refilled several times. The aim of this experiment was to establish reusability of the fibres. After each refilling, the fibre was connected to a syringe filled with air the fluid sample was pushed out at least six times. Then the air from the syringe was pushed into the fibre and the fibre was disconnected. The syringe plunger was pulled out and the fibre was connected again. For the first filling of new fibres, a time delay was noticed in comparison to subsequent refilling. In order to analyse the difference in the filling time, emptying and subsequent refilling of the fibre samples were and the filling time only of the fibre core was recorded. Note here, that the fibre was filled fully, however, only the filling time of the core was taken for analysis (for example the only filled core at 5 *s* presented in Fig.4.7 with the second image).



Figure 4.8: *Graph of the filling process of three fibres with water, where: blue triangles indicate 64 mm fibre length, green squares indicate 51 mm fibre length, and red circles indicate 42 mm fibre length with black lines, which display the error bars. The solid lines show the theory line and dashed lines display the error range for the theory line*

Fig.4.8 shows the core fibre filling process for three different fibres, where experimental data points correspond to the length of the fibres at 64 *mm* (blue triangles), 51 *mm* (green squares), and 42 *mm* (red circles). The experimental data points have error bars such of ±1 *mm* and ±1 *s*. Using Equation 2.28 (as explained in Chapter 2), theoretical curves (solid blue lines in Fig.4.8) with respect to the measured core size (dashed blue lines) were fitted to the experimental data points. Twenty diameter measurements

of the core of HC-PCF 1550 using the Nikon software were taken and were approximated as $D_c \approx 11\ \mu m$, for which the standard deviation was calculated and equal to $\sigma \pm 0.4 \mu m$. The theory plot line has an error range shown with dashed lines, which corresponds to the calculated filling time for the fibre with a core diameter of $\pm 0.4 \mu m$, respectively. Compared to the theoretical filling time (solid line), it is easy to notice that the first filling deviates the furthest from the theory line.



Figure 4.9: *Graph of time delays for the first filling for three fibres: blue triangles indicate 64 mm fibre length, green squares indicate 51 mm fibre length, and red circles indicate 42 mm fibre length with black lines, which display the error bars. The solid lines show the theory line and dashed lines display the error range for the theory line*

Fig.4.9 presents the same experimental points as a function of the number of fillings to the fibre core filling time (s). It shows a difference between the first filling and subsequent fillings in comparison to the theoretical line (solid lines). It was observed before that the filling time for a glass capillary can be reduced by creating a wetting film [173, 174]. Not surprisingly, the optical fibre is based on glass. The first filling may leave a wet film on the glass. When the fibre was filled a second time, the fibre had a wet film on the internal part of the fibre and the filling time was reduced.

Although this glass behaviour was published earlier [32, 43, 90, 174, 175] the same behaviour was found for HC-PCFs [30]. Consequently the fibre core should be filled a minimum of two times, neglecting the first filling time. As well, the fibre core may be filled multiple times and then the average of filling time can be taken. Another suggestion is to create the wet film internally in the fibre core, then only one filling is required. It is worth noting here that this experiment and conclusions were provided for water only.

Figure 4.10: *Graph of comparison between the theory of filling (solid line) with error range for theory line (dashed lines) dictated by the core diameter variations. The experimental results for average time for number of fillings for fully filled fibres indicated by green diamonds*



Figure 4.11: *Graph of comparison between the theory of filling (solid line) with error range for theory line (dashed lines) dictated by the core diameter variations. The experimental results for average time for number of fillings for selectively filled fibres indicated by red circles*

Fig.4.10 and Fig.4.11 show the experimental results for filling the uncollapsed fibres (i.e. the original fibre) and the collapsed fibres (i.e. selectively filled), respectively. For both fibres types, the averages of all the filling times of the fibre cores (for minimum 6 filling times including the first filling) were plotted. For the original fibre core data are shown with green diamonds and for selectively filled fibre core with red circles. As

one can see, an agreement between the theory line and average of the experimental data for original and collapsed fibres can be observed. The standard errors are significantly smaller than the point size, due to that the errors bars are not shown in the graphs. Nevertheless, we can observe still some deviations from theory, the overall dependence seems to follow the predictions.

### 4.3.2 Overpressure filling

Up to now, no external pressure was applied and only capillary action took place. This technique is not sufficient for longer fibre lengths (e.g. than 10 *cm*) or higher viscosity fluids than water. Otherwise the time of the measurements would be too long and not reliable. Therefore one way of addressing this problem is to use a syringe pump set-up, which applies sufficient external pressure to fill the capillaries.



Figure 4.12: *The scheme of a syringe setup with joins between the syringe and the fibre*

Fig.4.12 shows a schematic of a syringe set-up, where the fibre was connected to a syringe. A syringe with a special luer tip was connected with a tip adapter *(Upchurch Scientific, p-662)* and united to a micro-tight adapter *(Upchurch Scientific, p-882)*. This element was connected with a length of capillary peek tubing *(Upchurch Scientific, FS-115 or 1571-12x)*. The micro-tight adapter was then attached to the fibre with peek tubing sleeve *(Upchurch Scientific, f-228)*. It was essential to remove the acrylate jacket of the first $2-3$ *cm* of fibre and fix the last tubing sleeve. This connection was sealed with ordinary silicone rubber. The syringe was positioned in a syringe pump (KD Scientific 4100) and a chosen flow rate $Q$ *(volume/time)* was applied. In order to calculate an applied external pressure $P_p$ the following equation can be used:

$$P_p = \rho Q^2 \text{ where } Q = vA \qquad (4.3)$$

Here $\rho$ is density, $Q$ is a flow rate, $v$ is a liquid velocity, and $A$ is an area. In order to control the external pressure applied to the input of the fibre, the diameter and length of each connector must be taken into account. In this project, we only monitored the input flow rate. For example, we tested that filling a 40 *cm* fibre with water and methanol,

for a flow rate of $Q = 25$ $mL/h$ took less than 3 $min$. For a high viscous solutions it was necessary to reduce the flow rate in order to avoid a sample leakage in the plastic connectors. For example, in order to fill a 35 $cm$ of fibre with the PVT (as explained in Chapter 5), the flow rate was reduced to $Q = 10$ $mL/h$. In this case, it took 5 $min$ to fill the fibre. The longest tested fibre length for the filling using the syringe pump set-up was close to 1 $m$.

## 4.4 Viscometer

In this section we present the use of a HC-PCF as a new device to detect liquid viscosity, which we call a *nano-litre fibre viscometer* [44]. In Chapter 2, the physical parameters of the fibre filling process were examined and calculated to approximate the filling time of a particular fibre length, and in this Chapter we experimentally observed the filling time. Using Equation 2.25 it is possible then to estimate what the viscosity is, if knowing density and surface tension. During the filling process we observed a strong effect of temperature variations in the detected filling time. As a consequence the viscosity of the liquid sample was changing. A 2 ° Celsius change in temperature results in a viscosity change of up to 6.9% of the viscosity of water, as described Chapter 2.

### 4.4.1 Nano-litre fibre viscometer demonstration

For a proof of principle investigation, we used experimental data shown in Fig.4.10 (for an uncollapsed fibre). The detection setup for these measurements is presented in Fig.4.7. The detected time and the filled length of fibre were used to calculate the ratio of viscosity ($\mu$) to surface tension ($\sigma$). Equation 2.25 is converted (Appendix B) to:

$$\frac{\mu}{\sigma} = \frac{t \cdot r}{2L^2} \tag{4.4}$$

Here $t$ is the fibre filling time, $r$ is the radius of the fibre core, $L$ is the filled fibre length, and $\sigma$ is the surface tension. More details about these parameters can be found in Chapter 2.

Table 4.2 shows results for a fibre HC-PCF 1550 (with core radius $r \approx 5.45$ $\mu m$), when the time for filling the core was recorded for fibres of particular length. The results (no.1) to (no.3) are for pure water accompanied by the comparison to the viscosity value ($\mu_{lit}$) found in the literature [98]. In result (no.4), the fibre was filled with iso-propyl alcohol (IPA). The surface tension ($\sigma$) was taken into account [97]. There we

| no | L | t | sample | temp. | $\sigma$ | $\mu$ | $\mu_{lit}$ | $\Delta$ |
|----|------|--------|------------|-------|----------|--------------|--------------|--------|
|    | *(mm)* | *(s)* |          | *(°C)* | *(dyn/m)* | *(mPa · s)* | *(mPa · s)* |        |
| 1  | 42   | 9.65   | pure water | 21.7  | 0.72     | 1.0735       | 0.9616       | 0.119  |
| 2  | 51   | 13.12  | pure water | 20.4  | 0.72     | 0.9990       | 0.9921       | 0.0069 |
| 3  | 64   | 19.17  | pure water | 20.7  | 0.72     | 0.9185       | 0.9849       | 0.0664 |
| 4  | 59   | 134.86 | IPA        | 20.0  | 0.23     | 2.4220       | 2.4000       | 0.022  |

Table 4.2: *The data points for the fibre filling process with water and isopropyl alcohol, and the calculated viscosity with a surface tension value from [97] with comparison to [98]*

could approximate only the viscosity. Using the above experimental parameters introduced in Table 4.2, the measured viscosity values is comparable to the viscosity referenced in the literature [98], as shown as ($\Delta$). The results show the nano-litre fibre viscometer demonstrate the proof-of principal for which estimates the ratio between viscosity and surface tension. In order to calculate the viscosity only, the surface tension of the fluid and density should be estimated using another techniques such as [44].



Figure 4.13: *The optical setup for nano-litre fibre-viscometer, where He-Ne is a helium-neon laser at 632 nm, HC-PCF 1060 is the fibre sample, CCD camera and PD indicates a photo-diode*

In order to improve results and design the fibre viscometer as a small and portable device, it was proposed to change the detection of the filling time from an optical microscope (Fig.4.7) to free-space optical set-up and a low-speed photo-detector. Fig.4.13 presents a nano-litre fibre viscometer prototype. Owing to changes in the light propagation mechanism due to the fibre (HC-PCF 1060) filling we used HeliumNeon (He-Ne), CW laser operating at a $\lambda = 632$ *nm* with power $P = 8$ *mW* (no.1). This specific wavelength propagated in the fibre core, when only the core was filled (due to the index-guiding explained in Chapter 3) and also in the fibre core for fully filled fibre with water.

Subsequently, the beam was directed to another arm of the optical configuration using two mirrors (no.2a) and (no.2b). The laser beam was launched into the fibre by a focusing lens (no.3) (Newport, $M \times 40$, $NA = 0.65$, $FL = 4.6$ *mm*). When the fibre

sample (HC-PCF 1060) (no.4) was positioned in the setup, the beam was focused to the fibre core and transmitted along the fibre. The other end of the fibre (i.e. output) was connected to a reservoir (no.5). This reservoir was a plastic box ($W = 19$ $mm$ and $L = 29$ $mm$), where one of the reservoir sides was a transparent. In order to connect the fibre and the reservoir a micro-tight adapter (Upchurch Scientific, p-882) was used (as presented in the syringe set-up in Fig.4.12). One end of the adapter was put inside the box and in the other end, the fibre with tubing (Upchurch Scientific, f-228) was inserted. The fibre output was positioned at the centre of the reservoir. The reservoir was filled with a fluid sample. The laser beam, which was transmitting through the fibre, was reflected from the travelled surface of the sample in the fibre core. The transmitted beam was collected by a lens (Newport, $M \times 20$, $NA = 0.65$, $FL = 4.6$ $mm$) (no.6). The outgoing signal was then turned to be collimated and forwarded to the beam splitter (no.7). The signal was divided, and 50% of the beam was forwarded to the CCD camera (Thorlabs, USB 2.0) (as explained in Chapter 3) and the other 50% was detected with the photo-diode (PD) [44]. The time error for this PD was about $\pm 0.02$ $s$. The time detection was improved $\times 50$.

This presented optical configuration in Fig.4.13 was then tested for the viscosity detection based on solutions of different concentration of glucose in water [176], and were investigated by Laura Horan (PhD student in the PSG group). The aim for these measurements was to monitor the glucose level in blood using the viscosity changes. The detection of the glucose level is important for patients with diabetes, and is strongly investigated in the current time. It is worth to noticing, that these results were added to the patent application [44].



Figure 4.14: *The fibre core filling process with attached images from CCD camera during filling process*

Fig.4.14 shows one of achieved results. The performance of the system was characterised using a set of samples prepared from distilled water and anhydrous 96% Sigma-Aldrich D-(+)-Glucose. These were combined to create glucose solutions of concentrations typically found in blood plasma and spanning the hypoglycemic and hyperglycemic regions ($3 - 9$ *mmol/L*). Samples from each solution were introduced to various HC-PCF lengths ranging from 10 *cm* to 20 *cm*, where each fibre was used once. The reflection from the liquid surface inside the fibre were received at the PD. The PD detected a voltage *(V)* and collected signal was represented in the vertical axis of graph 4.14 as voltage *(V)*. The horizontal axis displayed the filling time *(s)*. Following the black line, at first we observed some light in the range from 0 *s* to 25 *s* which probably belonged to some light leakage inside the empty fibre. In addition, the output of the fibre was monitored with the CCD camera. In the first image attached to Fig.4.14 we could also recorded some red leaked light in the microstructured cladding. Next, the solution was added to the reservoir and the filling process began at 26 *s*, as indicated with *(t_{start})*. The voltage dropped. The laser beam began to be confined in the filled part of the core (yellow spots at the centre of the fibre) due to the changes in light guidance (referred as index-guiding). The moment when the core was completely filled was indicated by a peak of in voltage at 260 *s*, and is indicated with *(t_{stop})*. Note here that the fibre was filled fully, however, only the filling time of the core was taken into calculations. The temperature of the sample was also taken into account.



Figure 4.15: *The graph of surface to viscosity measurements for glucose solution at different concentrations for two different temperatures: red triangles display* 25° *Celsius, and blue circles show results for* 26° *Celsius*

Fig.4.15 shows the directly measured results for the batches of samples, at temperatures 25° and 26° Celsius shown with blue triangles and red circles in Fig.4.15, respec-

tively. Up to five measurements were taken for each sample, each using different fibre lengths. The sample standard deviation was 4.42 $m/s$ which can be seen from Fig.4.15. It can be primarily attributed to our length measurement with an accuracy of 0.1 $cm$. A solid line indicates a theoretical value of surface tension to viscosity as a function of concentration for 25° and 26° Celsius as red and blue, respectively. Fig.4.15 also presents an expected linear variation in filling time with concentration and a 1° Celsius shift resulting in a change in slope of 10%.

## 4.5  Summary

In summary, here we present a discussion of the fibre filling process. The fusion splicing technique was here chosen and implemented in order to selectively fill fibres. It was found, that this technique allows control of the number of open air channels in the fibre.

The fibre filling process was demonstrated. This process can be applied to a broad range of fluid samples with the advantage of not being complicated or time consuming. However, a time delay was observed for the first filling of the fibre with water. In addition, it was shown that the fibre filling is not limited to only filling with capillary action. Filling can also be performed by the application of external pressure using the syringe pump. A long piece of fibre or a fluid with a high viscosity and density may be inserted into the fibre without damaging the fibre structure; the process takes only a short time, only a few minutes.

Furthermore, the time to fill the fibre can be detected and has been proposed as a novel application for a HC-PCF. This may be successfully adapted as a new viscosity sensor technology. Therefore, applying HC-PCFs as sensors, in terms of positioning the sample inside the fibre is a completely reasonable and effective method.

# Integration of hydrogel with HC-PCFs

## 5.1 Introduction

In this chapter, instead of applying the aqueous solution into the HC-PCF we propose to use a special filling material. It was demonstrated in Chapter 2 that the PEGDA hydrogel is a good biomaterial in terms of DNA detection. The proposed filling here is designed to be attached to the inner fibre surface and fill the fibre volumetrically. It may avoid sample leakage, which may occur during measurements or fibre carriage [16, 24, 177]. As the filled fibre can be transportable, many optical tests can be applied and repeated. For instance, the fibre end-facet analysis using optical and fluorescence microscopes, tests of transmission spectrum, fluorescence detection as a function of fibre length, etc.

In fluorescence analysis using PCFs, for example, it has previously been shown that in order to avoid the leakage one of the fibre ends should be kept in the sample reservoir. This permitted a continuous contact between fibre end and sample [19, 26, 178–183]. However, if the fibre is in contact with the reservoir, a portion of the fluorescence solution in the reservoir would also be excited. Therefore, the results inside the fibre may be overestimated by the fluorescence in the reservoir. Another proposed solution to avoid the leakage involves bonding molecules to the glass surface. This was first proposed by [177]. For example, it was possible to attach antibody molecules to the glass surface inside the HC-PCF or labelled DNA probe [21, 184, 185], or quantum-dot labelled proteins in microstructured fibres [22, 23, 29, 180]. However, the overlap integral between the sample (attached molecules) and the fundamental mode of the excitation wavelength can be low. In our case, we may expect that the overlap integral between the excitation light and sample may be improved due to the fact that the sample (the hydrogel) fills entire core capacity.

In this chapter, the method of introducing the PEGDA hydrogel into the HC-PCF is explained. A technique of growing the PEGDA hydrogel inside the HC-PCF is adapted and improved from the standard bulk growth process outlined in Chapter 2. Steps for silanisation, followed by descriptions of the preparing solutions and conditions for hydrogel growth within the fibre are described. In addition, it is shown that

the hydrogel is covalently bonded to the internal surface. The filled fibre is tested as a sensor looking at the characteristics and distribution of the hydrogel through its length. The aim of this analysis is to use PCFs and hydrogel for labelled DNA probe detection.

## 5.2 Hydrogel morphology

In order to familiarise with the PEGDA hydrogel, here, we show microscope images of hydrogel. Fig.5.1 presents examples of 25% and 65% concentration of the PEGDA hydrogel grown on a glass slide.



(a)                              (b)                              (c)

Figure 5.1: *The SEM images of the PEGDA hydrogel with (a,b) 25% of concentration and (c) 65%. These hydrogel samples are grown on glass*

Fig.5.1a shows only the 25% concentration of the hydrogel. The structure looks uniform and homogeneous. However, with increasing magnification (shown in Fig.5.1b) we can observe that the surface is rough. The third example, Fig.5.1c, presents 65% concentration of the hydrogel with a high magnification. This image is attached here in order to show that the PEGDA hydrogel structure is porous. The observed lighter spots on its surface are pores.

| Concentration | Poly(ethylene glycol) (PEG) | 1-Vinyl-2-pyrrolidinone (VP) | Triethanolamine (TEOA) |
|---------------|-----------------------------|------------------------------|------------------------|
| 12.5% | 0.20 M | 0.019 M | 0.113 M |
| 25% | 0.40 M | 0.037 M | 0.226 M |
| 35% | 0.56 M | 0.052 M | 0.316 M |
| 50% | 0.80 M | 0.074 M | 0.452 M |
| 65% | 1.04 M | 0.096 M | 0.588 M |

Table 5.1: *Summary of polymers (PVT solution) concentrations used for the PEGDA hydrogel*

Here we characterise the hydrogel grown on a microscope slide to investigate the quality surface coverage, matrix regularity, and morphology of the PEGDA hydrogel. This

includes an analysis of the hydrogel surface and porosity, which may cause light scattering [111, 112, 186]. The hydrogel tests are based on imaging the hydrogel surface and its cross-section with the assistance of an optical microscope (Nikon Eclipse ME 600) together with a CCD camera and a scanning electron microscope (SEM Hitachi 700). Table 5.1 shows the various concentrations of the PVT solution, as described in Chapter 2. According to [123] it was expected that modifying the ratio between the three PVT compounds changes the network irregularities. These network differences may be observable using the optical or scanning electron microscope. For this reason, the PVT solution was diluted with phosphate buffered saline (PBS). In order to grow the hydrogel on slide it was necessary to silane the slides first. We describe the experimental aspect of the silanisation process and photo-polymerisation process in the next section of this chapter.



Figure 5.2: *Image of the hydrated state of 25 % PEGDA hydrogel grown on slide*

Fig.5.2 shows one of the first tests in SEM. In this example, the structure seems to be more solid than porous as these presented in Fig.5.1. When the hydrogel was hydrated, it was observed that it is not possible to identify any pores or voids. It is known in the literature, that to analyse the hydrogel morphology it is recommended to dry the hydrogel structure. Examples of the drying process of hydrogel can be found in [112, 113, 187]. In our case, the hydrogel samples were left in a container in a temperature controlled lab at $20°$ Celsius for three days. No additional technique was implemented for drying.



Figure 5.3: *The SEM images of 25% PEGDA hydrogel on a glass slide, for (a) and (b) with a different magnification, (c,d) is an increased region of (c) with minimised lines and sharpness, and increased contrast, (d) has maximised brightness of edges with shown an approximation of ellipse shape (yellow crosses and red line ellipse)*

Fig.5.3 presents the example of the dried PEGDA hydrogel sample, tested using SEM. The magnification was much higher than that available in the optical microscope. These images had a hue changed to blue in order to maximise the contrast in the structure. Fig.5.3a shows the image magnified to $\times 450$ and in Fig.5.3b the structure was observed at few times higher magnification. The porosity post-processing radius measurements were investigated for the cross-section (instead of the surface). The SEM images were analysed with the aid of Nikon software. Fig.5.3b shows some lighter spots (i.e. pores) similar to those found in Fig.5.1c. For this example, pores are called crests as shown by the yellow arrows. Dark grooves between them are called troughs (as indicated by the pink arrows). To give the reader a better view of the crests and troughs, Fig.5.3b has been cropped and only one square of Fig.5.3b as shown with a red square is expanded. This region has also had a hue changed to blue and the sharpness of lines minimised, with contrast increased to 35%. In Fig.5.3c we can see crests as lighter blue spots. In addition, the image of Fig.5.3d had the brightness of its edges increased, which allows crests to be observed as a growth of the surface. In terms of measuring this network, troughs are determined by a width, which were measured to be $0.79 \pm 0.05~\mu m$. Crests 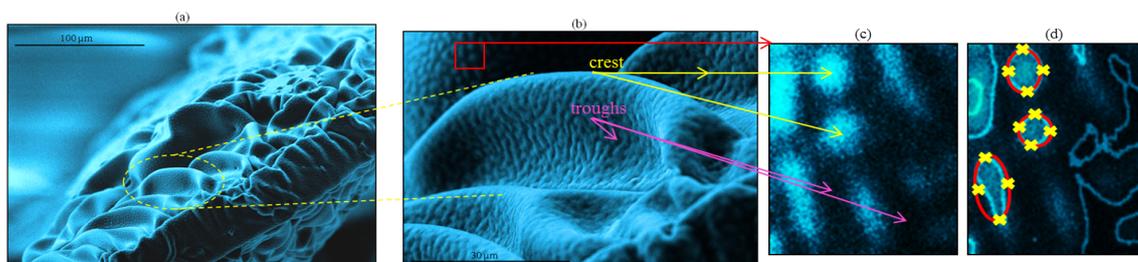have an elliptical shape, and were considered as a pores of the hydrogel. One may notice from Fig.5.3d that the area of each pore was marked using four points (see: yellow crosses) using Nikon software. Then the software approximated an ellipse shape (red line) according to the attached points, and the semi-axes of each ellipse were measured. The average dimension of the longer radii was $0.85 \pm 0.07~\mu m$, the shorter radii $0.42 \pm 0.02~\mu m$. For each hydrogel sample (12.5 %, 25 %, 35%, 50%, and 65%) twenty measurements of the radius were taken. The error in measurements was the standard deviation.

Fig.5.4 demonstrates the relation between the hydrogel chemical concentrations and the average pore radius. For comparison reason, the fibre core radius ($r = 4.85~\mu m$) of HC-PCF 1060 (blue solid line) is added. The hydrogel of 12.5% concentration is shown as a dark-cyan dot, 25% as a green dot, 35% is a purple dot, 50% as a navy-blue dot, and 65% as a pink dot. The error representing the standard deviation of twenty measurements is shown with a black line in the graph. One can see that the error range increased with the concentration due to higher variations in pore size. Also, Fig.5.4 shows that for a higher concentration of original PVT solution, the pore size increases in the hydrogel network. It was confirmed that 12.5% and 25% PEGDA hydrogel have nanoporous structure (as described in Chapter 2) [51].

In order to understand the hydrogel growth process within the core of the HC-PCF, we aimed to have the hydrogel structure as most homogeneous and uniform as was possible, and to minimised the dimension of the pores. According to this, we qualified

Figure 5.4: *Graph of the PEGDA hydrogel concentration as a function of average pore radii for: 12.5% is shown as a dark-cyan dot, 25% as a green dot, 35% as a purple dot, 50% as a navy-blue dot, and 65% is a pink dot; the blue solid line indicates the core radius of HC-PCF 1060, error bars are shown with black lines*

the concentrations below 35% as most suitable for use within the fibre (HC-PCF 1060). For the concentration 50% and 65% the pores dimension may be extended to 25% of the core area. In this case, for larger pore sizes, it is expected that the optical properties such as dispersion, attenuation and scattering may be present more significantly than for smaller pores. However, we have decided to integrate the 25% PEGDA hydrogel with HC-PCFs due to proven abilities to immobilise DNA within its structure. The 25% hydrogel had been successfully used for antigenicity and antibody measurements [47] and DNA immobilisation and hybridisation [45, 46]. These results encourage the use of such material for DNA immobilisation and hybridisation with a permeable character. In order to develop a new biosensor for DNA detection, these measurements were crucial for choosing the most useful hydrogel concentration

At the last part of the discussion about the hydrogel morphology it is worth noting that the pores in the PEGDA hydrogel are highly hydrated all the time. We could observe the presence of pores only for the dried state of the hydrogel. Thus, it can be concluded that pores are not empty spaces in the hydrogel structure, but are mostly filled with water. Therefore the refractive index differences should not have such a strong a impact when compared to the refractive index variations with air filled pores. The fibres filled by the hydrogel should be stored in water to avoid drying of the hydrogel.

## 5.3    Hydrogel for HC-PCFs

### 5.3.1    Silanisation process for fibres

In order to grow the PEGDA hydrogel within PCFs and on microscope slides, it is necessary to first chemically prepare the glass surface. This process is called *silanisation* and the background of this process was explained in Chapter 2. This is a standard process, which covers a silica surface with a silane agent. The silane agent attaches Eosin Y molecules to the glass surface. Eosin Y is then responsible for attaching the hydrogel to the glass. Eosin Y also begins the photo-polymerisation process.



(a) *New fibre*    (b) *APTMS filling*    (c) *Fully filled*    (d) *Eosin filling*

(e) *Eosin evidence*    (f) *Water filled*    (g) *Silanised fibre*

Figure 5.5: *The cross-section of HC-PCF 1060 for the silanisation process*

The silanisation was realised by filling the fibre with a series of solutions. In order to ensure good chemical surface coverage, one of the fibre ends was monitored using an optical microscope (Nikon Eclipse ME 600) with the other fibre end connected to a syringe pump as described in Chapter 4. Hence, by observing the filling of the end-facet of the fibre, the process of fibre silanisation may be controlled as presented in Fig.5.5. As a control process, we also silanised microscope slides. After the silanisation process, a silanised slide was used first for growing the hydrogel on its surface. When the hydrogel growth was complete, we found that the glass surface had been properly covered. If the hydrogel did not grow on the slide, it indicated that something did not go well. Hence, we have used the microscope slide as a surface quality tester as mentioned in Section 5.2.

Figure 5.6: *Graph of the silanisation process for one fibre as a function of time (min) with twelve described steps; the green circle symbol shows the time period for each step*

The silanisation process for a single fibre (green circle and green line) is presented in Fig.5.6. The x-axis shows the time scale and on the y-axis we can find a number of steps. The silanisation begins by preparing the first solution in order to attach to the silica the silane agent - APTMS (as explained in Chapter 2). A 19:1 ratio of methanol and distilled water ($MeOH : H_2 0$) was prepared (i.e. for a 100 $mL$ volume of solution 95 $mL$ methanol was added to 5 $mL$ of water). A 3% (v/v) solution of APTMS (3-Aminopropyltrimethoxysilane 97%) was diluted with the methanol/water mixture. For a 100 $mL$ solution, 3 $mL$ were taken away and 3 $mL$ of APTMS were added. Preparing this solution takes approximately 15 $min$. It is indicated as the $1^{st}$ step in Fig.5.6. This solution had been prepared in a biochemistry lab following a chemical protocol. Later, it was transported to the optical lab in order to fill fibres using a syringe pump and also to control the filling using an optical microscope. Next, the product solution was injected into the fibre air channels using the syringe pump set-up. Fig.5.5a presents the fibre cross-section before the silanisation process. Fig.5.5b shows a HC-PCF after filling with APTMS, while Fig.5.5c shows an example of fully filled fibre. In order to avoid air bubbles, which may affect the APTMS monolayer formation, the filling was kept a little bit longer until the solution formed a cap on the end of the fibre. The filling time of one fibre of $30-40$ $cm$ length, including connection to the syringe pump, as well as forming a liquid cap at the fibre surface took five minutes as marked in Fig.5.6 as the $2^{nd}$ step. At this stage, the fibre should be kept for one hour with the solution inside the fibre. This is a standard time, which allows APTMS molecules to covalently attach to the glass surface [188]. This is shown in Fig.5.6 (see the $3^{rd}$ step). Usually,

85

batches of six to seven fibre samples went through the silanisation process. At the moment when one fibre was filled with APTMS solution, the rest of the fibres were in the process of filling. It was observed that this delay did not affect the surface coverage quality. The hydrogel polymerised on the slide, which was kept for ninety minutes in the APTMS solution. This step in fact, can be extended up to two hours [188]. In the next step of the silanisation, fibres should be filled with methanol and quickly inserted into a heated oven in order to minimise the reaction between methanol and air at a normal temperature of $20°$ Celsius. It approximately took five minutes for single fibre, as shown in Fig.5.6 (see: $4^{th}$ step). Fig.5.6 also shows a step called *fibre transport* ($5^{th}$), as the samples were moved between labs and were exposed to air for another five minutes. In the case of batch preparing, the 30 *min* delay caused the silanisation to stop. Hence, the *methanol* filling step was modified. Removing this step, but maintaining the drying period. The fibres samples were inserted directly into the oven. This allowed drying of all fibres samples at the same time without any exposure to air. The drying step is required in terms of forming a covalent bond of APTMS to the glass surface. This process is presented in Chapter 2 in Fig.2.17. The reaction takes 120 *min*. We have not tested the impact of changing this period of time. It must be mentioned here that the microscope slide and fibres were found to be silanised without additional rinsing with methanol. Unfortunately, it was observed that the surface coverage was non-uniform in terms of covering the Eosin Y molecules on the glass surface. Fig.5.5g illustrates the silanised fibre with the green reflection. This colour depends on the concentration of APTMS and Eosin Y molecules. Therefore, by looking at the images of the *x*-section of the end of the fibre, the quality of coverage may be analysed.



(a) *Optical microscope*    (b) *Eosin Y emission*    (c) *Silicone reaction*

Figure 5.7: *The fibre's cross-section images of non-uniform surface coverage: by (a) an optical microscope, (b) a fluorescence microscope, (c) on optical microscope with silicone rubber contamination*

For example, Fig.5.7a shows non-uniform surface coverage. Here, the green areas are randomly present on the fibre surface. In order to confirm this observation this *x*-section was analysed with a fluorescence microscope, enabling a more accurate image of Eosin Y phosphorescence at $\lambda = 525$ *nm* (as described in Chapter 2). Fig.5.7a

and Fig.5.7b show an unsuccessful silanisation process. This suggests that APTMS molecules were not attached to the glass surface uniformly.The reason for the non-homogeneous surface coverage may be related to the APTMS solution. However, the other reason for this could be attributed to connecting the fibres to the plastic connectors with silicone rubber before silanisation. In order to connect fibres to a syringe pump set-up, the last connection (between fibre and tubing (F-228)) was sealed with silicone rubber and left to dry (as shown in Chapter 4). For this reason, fibres were prepared the day before. As expected, fibres were found with a particularly bright reflection as in Fig.5.7c. This may indicate that some of the evaporated molecules of silicone rubber entered the fibre and reacted with the glass surface. This could hinder attachment of the APTMS molecules to the glass surface. In terms of covering the microscope slide with APTMS, it was not necessary to have a uniform surface coverage. However, it was crucial for the fibres, in order to ensure uniform coverage by the hydrogel along the fibre length. After the described observation with silicone rubber, we tried to connect the fibre to syringe connectors just before the silanisation process. In order to improve the fibres internal surface coverage with the APTMS molecules, we implemented another change in the process. In addition, the reaction between APTMS and glass surfaces was supported by a sonication. This process helps to agitate molecules using ultrasound energy. The fibres and microscope slides were filled with APTMS solution. However, all of them were inserted into a jar with the APTMS solution and the jar was tightly closed. The jar was transported to the biochemistry lab and sonicated for one hour. This silanisation process for six fibres is presented in Fig.5.8. It is shown here, that part of the $3^{rd}$ step is marked as sonication and followed directly by the drying step. The fibres and slides were taken out of the jar and inserted into a previously heated oven. We found that direct insertion samples (filled by the APTMS solution) into the oven, and in addition sonication guarantee uniform surface coverage, both inside the fibre and on slides.

The second part of the silanisation started with preparing the solution of Eosin Y and (1-ethyl-3-(3-dimethylaminopropyl) carbodiimide hydrochloride (EDAC). EDAC activates the carboxylic group present on Eosin Y. An explanation of the reaction process for Eosin Y and EDAC is presented in Chapter 2 (Fig.2.19 and Fig.2.20). A 10 $mM$ sodium dihydrogen phosphate ($NaH_2PO_4$) was added to water (i.e. a 50 $mL$ solution required 6 $mg$ of $NaH_2PO_4$ for this concentration). The $NaH_2PO_4$ was acidic, hence the pH of the solution decreased. It was required to keep the pH close to 7.2 to support Eosin Y dilution. Next, 0.5 $mM$ of Eosin Y and 25 $mM$ of EDAC was added to the solution. For example, a 50 $mL$ solution required 17 $mg$ of Eosin Y and 240 $mg$ of EDAC. The solution was sonicated for $10 - 15$ $min$ in order to dilute all powders. In addition, a glass beaker with this solution was covered with aluminium foil to avoid

Figure 5.8: *Graph of the reduced silanisation process for six fibres as a function of time (min) with twelve described steps; green line shows the process for 1st fibre, pink line the 2nd fibre, violet line the 3rd fibre, grey line the 4th fibre, red line the 5th fibre, and navy blue line the 6th fibre*

Eosin Y bleaching [131]. Preparing this solution took about 20 *min*. This step is shown as the $7^{th}$ step in Fig.5.6 and also as the $5^{th}$ step in Fig.5.8. Next, fibres and slides were taken out of the oven and left to cool. Then, Eosin Y solution, fibres and slides were all carried to the optical lab. Here, fibres were filled with Eosin Y solution. Fig.5.5d shows the refilled fibre with Eosin Y solution. As a result, a particular magenta colour appears on the fibre surface, which we can observe in Fig.5.5e. Note here, that for this filling, we also waited to observe a cap at the fibre surface. This ensures that the fibre was fully filled. The prepared fibres were immersed in this solution and left for ninety minutes at room temperature, to ensure the reaction between Eosin Y and EDAC with APTMS. Fibres were flushed with water until no magenta colour could be observed on the fibre surface. This usually took around ten minutes. The end-facet of the fibre looked similar to that in Fig.5.5f. As described in [124], the PEGDA hydrogel can be grown on a wet surface. However, it can be a much longer process. Fibres were brought back to the biochemistry lab in order to dry the internal silanised surfaces of the fibre capillaries. The washed fibres were kept overnight in an oven at 35-37° Celsius. The silanisation process was then completed. According to a standard chemical protocol, the silanisation of six fibres required twelve steps and took approximately 425 *min*. However, this process failed to silane multiple fibres. By modifying the protocol to the one just described, the silanisation time was reduced to 385 *min* and all silanised fibres were successfully silanised with an uniform surface coverage. The silanised fibres and slides were stored in dry boxes, covered with aluminium foil to

protect them from contamination and to avoid exposure of Eosin Y to light. It was found that the silanised slides and fibres can be stored for a few months. After such a long time, it was still possible to grow the hydrogel using these fibres (or slides).

### 5.3.2 The hydrogel polymerisation process and distribution of grown hydrogel within HC-PCFs

**Photo-initiation process for HC-PCFs**

The polymerisation process in the fibre begins with filling the silanised fibre with the PVT solution. Next, Eosin Y has to be excited in order to polymerise the PVT solution into the PEGDA hydrogel. The polymerisation process and Eosin Y phosphorescence process are also described in Chapter 2.



Figure 5.9: *(a) Illustration of the fibre cross-section with red circles indicating Eosin Y molecules, (b) the profile of the Gaussian-like profile in the core cross-section*

In order to analyse what may happen inside the fibre and to choose a sufficient method to excite Eosin Y, we present a schematic drawing (Fig.5.9a) of the hydrogel polymerisation. Eosin Y molecules (red circles) are covalently bonded to the silica glass surface of the internal walls of the fibre channels. At this point, we are concerned that the fundamental mode ($LP_{01}$) may be launched into the fibre core. In addition, Fig.5.9b shows this mode profile (green line) and concentration profile of Eosin Y molecules in the core cross-section (pink lines). For this case, the maximum intensity of the optical field may appear at the centre of the fibre. Unfortunately the Eosin Y would be positioned in the weakest part of the optical mode.

When light is launched into the fibre and absorbed by Eosin Y, photons ($\lambda = 545$ *nm*) are emitted. As a result, Eosin Y behaves like a free radical and polymerises the PVT

Figure 5.10: *Illustration of the polymerisation process inside the fibre core with red circles indicating Eosin Y molecules, where (a) shows the hydrogel growing, and (b) is the intensity profile of higher order mode in the core cross-section*

solution into the hydrogel (as explained in Chapter 2). It is important to note that the photo-initiating process probably start from the walls of the fibre core, as shown with the red arrows in Fig.5.10a. Therefore the hydrogel probably grows from the glass wall to the centre of the core. In addition, it was observed and calculated in the literature [123, 125] that the PEGDA hydrogel grows by layers. The first layer of the hydrogel grows next to the glass surface, than another layer forms on top. Following this analysis, the excitation wavelengths of Eosin Y should be launched into the fibre with higher order modes. As we can see in Fig.5.10b, higher order modes such as $LP_{21}$, $LP_{31}$, $LP_{41}$ etc., which may have the intensity peaks close to the glass surface of the core (green lines). For these excitation modes, we may expect the highest intensive excitation of Eosin Y molecules due to improved the integral overlap.



Figure 5.11: *(a) Scheme of the optical setup for the photo-initiation process, and (b) the image of the output of the fibre during the polymerisation process*

Fig.5.11a presents the optical configuration applied for the photo-initiation process. The light source, in this case, had an operation wavelength at $\lambda = 532\ nm$ due to the excitation wavelength of Eosin Y. It was a CW laser (no.1) with power $P = 50\ mW$. Then, the laser beam was collected with a (no.2) lens. In order to launch the maximum possible laser power to the glass surrounding the core (according to Fig.5.10b), we chose the use of a microscope objective (Newport, $M \times 4$, $NA = 0.10$, $FL = 45.5\ mm$)

90

with a spot diameter at focal point of around 30 $\mu m$. The spot diameter is three times greater compared to the diameter of the core (9.8 $\mu m$), and then the light also partially overlapped with the cladding. The silanised fibre filled with the PVT solution (no.3) was then positioned at the *x,y,z* stage using a bare fibre connector (Newport, 561-FH). While, on the other end of the fibre, a CCD camera was placed as shown in Fig.5.11a with (no.4a). Using the CCD camera we could monitor the process of launching the light into the fibre. In the attached black and white near-field image of Fig.5.11b, one can see light in the core area and the microstructure cladding. The bright white circle indicates the light that was trapped into the solid part of the cladding. It was very difficult to generate and observe any kind of optical modes. Instead of observing any optical modes, we could only observe the light presence within the microstructure area as shown within a red dashed circle.

In order to verify the presence of hydrogel in the core, after the photo-initiation process was completed, the fibre was cleaved at both ends until the presence of hydrogel was verified. In this case, we used images of the fibre cross-section tested with the assistance of optical/fluorescence/scanning electron microscopes.



Figure 5.12: *SEM images of the fibre core with a growing hydrogel inside, (a) with a yellow hue, and (b) in black and white*

Examples of the hydrogel grown in the fibre are shown in Fig.5.12. Here, we present two examples of the hydrogel grown from the silica walls. In both these cases, the images of the core of the fibres are SEM images. For Fig.5.12a the hue has changed to yellow, which increased the sharpness of the original image. Fig.5.12b is an original SEM image in black and white. Inside each fibre core, the hydrogel is partly grown within the core (marked with a black arrow). Fig.5.12a shows the example of the hydrogel growth from the circumference to the centre of the fibre. On the other hand, Fig.5.12b presents a different example, where the hydrogel grows only at one side of the core. In both cases, the growing process was initiated from the wall of the fibre. Such behaviour was observed for many more fibre samples. Thus, our analysis

91

described in Fig.5.10 and the hydrogel growth observations are in agreement with the observations presented in [123, 125]. However, in Fig.5.12a and Fig.5.12b we can also observe that the hydrogel was also growing in cladding capillaries. This is attributed to beam size at the focal point of lens (no.2) in the optical configuration from Fig.5.11a. This causes excitation of Eosin Y molecules, not only on the internal surface of the core, but also in the cladding capillaries. Another example, Fig.5.13 demonstrates the cross-section of HC-PCF 1060 taken with an optical microscope for (a) without the hydrogel and (b) with the hydrogel (white spot at the centre of the fibre), respectively.

**Analysing the presence of hydrogel**



(a) *empty*          (b) *hydrogel*

Figure 5.13: *The images of HC-PCF 1060, when (a) there is no hydrogel and (b) hydrogel was grown in the core of fibre*

Due to the non-uniformity observed in Fig.5.12, an analysis of the hydrogel coverage through the length of the fibre was required. Then, we could understand the photo-initiation inside the fibre, and perhaps modify it to ensure an homogeneous coverage. Here, two methods were investigated. The first method involved cleaving the fibre into short segments and observing the hydrogel in the fibre core as this presented in Fig.5.13b. Fig.5.14 presents the hydrogel-filled fibre, which was cleaved in lengths of 1 *cm* to 1.5 *cm*. In order to analyse the hydrogel presence in the core, the brightness measurements for the fibre captures were provided with the assistance of the optical microscope and Nikon software.



Figure 5.14: *The schematic of cleaving the fibre at length:* $1 - 1.5\ cm$

The cross sectional image of each short fibre length was captured and post-processed by software. The mean area brightness of the core area was calculated with the aid of Nikon software. In the presence of the hydrogel, the mean brightness had a high value (i.e. the core area had a white colour). Whilst in its absence, the brightness had a low value (i.e. the core area had a black colour). In order to simplify the analysis, we concerned only if the hydrogel was present in the core or was not. Then, for the observed hydrogel in the core the brightness had just a maximal value '1'. In the case, when we did not observe any hydrogel in the core, we did not assume the value '0'. For this case, we took the mean brightness value measured for the silanised core (i.e. the internal part of the core walls had been covered with APTMS and Eosin Y molecules). It was close to $\approx 0.1$, and it is also shown with a solid green line in Fig.5.15. When the core was not filled with hydrogel and was not silanised, then we measured that the brightness had value 0.00 (black line in Fig.5.14). These values ('1' and '0.1') were plotted as a function of the fibre length (blue lines in Fig.5.15, and shows the hydrogel distribution profile in the fibre core. We could observe that the first 7 *cm* of HC-PCF 1060 were filled with the hydrogel. This fibre point was chosen for other fibre samples as a cleaving point in order to achieve optimum core filling, as previously shown in [46].



Figure 5.15: *Graph of the hydrogel distribution in the fibre, due to the cleaving method*

Following the analyse of a number of fibres (¿20), it was found that the hydrogel was always grown in the first few centimetres of the fibre where the laser beam was launched. It was not dependent on the fibre length. We also could not observe an increase in the hydrogel filling fraction due to increasing the laser power to 100 *mW*. However, the filling of the hydrogel could be doubled by enabling a photo-initiation

process at the other side of the fibre. As a result, the hydrogel may grow in the first and last centimetres of the fibre. For this reason, during the photo-initiation process one of the fibre ends was connected to the syringe filled with the PVT solution (see: Fig.5.11a (no.4b)). The practice of connecting the fibre to the syringe allows keeping the fibre filled with the PVT solution until the polymerisation was initiated. In this case, we could not monitor the fibre end-facet in the CCD camera. The beam was launched into the other fibre end and transmitted through. After 15 *min*, the fibre end was disconnected from the syringe and the fibre was turned around. The photo-initiation process was repeated at the other side of the fibre. As a result, the hydrogel presence was observed at both ends of the fibre. Here, instead of a destructive method, we present another method to estimate the percentage of the fibre filling. The second test provided was *side-view scanning* shown schematically in Fig.5.16.



Figure 5.16: *The schematic of the side view scanning method for the fibre, when each fragment of the fibre is observed with a microscope objective*

When the hydrogel growing process was completed, the fibre was cleaved at both sides. Then, the side of the fibre was scanned with the assistance of an optical or fluorescence microscope. In comparison to the first described method (i.e. cleaving) the fibre was not cleaved into a small segments. Here, the entire fibre length had been tested. The observation of the entire fibre length allowed us to verify the hydrogel distribution profile and the fraction of the filling before any further experiments. This method was found to be more practical than the first method presented. Each small part of the fibre was monitored (i.e. scanned). However, the length of the scanned fibre part depends on the magnification of the microscope lens. Three examples of pictures taken for *the side view scanning* method are presented in Fig.5.17. Once the plastic jacket was removed, we analysed the *bare* fibre. In the example presented, in Fig.5.17, the fibre was scanned in 6 *mm* steps.

To simplify interpretation of results, the fibre edges were marked with two yellow lines. First the silanised fibre was tested. Fig.5.17a presents this fibre side; it is roughly black area within the yellow lines. The Eosin Y was too weak to emit the fluorescence through the solid part of the cladding. Thus, in this example we cannot observe

(a) *Silanised*



(b) $0 - 6$ *mm*



(c) $92 - 102$ *mm*

Figure 5.17: *The images of the side view of the fibre (between the yellow lines), when (a) the fibre was silanised, (b) the hydrogel emits the light from the cladding and the core, (c) the hydrogel is in the core*

anything. Fig.5.17b shows evidence of the hydrogel. It is a white shape in the fibre (indicated with a red arrow). This hydrogel has grown in the cladding capillaries and in the core. In the printed image, as this shown in Fig.5.17c, it is difficult to separate and observe the core and the cladding capillaries. However, at real-time observation these differences were significant. Fig.5.17c represents the hydrogel presence only in the core (thin, white line at the centre of the fibre, indicated with a red arrow). The hydrogel was present in the whole 6 *mm* of the fibre length. However, due to microscope lens aberrations, the left part of the image suggests that only part of the length had the hydrogel. By observing all 6 *mm* fibre sections, we nominated the presence of the hydrogel in the core as '1', and '0' indicates the absence of hydrogel in the fibre core. These values were plotted to illustrate the core filling profile. It is worth noting here that in this analysis we were only interested to estimate the presence of the hydrogel only in the fibre core.

Fig.5.18 illustrates the data points (blue lines) collected for a 11 *cm* long sample. The original fibre length was 14 *cm*. This fibre was cleaved on both sides after the photo-initiation process in order to keep the fibre ends clean and ends flat. Due to this, the hydrogel grown in $1 - 1.5$ *cm* at both fibre ends was lost. As shown in Fig.5.18, it is clear that the hydrogel in the core grew on the first and last 4 *cm* of the fibre. In

Figure 5.18: *Graph of the hydrogel distribution in the fibre core achieved with the side view scanning method*

summary, the hydrogel filling fraction was doubled.

It is worth noting that different periods of polymerisation time were tested. For example, the fibre was exposed to the laser beam for 10 *min*, 15 *min* and 30 *min*. After, 10 *min* not polymerised solution was found inside the fibre (i.e. the fibre was cleaved and there was some liquid inside). After 15 *min* and 30 *min* we did not notice any liquid. However, extending the exposure time to 30 *min* did not increase the hydrogel filling fraction. According to this observation, in further experiments, fibres were held for light exposure for a quarter of an hour (both fibre ends). In order to keep the hydrogel hydrated the fibre was connected to the syringe filled with water and refilled using a low flow rate (5 ml/h). The fibre samples were stored in a plastic container for biological samples filled with distilled water. Any optical tests could be repeated until the hydrogel was dry. However, the fibre end-facet was contaminated after keeping the fibre for a few hours in water. The fibre had to be cleaved, which reduced the fibre length by $2-3$ *cm*. If the fibre becomes very short, testing it becomes technically difficult. As was explained in Chapter 3 the fibre of length $< 10$ *cm* must be placed at one translation stage. This interrupted the collection of transmitted light through the fibre, when the input of the fibre was changing its position. In addition, for a short length of fibre such as $2-3$ *cm*, light leaked in the solid part of the cladding intensely. It was observed that the signal transmitted in the fibre core was less intense compared to that in the cladding.

Note here, that different examples of fibres such as HC-PCF 800 and HC-PCF 1550 with the hydrogel grown inside can be found in Appendix C.

**Photo-initiation process for slides**

The hydrogel polymerisation process on a microscope slide followed the same protocol that is described in Chapter 2. The silanised slide was covered with the PVT solution. In order to photo-initiate Eosin Y attached to the glass surface, we used a CW green laser with wavelength centred at $\lambda = 532$ $nm$ and laser power of 50 $mW$. The laser beam was directed along the side of the microscope slide (75 $mm \times 25$ $mm \times 1$ $mm$). The light beam was scattered over the entire glass. Five minutes of the light exposure was enough to complete the hydrogel polymerisation. The sample was washed with distilled water when the growing of the hydrogel was completed. The non-polymerised PVT solution was removed and the hydrogel matrix was kept hydrated. It was observed that the hydrogel on slides can be stored in water in a fridge for as long a period of time as two years.

## 5.4   Summary

To summarise this chapter, the PEGDA hydrogel was presented and its chemistry and morphology were investigated. Porosity can be controlled and tailored by changing the chemical component proportion in the hydrogel. However, it was shown, that the presence of pores can be verified for a dry state of the hydrogel. It was demonstrated that 12.5% and 25% of the PVT solution can be polymerised into the hydrogel. Both hydrogel contain nano-size pores ($d \approx 7.5$ $\mu m$) and these are suitable for filling the HC-PCF 1060.

Integration of the PEGDA hydrogel within HC-PCF was discussed. Specifically, the silanisation process (chemical surface coverage) of the internal fibre surface was determined. The fibre surface was covered with silane agent APTMS, which was bonded to the internal fibre walls. APTMS bonds with the Eosin Y molecule used for the polymerisation process of the hydrogel. Therefore, the silanisation technique was adapted for HC-PCFs. In addition, we presented the successful silanisation of multiple HC-PCFs. This was possible by reducing the process with the methanol rinsing and implementing the sonication process.

It was demonstrated, that the hydrogel grew inside the fibre due to the light ($\lambda = 532$ $nm$) transmission through the silanised and filled with the PVT solution. This laser beam excited Eosin Y attached to the silica walls, which caused the hydrogel

growth from the fibre core circumference. However, due to the hydrogel distribution analysis, it has been demonstrated that the hydrogel grows irregularly inside the fibre. The developed and tested cleaving fibre technique shows that the optimum fibre length was found at 7 *cm* of the fibre length. However, with additional polymerisation the PVT solution at the other end of the fibre we could observe the hydrogel at both fibre ends. The side-view scanning test confirmed the hydrogel presence in $5 - 6$ *cm* of both sides of the fibre, which increased the hydrogel filling by 50%.

# Optical parameters of the hydrogel

## 6.1 Introduction

Hydrogel integration with an optical device such as HC-PCFs was proposed for the first time (by our group) in 2010 [46]. We described techniques to grow the hydrogel inside the fibre and studied the morphology of hydrogel. Although the PEGDA hydrogel optical properties were not published before, as far as we can see, some attempts in determining the attenuation of hydrogels. The analysis described in article [189] determined the attenuation of the synthetic hydrogel as $\alpha = 0.66 \ cm^{-1}$ using a microscope light source. Measurements of PEG hydrogel parameters were published by [190] and the attenuation equaled $\alpha = 0.1 \ cm^{-1}$ at wavelength $\lambda = 480 \ nm$. However, these analyses were for a PEG hydrogel polymerized as a homogeneous polymer using only poly(ethylene) glycol (chemical components of the PEGDA hydrogel are explained in Chapter 2).

The properties of hydrogel are expected to be similar to that of water due to the hydrated state of the hydrogel matrix. Most of our comparisons are with water. Another advantage of comparing results to these for water is that water had been used for a number of sensor applications with PCFs [17]. For instance, the COM Research Center group proposed the addition of labelled DNA to an aqueous solution, which was inserted into the PCF in order to detect a DNA probe [12]. The Institute for Photonics group in Adelaide analysed fluorescence detection using the microstructured optical fibre filled by quantum-dots in water solution [182]. Also, the HC-PCF was filled with water in order to indicate the mechanism of the PBG shift, which may be applied as the refractive index sensor. This was proposed by the Center of Photonics group in Bath [83]. Another example of filling microstructured fibres with water was used for supercontinuum generation investigated by the Photonics group in São Paulo [156]. Here in this thesis, the fibre was filled with water for the fibre fillings tests, viscometer analysis and a primary test for fluorescence measurements. Thus, water parameters and the light guidance for fibre filled with water are well-known [83, 84, 86, 191].

In this chapter, light guiding properties through the hydrogel filled fibre are characterised: the refractive index and hydrogel attenuation are investigated. In addition,

we analyse an optimum fibre length in order to use the fibre for fluorescence detection. Finally, the light guidance mechanism for the fibre filled with the PEGDA hydrogel is presented.

## 6.2   Optical properties for the filled fibre

In order to investigate the refractive index and the attenuation of hydrogel, at first we characterise fibres filled with water. Then, we compare fibres filled with the hydrogel. Here, we present the transmitted spectra and mode analysis for the fibre filled with the PEGDA hydrogel. For detection of the transmitted spectra of the described fibres, the optical configuration used here is as described in Chapter 3 from Fig.3.15 (for a detection of the fibre's transmitted spectrum). However, we used the Ocean Optics Spectrometer (HR4000) instead of the OSA.

### 6.2.1   Water-filled fibre

According to our observations described in Chapter 5, since the hydrogel mostly grows in the core of the fibre, the light interaction within this sample is limited to the core.



(a) *Collapsed end*          (b) *Water filling*

Figure 6.1: *The water-core fibre, where (a) is preparation for a selective filling, (b) the core filled with water*

Here, we analysed the selective filling of the fibre with water, using the collapsed end. The liquid sample had only access to the core. In the next step, the fibre was filled with water as shown in Fig.6.1b. The filled fibre was placed in the optical setup (Fig.3.15).

Fig.6.2a and Fig.6.2b show the end-facet of the same fibre with neutral density filters: *OD* 2.0 and *OD* 3.0, respectively. Fig.6.2b shows the yellow colour at the fibre core,

(a) *OD* 2.0        (b) *OD* 3.0

Figure 6.2: *Near-field images with supercontinuum propagation in the core with a neutral density filter (c) OD 2.0 and (d) OD 3.0*

however, it indicates the saturation of the CCD camera. When the intensity of light incident on the CCD sensor is reduced with a $0D$ 3.0 filter (Fig.6.2b). We observed only the red colour in the fibre core. The red colour indicates an interval of wavelengths of the visible range for red such as $650\,nm < \lambda < 750\,nm$. We expected the highest power transmitted transmission within this interval; with the remaining of the supercontinuum light to be leaked through the fibre cladding.



Figure 6.3: *The supercontinuum propagation through the fibre selectively filled with water, the intensity of light was reduced with a neutral density filter with $0D$ 2.0*

Fig.6.3 shows the transmission spectrum for this fibre (Fig.6.2a) in a logarithmic scale. It was necessary to reduced light intensity with a neutral density filter *OD* 2.0 in order to not saturate the detector. At a wavelength of $\approx 520\,nm$, there is a relatively strong peak in comparison to the rest of the spectrum probably due to a low water attenuation of water at this wavelength. Another characteristic peak is the highest intensity peak at wavelength $\lambda = 715\,nm$, as expected from Chapter 3. The broadness of the trans-

mitted spectrum in the filled core of the fibre suggests that light propagated with an index-guiding mechanism. Here, at the left part of spectrum we observe that the spectrum begins at 500 *nm*, which may be attributed to a presence of the light in the fibre cladding. As well, the transmitted spectrum decay at right side. It may be associated to continues increment of water attenuation for longer wavelengths in comparison to the visible range. As well, the sensitivity of the used detector had a operating range from 200 *nm* to 1100 *nm* with the highest sensitivity at 600 *nm*.

## 6.2.2   Hydrogel-filled fibre

Here, light guidance properties for the fibre filled with hydrogel are discussed. As the first stage of testing the hydrogel grown in the fibre, the fibre had to be prepared as described in Chapter 5. Afterwards, the presence of hydrogel within the fibre was verified with the assistance of an optical microscope.



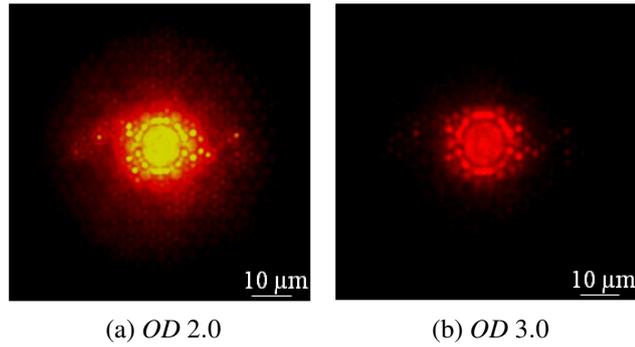|        |        |        |
| :----: | :----: | :----: |
|  (a)   |  (b)   |  (c)   |

Figure 6.4: *Examples of the fibre filled with the hydrogel and (b) near-field images with supercontinuum propagation in the core with a neutral density filter OD 2.0 and (c) OD 3.0*

Fig.6.4a shows the cross-section of a fibre with the hydrogel grown in the core (white dot in the core). However, we can also observe the hydrogel spread randomly in the fibre cladding (white dots). The hydrogel grown in the cladding was noticed previously and was presented in Chapter 5. The tested fibre length was approximately 12 *cm*. Fig.6.4b and Fig.6.4c demonstrate the fibre end-facet images for the transmitted supercontinuum light, which was reduced by two different neutral density filters with *OD* 1.0 and *OD* 2.0, respectively. As was observed for the water example in Fig.6.1d, Fig.6.4c demonstrates the presence of the red colour in the fibre core as well. This can be attributed to propagation in the core wavelength of the interval from 650 *nm* to 750 *nm*.

As was described in Chapter 5, a uniform and homogeneous filling of the hydrogel solely in the core was achieved. The presence of the hydrogel in the cladding was

random and only verified for the first centimetres of the fibre. It was expected to observe a similar transmitted spectrum of the fibre filled with the hydrogel to the fibre selectively filled with water.



Figure 6.5: *Supercontinuum propagation through the core filled with hydrogel (green open circle line) and through water (blue open square line)*

Fig.6.5 shows the transmitted spectrum (green open circle line) for the 13 *cm* long fibre filled with the hydrogel of 13 *cm* in comparison to a 23 *cm* long fibre sample filled with water (blue open square line). The water and hydrogel show almost the same spectral profiles with the hydrogel exhibiting a higher loss. In addition, we observe the broad spectrum guidance equivalent to the observation of light guidance for the water sample. This also suggests that light is propagated with the index-guiding mechanism. Moreover, due to the similarity of transmitted spectra of the hydrogel and water, it can be assumed that the refractive index of the PEGDA hydrogel may be very close to the refractive index of water.

Fig.6.6 also shows another example of the transmitted light for the fibre with the hydrogel grown in the core. Of interest is the 30 *nm* shift at the beginning of the spectrum. The intensity line starts at $\lambda = 470$ *nm* instead of $\lambda = 500$ *nm*. Also the maximum intensity peak is shifted to shorter wavelengths of ($\lambda \approx 670$ *nm*) rather than remaining at wavelengths $\lambda \approx 715$ *nm*. The equivalent shift was observed in Chapter 3 for a mode analysis (calculated) for the core of the fibre with a refractive index changed to 1.34. We can presume that the refractive index of the hydrogel in this case is closer to 1.34. However, the reason why the refractive index of the hydrogel is slightly higher in this example is difficult to explain. In addition, we know that for the 25% concentration of
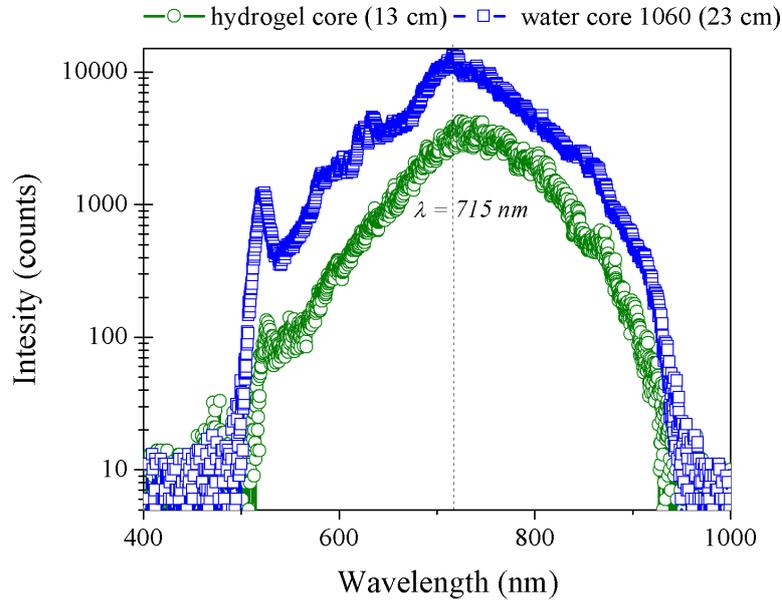
Figure 6.6: *Supercontinuum propagation through the core filled with hydrogel (red open circle line) and water (blue open square line)*

PVT solution, the other 75% is water (described in Chapter 5).

Also, we have observed that the hydrogel contains a lot of water within its structure. According to these two points and the presented transmitted spectra we assumed for any further analysis that the PEGDA hydrogel had a refractive index close to water $n \approx 1.33$. In order to verify particular wavelengths that can also be transmitted through the hydrogel, we tested another fibre sample.

Fig.6.7 presents the image of the fibre cross-section. In this fibre, the hydrogel is grown in the core and randomly in the microstructure cladding. In this case, certain wavelengths from the supercontinuum source were filtered and directed along the fibre. At first the supercontinuum spectrum was launched into the fibre and is shown in Fig.6.7a. Here a bright light in the core can be noticed (i.e. yellow dot) and some light in the hydrogel in the cladding (i.e. red, orange, yellow dots in Fig.6.7a). This suggests that the entire supercontinuum is transmitted through the hydrogel. Fig.6.7b shows the detected transmitted wavelengths: from $\approx 795$ *nm* to $\approx 805$ *nm*. At these wavelengths a fixed IR filter in the CCD greatly reduced the intensity, nevertheless, we can still observe that these wavelengths are confined in the core (light pink dots spread in the image). Next, wavelengths from $\approx 645$ *nm* to $\approx 655$ *nm* were launched into the fibre. Fig.6.7c demonstrates an intense red light within the hydrogel in the core and cladding. Fig.6.7d presents the image of the fibre end-facet, for wavelengths from $\approx 545$ *nm* to $\approx 555$ *nm*. The intensity decreases (i.e. green dots in the fibre are not as bright as in Fig.6.7c). However, it was shown with the following examples that the

(a) *Supercontinuum*                    (b) 800 *nm*

(c) 650 *nm*                    (d) 530 *nm*

Figure 6.7: *The near-field images for the hydrogel-filled fibre, when (a) the entire supercontinuum was propagated, and filtered spectrum using the bandpass filters centred at (b)* 800 *nm, (c)* 650 *nm, and (d)* 530 *nm*

broad spectrum as the supercontinuum is propagated through the hydrogel.



Figure 6.8: *The near field image of HC-PCF with corresponding transmitted spectrum*

The left panel of Fig.6.8 shows the near field image of the fibre: we can observe the hydrogel in the core of the fibre along with random growth of the hydrogel in the microstructure cladding. The hydrogel grows in the cladding only for the first 3 *cm* to 4 *cm* of the fibre input and output due to using a focusing lens with a large spot size for the photo-initiation process. The launched light excites the Eosin Y molecules attached to the cladding holes' surfaces. This causes growth of the hydrogel in the cladding. This effect is also explained in Chapter 5. In the cross-section image of the fibre discussed, light is transmitted in the core of the fibre, but also leaks out to the microstructure region, where localised confinement is also observed within the hydrogel in the cladding (red and yellow dots). The right panel of Fig.6.8 demonstrates the transmitted spectrum for this fibre. The outgoing light is similar to that presented in Fig.6.5 with less intensity. In order to investigate changes of light guidance properties due to the partially filled microstructure cladding, we extended the mode analysis using the numerical modelling described in Chapter 3. A typical pattern shown in Fig.6.9 represents an approximation of the hydrogel distribution with blue shaded regions indicating the higher index areas as 1.33. The order of these areas was dictated to the hydrogel distribution for the fibre sample shown in the left panel of Fig.6.8 as observed using the optical microscope. Simulations were carried out to identify optical modes for wavelengths from $\lambda \geq 520$ *nm* to $\lambda \leq 870$ *nm* in 10 *nm* steps.



| (a) *model* | (b) *superposition* | (c) 520 *nm* | (d) 550 *nm* |

| (e) 670 *nm* | (f) 710 *nm* | (g) 750 *nm* | (h) 850 *nm* |

Figure 6.9: *(a) refractive index mapping for Comsol simulations, with shaded blue fillings (n=1.33) and white empty holes (n=1.00), (b) Matlab superposition of all simulated frames in the range of* 520 *nm* $\leq \lambda \leq$ 870 *nm; light observed at: (c)* 520 *nm, (d)* 550 *nm, (e)* 670 *nm, (f)* 710 *nm, (g)* 750 *nm, (h)* 850 *nm*

All optical modes found were superimposed using Matlab, and the resultant overall modes profile over this wavelength range is shown in Fig.6.9b. This is derived from the following components shown in Fig.6.9c to Fig.6.9h. At shorter wavelength ranges

520 $nm < \lambda < 660$ $nm$ we could observe some cladding modes spread around the core. Examples of observed light in the cladding are presented in Fig.6.9c and Fig.6.9d at wavelengths 520 $nm$ and 550 $nm$, respectively. Fig.6.9e shows the fundamental-like mode, which was observed in the range of 670 $nm < \lambda < 740$ $nm$. Also in this range we found other core modes such as that presented in Fig.6.9f. According to the transmitted spectrum (Fig.6.8), it was expected to observe light in the fibre core. For the longer wavelengths (750 $nm < \lambda < 870$ $nm$) confinement within the core was not observed, as shown in Fig.6.9h.

Note here that for all of the fibre end-facet images (Fig.6.1c, Fig.6.1d, and Fig.6.7a - Fig.6.7d), it was possible to confine the light within the fibre core.

## 6.3 Hydrogel attenuation

This section describes an investigation of the attenuation of the hydrogel. We assumed that hydrogel attenuation is a combination of absorption and scattering effects. In order to determine the hydrogel attenuation, we measured the transmitted power through the fibre filled with the hydrogel.The optical configuration for these tests was the same as presented in Chapter 3.

| no. | $L$ | light source | $\lambda$ $(nm)$ | $P_0$ | $P$ | $\alpha$ $(cm^{-1})$ | $(\overline{\alpha} - \alpha)^2$ |
|-----|-----|--------------|-------------|-------|-----|---------------------|----------------------|
| 1 | 10 $cm$ | CW laser | 532 | 48 $mW$ | 0.23 $mW$ | 0.53 | |
| 2 | 10 $cm$ | SC* | 650 $nm$ | 1.8 $mW$ | 4.5 $\mu W$ | 0.60 | 0.021 |
| 3 | 10 $cm$ | SC* | 650 $nm$ | 1.9 $mW$ | 4.5 $\mu W$ | 0.60 | 0.019 |
| 4 | 9.6 $cm$ | SC | 650 $nm$ | 0.058 $\mu W$ | 3.16 $nW$ | 0.41 | 0.003 |
| 5 | 6.9 $cm$ | SC | 650 $nm$ | 0.058 $\mu W$ | 1.99 $nW$ | 0.63 | 0.030 |
| 6 | 8.0 $cm$ | SC | 650 $nm$ | 0.058 $\mu W$ | 3.16 $nW$ | 0.49 | 0.0001 |
| 7 | 6.1 $cm$ | SC | 650 $nm$ | 1.99 $\mu W$ | 0.63 $\mu W$ | 0.19 | 0.074 |
| 8 | 13.0 $cm$ | SC | 650 $nm$ | 0.16$\mu W$ | 3.16 $nW$ | 0.30 | 0.025 |
| | | | | | | $\overline{\alpha} = 0.46$ | $\Delta\alpha = 0.16$ |

Table 6.1: *Data of light attenuation for the fibre with hydrogel grown inside, SC\* indicates that the supercontinuum signal, which was filtered with a bandpass filter centred at the described wavelength*

For eight different fibres filled with the 25% concentration of PEGDA hydrogel, the measurements of input and output power were made using two detection setups. First three of presented results in Table 6.1 were detected using a power meter (Newport 1935-C). This power meter covers the range of detection from $\lambda = 200$ $nm$ to $\lambda = 1800$ $nm$, with sensitivity from $pW$ up to $W$. At first the power meter was positioned in a focal plane of the lens, which launched a particular wavelength of the supercontin-

uum / CW laser beam into the fibre sample (as shown as (no.4) in Fig.3.15 in Chapter 2). Without the fibre in the set-up we measured the input power. Next, the fibre was mounted to the setup and light was transmitted through the fibre. The power meter measured the output power at the end of the fibre. However, for the last five results in Table 6.1 (from 4 to 8) the power was detected using the OSA. At first, we detected the supercontinuum profile out of the focusing lens using the collecting lens and the multimode fibre. Then, the HC-PCFs samples were put into the optical configuration and again the spectra were collected. The ratio of the input and output powers form each spectrum was calculated, and the result at 650 $nm$ is shown in Table 6.1. The hydrogel attenuation was calculated using Equation 2.8 as described in Chapter 2, which gives:

$$P = P_0 \cdot e^{-L \cdot \alpha} \text{ then } \alpha = \frac{\ln(\frac{P_0}{P})}{L} \tag{6.1}$$

$$\Delta\alpha = \sqrt{\frac{1}{n}\sum_n^1 (\overline{\alpha} - \alpha_n)^2} \tag{6.2}$$

The collected data are presented in Table 6.1. Seven measured values were taken into calculations, as this shown in Table 6.1 from 2 to 8. The average attenuation ($\alpha$) for the 25% hydrogel equal $\alpha = 0.46$ (for wavelengths close to $\lambda \approx 650$ $nm$). The root mean square (RMS) formula (Equation 6.2) was used to calculate the error margin between seven $\alpha$ numbers. It equals $\Delta\alpha \pm 0.16$.

The calculations of the attenuation here used the full power measured, and hence coupling losses and efficiency in core confinement is not taken into account. Therefore it possibly over-estimates the attenuation of the hydrogel in the fibre. Then, we can say, that this number presents the worst case scenario for the hydrogel attenuation analysis. However, it is comparable to the results published in [189] for the synthetic gel with $\alpha = 0.66$ $cm^{-1}$.

According to Equation 2.8 and discussion of the hydrogel attenuation, we may estimate a signal transmittance as a function of the fibre length for $L > 0$. Fig.6.10 shows a decay of the transmittance for the fibre filled by the hydrogel ($\alpha_m = 0.46$ $cm^{-1}$) (red line) at $\lambda = 650$ $nm$. We can observe at the $9^{th}$ centimetre of the fibre, the signal decayed by 90%.

Fig.6.11 shows the decay for the fibre filled with water ($\alpha_m = 0.022$ $cm^{-1}$) (blue line). The water attenuation coefficient was taken from reference [86] and at $\lambda = 750$ $nm$. In this example, the transmittance decay to 75% at 66 $cm$ of the fibre length. In both discussed cases, the input signal ($I_0$) equals one. Also, it was assumed that the fibre sample was always kept straight (i.e. no additional light attenuation due to bending) [165, 192].

Figure 6.10: *The fibre length against the transmitted light for the fibre filled with the 25% PEGDA hydrogel (red line)*



Figure 6.11: *The fibre length against the transmitted light for the fibre filled with water (blue line)*

## 6.4 Determination of the fibre optimum length

In order to estimate the fibre length for the fluorescence detection, we first discuss what may happen inside the filled fibre with fluorochromes, as shown in Fig.6.12. According to Fig.6.12, it is assumed, that the input intensity (orange arrows at the bottom of Fig.6.12) decays exponentially for each fibre section. It depends on the

Figure 6.12: *Schematic of fluorescence transmitted intensity for HC-PCF filled with an absorbing material with fluorochrome molecules*

material attenuation at the excitation wavelength, which was presented in Fig.6.10 and Fig.6.11 using Equation 2.8. If fluorescence is also measured within the hydrogel structure, it must be taken into account that a fluorochrome molecule also absorbs light. For this reason, light attenuation increases [131, 193]. We assumed that the probability of excited fluorochromes (red dots) decays also exponentially. Thus, the fluorescence signal is proportional to the number of excited molecules in each section (red arrows at the top of Fig.6.12), which depends on the attenuation coefficient of the material at the emitted wavelength. The concentration of these molecules must be concerned. As Equation 2.8 only shows the impact of material attenuation through the length, we include here the attenuation of the fluorochrome molecules, which gives [193]:

$$I = I_0 \cdot e^{-L \cdot (\alpha_m + \alpha_{fluoro})} \tag{6.3}$$

where, the $\alpha_{fluoro}$ can be estimated using the molar extinction coefficient ($\alpha_{fluoro}$) of particular fluorochrome molecule as this described in Chapter 2 with Equation 2.13.

Using Equation 6.3, we can observe in Fig.6.13, the hydrogel was mixed with 1 $\mu M$ concentration of Cy-5 fluorochrome (red line) and 6 $\mu M$ (green line). The fibre length is reduced ($\approx 7$ $cm$) in comparison to the analysed fibre length in Fig.6.10. It is even more reduced for a higher concentration (6 $\mu M$) case. Here, the transmitted signal approached the minimal intensity at $\approx 4$ $cm$.

Figure 6.13: *Graph of the output intensity for the hydrogel sample with two concentrations of Cy-5 fluorochrome:* 1 *μM (green line) and 6 μM (red line)*



Figure 6.14: *Graph of the output intensity for the fibre filled with water solution of Alexa-750 fluorochrome with two concentrations of* 1 *μM (dark-yellow line) and 6 μM (blue line)*

As we can observe in Fig.6.14, the output intensity for the fibre filled with an aqueous solution and Alexa-750 is also affected. Here, we analysed the same concentrations of Alexa-750 as for Cy-5 molecules: dark-yellow line presents 1 *μM* and blue line 6 *μM*, respectively. The transmitted signal is minimal about $\approx 35$ *cm* for 1 *μM* concentration and $\approx 7$ *cm* for 6 *μM*.

111

The hydrogel and 1 μM of Cy-5 molecules:
back-fluorescence — trans-fluorescence

(a) *hydrogel*

The hydrogel and 6 μM of Cy-5 molecules:
back-fluorescence — trans-fluorescence

(b) *hydrogel*

Figure 6.15: *Intensity as a function of the fibre length with Back-F signal and Trans-F for (a) and (b) for the hydrogel with 1 μM (magenta and blue lines) and 6 μM (grey and orange lines) of Cy-5 concentrations, respectively*

However, even the fluorochromes absorbs light and causes the higher signal loss at the same time they emit photons. Then, we can say that we are looking for a optimum fibre length. It is the length for which the sample analysis is most effective, allowing interaction with samples while minimising attenuation effects [12, 17]. For our case, the material and fluorochrome attenuation supposed to be balanced by the emitted fluorescence signal. Herein, we also considered that the emitted wavelength is also

absorbed in the medium ($\alpha_{emit}$) [193]. However, in order to collect the fluorescence signal as a function of the fibre length two scenarios must be investigated. The first one is for detecting the transmitted fluorescence signal ($I_{trans-f}$). In this case, the fluorescence signal is collected as a transmission (at the fibre output). It is the total of the attenuated signal for each of the fibre section reduced by the emitted light. Also, we may expect that the output signal decreases at each length unit, similar to the presented transmittance graphs. In order to estimate the optimum fibre length we used following equations:

$$I_{trans-f} = I_0 \cdot \left( \left( e^{-(\alpha_m + \alpha_{fluoro} + \alpha_{emit}) \cdot L} \right) \cdot \left( -1 + e^{\frac{\alpha_{emit}}{2} \cdot L} \right) \right) \tag{6.4}$$

The second scenario is for collecting the fluorescence signal at the fibre input. It is called a back-fluorescence ($I_{back-f}$). First of all, we detect the fluorescence for which the excitation signal was maximal. In addition the fluorescence signal of the whole fibre length ($L_{total}$) is added [194]. For this case, we may expect to use the longer fibre and its length is estimated using following equation:

$$I_{back-f} = I_0 \cdot \frac{\alpha_{emit}}{2 \cdot (\alpha_m + \alpha_{fluoro})} \cdot \left( e^{-(\alpha_m + \alpha_{fluoro}) \cdot L} - e^{(\alpha_m + \alpha_{fluoro})(-2 \cdot L_{total} + L)} \right) \tag{6.5}$$

Fig.6.15 presents two investigated scenarios of fluorescence detection as a function of the fibre length, according to Equations 6.4 and 6.5. Fig.6.15a shows the results obtained for the fibre filled with the hydrogel with 1 $\mu M$ of Cy-5 fluorochrome. As we can see, the optimum fibre length for the $I_{trans-f}$ is only 2 $cm$. However, analysing the line for the back fluorescence ($I_{back-f}$) can also observe that this line is constantly increasing towards an asymptotic value. In this case, rather than assuming an infinite length, we calculated the length at which 99% of the asymptotic value had been achieved. As we can see in Fig.6.15a with magenta line, for 1 $\mu M$ of fluorochrome molecules concentrations, the used fibre length should be longer than 12 $cm$. Fig.6.15b presents the results for a Cy-5 concentration increased to 6 $\mu M$. The optimum fibre length dropped to 1 $cm$ for the transmitted fluorescence $I_{trans-f}$. For the back-fluorescence signal, the asymptotic value was found close to $> 7$ $cm$.

For comparison we plotted results for the fibre filled with water and Alexa-750 fluorochrome with the same concentrations as for Cy-5. Fig.6.16a describes the optimum fibre length obtained for 1 $\mu M$ for $I_{trans-f}$ as 8 $cm$. Considering, $I_{back-f}$, the asymptotic value was calculated close to $> 49$ $cm$. In Fig.6.16b we can observe the same tendency as that observed for the hydrogel sample. For an increased fluorochrome concentration, the optimum fibre length is reduced to 2 $cm$ for $I_{trans-f}$ (red line), and for the $I_{back-f}$ case, the asymptotic value was at length $> 13$ $cm$ (green line).

The water and 1 μM of Alexa-750 molecules:



(a) *water*
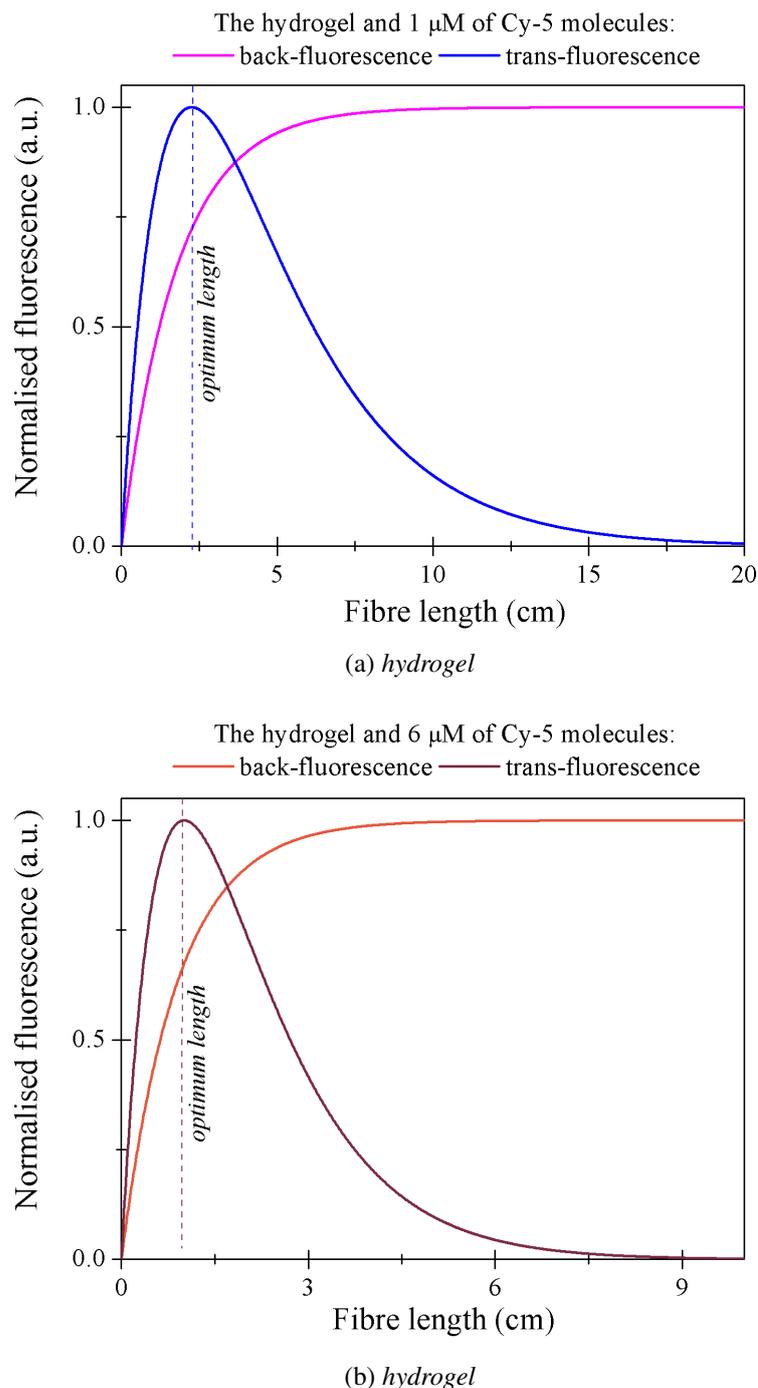
The water and 6 μM of Alexa-750 molecules:



(b) *water*

Figure 6.16: *Intensity as a function of the fibre length with Back-F signal and Trans-F for (a) and (b) for water sample with 1 μM (green and red lines) and 6 μM (purple and light-cyan) of Alexa-750 concentration*

Note here, that we assumed the number of excited molecules equals the number of emitted molecules, with a fluorescence efficiency was estimated as 100%.

## 6.5 Summary

We analysed the transmitted spectra for a number of fibres with the hydrogel filling. These spectral profiles were found to be close to these observed for water. According to this, we estimated that the refractive index of the PEGDA hydrogel is close to the value 1.33. However, it was demonstrated that sometimes hydrogel may have a slightly higher refractive index than water, which causes a blue shifting. Also, it was demonstrated through experiments and modelling that the presence of hydrogel in the microstructure cladding channels does not hinder the spectral analysis.

During the analysis of the hydrogel attenuation, it was approximated that the hydrogel attenuation is close to $0.46 \pm 0.16$ $cm^{-1}$, for wavelengths close to $\lambda \approx 650$ $nm$. Due to this relatively high attenuation coefficient, the maximum practical fibre length for modal analysis was (10 $cm$). It was found, that due to low water attenuation coefficient, testing a 60 $cm$ of the filled fibre core was still possible. However, it was observed that with a higher concentration of fluorochrome, the pump decay changes. We demonstrated two scenarios for detecting fluorescence such as transmitted fluorescence and back fluorescence. It was calculated that it should be more sufficient to detect the back-fluorescence signal. Considering the fibre filled with the hydrogel and Cy-5 fluorochrome, the fibre length should be longer than $> 12$ $cm$ for 1 $\mu M$ and $> 7$ $cm$ for 6 $\mu M$. Regarding, water and Alexa-750 fluorochrome the fibre length can be as long as 50 $cm$ for 1 $\mu M$ and $> 13$ $cm$ for 6 $\mu M$.

# DNA probe detection in the hydrogel

## 7.1 Introduction

In this chapter, a labelled DNA probe immobilisation in the hydrogel within HC-PCFs is demonstrated. This includes development of the technique to grow the hydrogel within the PCF fibre with an immobilised DNA probe.

Here, we present a detection of immobilised DNA for a various DNA molecule concentrations and fibre lengths. The successful immobilisation and detection of DNA within the hydrogel structure contained in HC-PCFs is a proof-of-concept of this thesis, and can qualify the use of HC-PCFs integrated with the hydrogel as sensor for the selection process of DNA in point-of-care methods.

Additionally, the supercontinuum light source is tested in terms of fluorescence detection for HC-PCFs, when filled with fluorochrome diluted in an aqueous solution for one of the lowest concentrations compared to those recently published.

## 7.2 DNA immobilisation within hydrogel in HC-PCFs

### 7.2.1 DNA probe in a PEGDA solution

The immobilisation of a labelled DNA probe inside the PEGDA hydrogel started with the preparation of the PVT solution with DNA molecules before the polymerisation process, as explained in Chapter 2 and 5. In order to prepare the required final concentration of Cy-5 DNA in the hydrogel, 100 $\mu M$ of the Cy-5 DNA probe is proportionally added to the PVT. For example, to prepare the 0.6 $\mu M$ solution of the Cy-5 DNA, 9 $\mu L$ of 100 $\mu M$ DNA is poured into a container, and PVT solution is added to get a 1.5 $mL$ final volume. Details of this DNA molecule and its sequence can be found in Chapter 2. There the specifications of Cy-5 fluorochrome are also described. As explained in Chapter 2, it is required to stabilise the bonding of the DNA molecule with the polymer using an NHS-PEG-acrylate cross-linker. It is sufficient to add 18 $mg$

of cross-linker powder to 1.5 *mL* of PVT with the Cy-5 DNA. The schematic of the molecules described and their connections are presented in Fig.2.28 in Chapter 2. The solution was mixed using a chemical shaker for less than one minute. The plastic container was then covered with aluminium foil to avoid any light exposure of the sample.

### 7.2.2   DNA immobilisation in hydrogel grown on a slide

As a pre-step to the fibre tests with the DNA probe immobilisation, we examined the hydrogel with and without the immobilised DNA molecules.  For this case, the hydrogel grown on microscope slides. At first, the slide was silanised and the PVT was polymerised on its surface. The chemical protocol and details of these procedures are described in Chapter 5.  Next, the grown hydrogel was removed using a scalpel blade from the original slide and positioned onto clean glass. Examining the specimen using a fresh slide ensured that only the hydrogel structure was observed, with no surface coverage from the silanisation process. The hydrogel structure was then examined by fluorescence imaging with the assistance of an epi-fluorescence microscope (Olympus IX81).



Figure 7.1: *Schematic of the cube filter used in the epi-fluorescence microscope*

In the optical path of this type of microscope were a set of filters specifically designed to optimize detection of fluorescence of three fluorochromes: *fluorescein isothiocyanate (FITC)*, *green cyanine (Cy-3)* and *red cyanine (Cy-5)*. Fig.7.1 shows these filters, which were combined to produce one cube of three categories of filters: exciter filters (violet shape), barrier filters (pink shape) and dichromatic beam splitters (i.e. dichroic mirrors) (pink-violet shape). The exciter filter was positioned in front of the light source. It was one side of the cube and was vertically oriented to the optical

path. This filter selected an excitation wavelength from the light source. The splitter was placed at 45° to the optical path inside the cube, and hence the excitation wavelength was reflected from the dichroic mirror into the specimen (i.e. sample). The reflected fluorescence light from the specimen was transmitted through the dichroic filter. At the horizontal side of the cube was the barrier filter. This filter selected only the fluorescence light from the background reflections and passed it to the objective. Fig.7.2 shows a series of images of 25% concentrations of the PEGDA hydrogel using this kind of microscope and a set of the above-described filters. It is worth mentioning here, that we expected to observe a luminescence due to the presence of Eosin Y inside the hydrogel. The Eosin Y molecule was previously characterised as a photo-sensitive molecule, and its phosphorescence at wavelength $\lambda \approx 525 - 570$ $nm$ was presented in Chapter 2. Also in Chapter 2 we can find the excitation and emission profile of Eosin Y with a description of the phosphorescence process.



| (a) *white light* | (b) 520 *nm* | (c) 570 *nm* | (d) 670 *nm* | (e) 670 *nm* |

Figure 7.2: *The images of PEGDA hydrogel grown on the slide, illustrated with assistance from the epi-fluorescence microscope, with details of the filter used and the integration time of the CCD camera used for the observation: (a) 5 ms, (b) 20 ms, (c) 100 ms, (d) 10 s, (e)100 ms for 1 μM of Cy-5 DNA probe*

Fig.7.2a shows the hydrogel structure (dark spot) illuminated by white light (i.e. microscope lamp, without any filters). Fig.7.2b shows the hydrogel structure (green spot) observed using an FITC filter. This filter transmitted the excitation wavelength at 490 *nm*, and allowed the observation of the fluorescence signal at 520 *nm*. In this case, we could observed the fluorescence light due to Eosin Y phosphorescence. It was found that the hydrogel sample for the FITC filter was always very bright, even for such a short exposure time (20 *ms*). The other filter used here was Cy-3. This filter was designed to filter the excitation wavelength at $\lambda = 550$ *nm* and select fluorescence light at $\lambda = 570$ *nm*. Fig.7.2c shows the hydrogel (orange spot), for which the fluorescence of Eosin Y was observed. In order to verify the Cy-5 DNA probe in the hydrogel, the filter was changed to Cy-5. In this case, the filter allowed for the excitation transmission at $\lambda = 650$ *nm* and the fluorescence at $\lambda = 670$ *nm*. Fig.7.2d presents a black surface. Clearly no hydrogel is observed and no contamination with Cy-5 labelled DNA occurred as no fluorescence is observed either. When the 1 *μM* of DNA probe was immobilised inside the hydrogel, the hydrogel reflected the fluorescence of Cy-5

fluorochrome. Fig.7.2e presents the red spot, with at higher magnification, indicating the presence of Cy-5 DNA-probe inside the hydrogel sample. These measurements were realised using the fluorescence microscope without the detector, which could detect the intensity of the fluorescence light. For this reason, there was no information about the intensity. Only the presence of fluorochrome could be verified. Nevertheless, we show here that the solution of PVT with Cy-5 DNA was polymerised into the PEGDA hydrogel, and the DNA probe immobilisation was verified inside the hydrogel structure. In addition, the response of the hydrogel to illumination at a certain wavelength was observed due to Eosin Y molecules inside the hydrogel structure. For this reason, for further experiments we called this illumination *hydrogel auto-fluorescence*.

### 7.2.3 DNA immobilisation in hydrogel grown in the fibre



(a) *White light*

(b) 570 *nm*

(c) 670 *nm*

(d) 670 *nm*

Figure 7.3: *The images of the fibre cross-section, with hydrogel grown in the core, for (a) the optical microscope, and (b,c,d) fluorescence microscope with the integration times: (b) 2 ms, (c) 10 s (the hydrogel without the Cy-5 DNA probe), and (d) 1 s (the hydrogel with the Cy-5 DNA probe) [195]*

In this section, we present the DNA immobilisation in the hydrogel for HC-PCFs. The same fluorescence imaging was performed for the fibres with hydrogel grown inside as that presented for slides in Fig.7.2. Fig.7.3 presents the cross-section of HC-PCF 1060 with the hydrogel grown within the core. One of the fibre ends was observed

using the optical microscope (Nikon Eclipse ME600) and epi-fluorescence microscope (Olympus IX81) as described above. The fibre was held in the microscope using a fibre clamp attached to a microscope bench, and then illuminated.

Similar to experiments with the microscope slides, Fig.7.3a first shows the fibre cross-section illuminated with white light. The white dot at the centre of the fibre cross-section confirms the presence of the hydrogel. In the next example as shown in Fig.7.3b, the fibre was tested using the fluorescence microscope. In Fig.7.3b, we observe the red colour in the microstructure cladding and the red dot in the core of the fibre. This is the observed fluorescence at $\lambda = 570$ *nm* due to Eosin Y light emission (i.e. for the Cy-3 filter) similar to Fig.7.2c. Next, the Cy-3 filter was replaced by the Cy-5 filter. Fig.7.3c presents a black screen as was expected (see: Fig.7.2d). In the last test, the fibre was filled with the solution of PVT and the Cy-5 DNA probe, which gave 400 *nM* of the DNA in the final solution product. The solution was then polymerised thus immobilising the Cy-5 DNA in the hydrogel that was grown in the fibre core. Fig.7.3d shows the black screen with a red dot at the centre of the image. It indicates the fluorescence of the Cy-5 DNA probe positioned inside the fibre core. Following this analysis, the immobilisation of DNA inside the fibre filled with the hydrogel was successfully verified [195].

## 7.3 Fluorescence measurements for HC-PCFs

### 7.3.1 Experimental set-up

The detailed experimental set-up used to determine the fluorescence intensity signal from samples in the HC-PCF is depicted in Fig.7.4. The light source used was the supercontinuum source (no.1), explained in Chapter 3.

This set-up is similar to the one used for the transmitted spectra detection shown in Chapter 3. Each element of the set-up was positioned on optical carriers (Newport, PRL-3 and PRC-1) and held on the two optical rails to maintain a precise alignment throughout the experiments. The optical lenses were attached to the same translation stages and lens holders as in Chapter 3. However, in order to obtain the optimum excitation of the fluorochrome and detect the resulting back-fluorescence, two selective filters were placed before (no.2) and after the sample (no.11) with the additional presence of a dichroic filter (no.3) in the middle. For fluorescence measurements only certain wavelengths were required. The set of *input* filters (no.2) ensured that the supercontinuum light was properly filtered to excite the fluorochrome only. In front of

Figure 7.4: *The scheme of the optical setup where: HNL-PCF=highly nonlinear PCF, IF =input filters, DF=dichroic filter, AF=alignment filter, OF= output filters, PMT = Photomultiplier tube, MM=multimode fibre. The HC-PCF output was connected a CCD for monitoring purposes*

| Filters | Cy-5 fluorochrome |
|---------|-------------------|
| Input | band pass at 650 *nm*, 10 *nm* bandwidth—low pass, at 650 *nm* |
| Output | band pass at 670 *nm*, 10 *nm* bandwidth—high pass, at 665 *nm* |
| Dichroic | transmission at 650 *nm*, reflection at 670 *nm* |
| Alignment | band pass at 530 *nm* 10 *nm* bandwidth |

Table 7.1: *Optical filters used for Cy-5 fluorochrome*

the detector we placed two *output* filters (no.11) to avoid detection of reflection of the exciting signal. These filters also select fluorescence light from the specimen. The entire set of filters were replaced for detecting two different types of fluorochrome. Their specifications are in Table 7.1 and Table 7.2 for Cy-5 and Alexa-750 fluorochrome, respectively.

In this set-up the supercontinuum light had been filtered with the dichroic filter (no.3). This filter transmitted the excitation wavelength along the *x-axis* but deflected the backward propagating fluorescence light with a 90° degree clock-wise rotation. It was affixed to the rotation stage enabling the positioning of the filter at 45° degree to the horizontal optical axis (i.e. *x-axis*). An *alignment filter* (no.4) was positioned in front of the focusing lens (no.5) to block the excitation wavelengths. This filter had a dif-

| Filters | Alexa-750 |
|---------|-----------|
| Input | band pass at 740 *nm*, 10 *nm* bandwidth—low pass, at 750 *nm* |
| Output | band pass at 780 *nm*, 10 *nm* bandwidth—high pass, at 775 *nm* |
| Dichroic | transmission at 750 *nm*, reflection at 780 *nm* |
| Alignment | band pass at 530 *nm*, 10 *nm* bandwidth |

Table 7.2: *Optical filters used for Alexa-750 fluorochrome*

ferent transmission wavelength compared to the fluorochrome excitations wavelengths used (as described in Tables 7.1 and Table 7.2). It allows aligning the fibre in the setup without the fluorochrome excitation. Next, the filtered beam passed through to an infinity corrected objective (no.5) to focus the beam into the fibre and to collect the back-fluorescence light from the fibre. This light is divergent in nature, but is transformed to collimated light when it passes through this lens. The fibre (no.6) already filled with the sample was placed in the set-up using the *x,y,z* stages at both ends of the fibre, with a working distance $WD = 0.5$ *mm* to the focusing lens. The beam was focused into the fibre core and transmitted through the fibre. Then, the transmitted light was collected with the infinity corrected lens (no.7). Here, we used the CCD (no.8) to continuously monitor the fibre alignment. At this stage, the alignment filter was removed from the beam line. The *input filters* (no.2) were now positioned into the beam line with their respective flip-up holders. The supercontinuum light was filtered with a low pass filter, bandwidth filter and the dichroic filter (see Table 7.1 and Table 7.2). The beam was focused into the fibre and transmitted through. The light excited the fluorochrome in the sample inserted into the fibre channels. In general, fluorescence does not have a preferred direction. In this experiment, due to the fibre geometry, the fluorescence light is confined to the core instead of scattering. It is assumed that the fluorescence propagates in both directions and is commonly referred to as *back-fluorescence* and *trans-fluorescence*. According to the discussion in Chapter 6, we configured the optical setup to collect the back-fluorescence signal from the fibres. Here, this signal was collected with the lens (no.5). Then, the fluorescence (parallel beam) was deflected 90° clockwise at the dichroic filter. A rotatable mirror (no.10) positioned in the beam line further deflected the light with a 90° clockwise shift. The light was forwarded to the bottom arm of the optical set-up. The *output filters* (no.11) further resolved the fluorescence beam as described in the filter specifications. Then, the objective microscope (no.12) lens (Newport, $\times 10$, $NA = 0.25$, $FL = 16.5$ *mm*) coupled the beam into a multimode fibre (no.13) (Thorlabs BFL 22-200, $NA$ 0.22, $d_{core} = 200$ $\mu m$, Vis-IR) with a 1 *m* of length. The input of the fibre was placed at 5.5 *mm* working distance from the (no.12) lens. The other end of the fibre was connected to a photomultiplier tube (no.13) using an FC fibre adapter attached to a PMT. PMTs are powerful tools for detecting low level signals. Usually they are used in combination with a low noise amplifier, a discriminator and a pulse counter. However, the PMT (Hamatsu H9656-20) used in the experiments had a built-in low noise amplifier. A Labview programme was developed by a colleague, Jiadi Lu, in order to implement the discriminator and count the pulses in 0.1 *s* intervals above a certain threshold using a 16 *bit* 400 *ks/s*1 analogue to digital converter (DAQ). The DAQ was connected by a USB cable to a PC. Dark counts were also performed for reference, where the laser beam was switched off and the pulses counted. The total number of peaks as a function of time was then

recorded. The background of the fluorescence process is explained in Chapter 2.

## 7.3.2   Fluorescence detection with HC-PCFs

A proof of the concept of this thesis was to devise a technique to analyse the DNA probe within the hydrogel, which was placed within HC-PCFs. However, we were also interested to implement the fluorescence detection using the supercontinuum source (with generated 0.55 *ns* pulses with the pulse frequency 0.15 *ms*) instead of a traditional CW source. Using the supercontinuum spectrum allows the flexibility of fluorochromes choice, due to multiple number of excitation wavelengths in the spectrum. As well, the optical configuration developed for the fibre transmission detection may be used for the fluorescence detection only with adding the optical filters. In terms of the developing a new sensor it could broad number of applications of such sensor. In order to use the supercontinuum source, we first analysed the optical set-up shown in Fig.7.4 with the fluorescence of Alexa-750 fluorochrome in aqueous solution. This fluorochrome had been earlier successfully verified by Jiadi Lu, using a CW source. The Alexa fluorochromes are known as more efficient molecules in comparison to dyes [132]. We also chose this fluorochrome due to the fact, that the supercontinuum at $700 - 760$ *nm* (Alexa-750 excitation wavelengths) has much higher intensity in comparison to another wavelengths of the transmitted spectra for the fibre selectively filled with water (see Fig.6.3 in Chapter 6). Also, we diluted this fluorochrome in water, due to lower attenuation coefficient for water compared to that of the hydrogel.

**Preparation of the fibre sample**

At the first stage of testing the optical set-up with the fibres samples, a number of HC-PCFs 1060 were prepared for selective filling using the fusion splicing method (as described in Chapter 4). According to the analysis of Chapter 6, a 50 *cm* length would provide 99% of the asymptotic value for collecting the back-fluorescence signal for 1 $\mu M$ of fluorochrome concentration. However, for this optical configuration test a fibre length of 30 *cm* was used in order to keep the fibre straight and avoid bends or any additional losses. It was calculated that a reducing the fibre length of 20 *cm* should only affect the efficiency of collecting the back-fluorescence signal by 3%.

The Alexa-750 had been originally a powder. The preparation of this fluorochrome to a certain concentrations in aqueous solution was provided by Jiadi Lu. The filling process was run using the syringe set-up. One end of the fibre was connected o an

optical microscope. In front of the microscope lamp was mounted a bandpass filter centred at transmission wavelength $\lambda = 520\ nm$. This ensured that the fluorochrome in the fibre would not be excited during the filling process. The filled fibre sample was transported to the optical set-up. It should be mentioned here that the collapsed ends of the fibre were not cleaved.

**Experimental measurements**

It is well-known that the optical set-up alignment for the fluorescence measurements is crucial. In terms of working with free-space optics, any beam deviations hinders the signal detection. For this reason, before any fluorescence measurements for the fibres were taken the optical set-up shown in Fig.7.4 was tested in terms of alignment and detection abilities with a high concentration ($100\ \mu M$) of Alexa-750 fluorochrome diluted in distilled water. A plastic slide (Ibidi, 80601) was filled with the sample of approximated $15\ \mu L$ volume and mounted to a linear translation stage (Standa, 7T175-100) supported at both sides with steel blocks. This element was placed in front of the lens (no.5). When we observed fluorescence, then the optical configuration was qualified for any further tests using the fibre samples.



Figure 7.5: *Fluorescence curves as a function of concentration for Alexa-750 in a fibre filled with water: purple circles indicate* 100 *nM, green triangles display* 200 *nM, blue squares are for* 500 *nM, and black diamonds are noise level*

Fig.7.5 shows a typical fluorescence measurements over time. A decay is observed over a period of 55 *s* indicating that photo-bleaching occurred [131]. This process is probably nonlinear, and hence the decay time may be intensity dependent. We show

three curves for the three fibre samples filled with solutions of Alexa-750 fluorochrome in water with three different concentrations of fluorochrome: 100 *nM* (purple circle line), 200 *nM* (green triangle line), and 500 *nM* (blue square line). The average dark count rate was 2.25 counts over 76 *s* time. As we can see, for the highest measured concentration, saturation of the detector is observed. The peak of fluorescence cannot be determined. In this case, neutral density filters should be used just before the detector. However, we were interested in approximating the detection for much lower concentrations than 500 *nM*. As we can observe in Fig.7.5, the 200 *nM* concentration line has a highest peak close to 600 counts. This was lower than the limit of our detector (i.e. 700 counts). The next line (purple circles) presents the decay for a 100 *nM* concentration. It was also observed here, that the line of 100 *nM* concentration had a longer decay time in comparison to the green line of 200 *nM* concentration.



Figure 7.6: *The fluorescence detection for* 1 *nM filled core (red circles line) and* 0.5 *nM filled core and surrounding 18 holes (purple triangles line)*

In order to find out the detection limits of this technique, lower concentrations (than 100 *nM*) were also measured. Fig.7.6 shows fluorescence measurements of 1 *nM* and 0.5 *nM* concentrations of Alexa-750. However, two scenarios are presented. The first is only for filling the core of the fibre. In this case a fibre length of 33 *cm* corresponds to a 24 *nL* volume of sample. It was possible to measure the concentration of 1 *nM* (red circles line). Taking into calculations volume *L*, concentrations *mol*, and Avogadro's number ($6.022 \times 10^{23}$ $mol^{-1}$), it gives approximately $\approx 14 \times 10^6$ fluorochrome molecules. However, during the preparation of the fibre, the fusion splicer was set to modify the selective filling process parameters. The arc time was reduced to 480 *ms* and the arc power to 3.78*W*. For this case, it was possible to fill not only the fibre core,

but additionally eighteen cladding capillaries close to the core. As a result, a lower concentration of 0.5 *nM* was detected with a fibre length of 31 *cm*, corresponding to a sample volume of 53 *nL* ($\approx 16 \times 10^6$ fluorochrome molecules) as shown in Fig.7.6 (purple triangles line) [196]. The average power ($P_{average}$) launched into all samples was about 62 $\mu W$ at wavelength 750 *nm*.



|  |  |  |
|:---:|:---:|:---:|
| (a) *curved, thin* | (b) *curved* | (c) *straight* |

Figure 7.7: *The side images of collapsed fibres, where the first two images present the curvature in the core line, the last ideal shape of the opening channel*

It is worth noting that the shape of the collapsed part of the fibre ends may have an impact on fluorescence measurements. The collapsed input of the fibre may affect light propagation in the fibre. Fig.7.7 presents examples of collapsed fibre tips. Fig.7.7a and Fig.7.7b show the curved core channel, and any curvature of the core prevents good interaction of light and sample, and compromises sample analysis. Fig.7.8a shows the example of the fibre output, for which we could not launch light into the core and could not detect any fluorescence signal. We can see, that the green light (filtered beam used for the fibre alignment process) is spread out from the core and present in the solid cladding.

Fig.7.7c gives the side view of the fibre with the best parameters for light guidance (i.e. launching light into this fibre is not hindered). Fig.7.8b shows the fibre output with good interaction achieved between light and the sample in the core. This indicates strong green light coming out of the centre of the fibre. In addition, we present in Fig.7.8c the excitation wavelength (740 *nm*), which was propagated solely in the fibre core.

The presented results of the fluorescence detection for Alexa-750 fluorochrome diluted in water with concentration of 0.5 *nM* (navy blue column in Fig.7.9) were compared to the published fluorescence detection using PCFs. Fig.7.9 shows the obtained result for

126

(a)                    (b)                    (c)

Figure 7.8: *The images of collapsed fibres, where the first two images present the fibre during the alignment, where (a) shows the poor light interaction of light and sample, (b) the good interaction, and (c) shows the fibre near field during the fluorescence measurement*



Figure 7.9: *Graph of published results of fluorescence detection for the filled fibres PCFs shown with columns: green - 100 nM of the Cy-5 DNA probe in water [12], light blue - 360 nM of rhodamine in ethylene glycol [20], pink - 1 nM of quantum dots in water [29], dark yellow - 0.2 nM of quantum dots in water [182]*

the Cy-5 DNA detection, where 30 *cm* of HC-PCF fibre was filled with a 100 *nM* of the Cy-5 DNA in aqueous solution (green column). These measurements were published in 2004 by J. Jensen from Research Center COM, Denmark [12]. The next column (light blue column in Fig.7.9) presents the results of C. Cordeiro, from University of São Paolo, Brazil who published on fluorescence detection using the microstructure fibre filled with rhodamine diluted in ethylene glycol. Here, the lowest published concentration was 360 *nM* [20]. In the following years (2007 and 2009) the group from the University of Adelaide, Australia published their results for filling a suspended-core fibre with quantum dots in aqueous solution with concentration of 1 *nM* (pink column)

and 0.2 *nM* (dark yellow column), respectively [29, 182]. To summarise, the test of optical set-up sensitivity, the supercontinuum with 0.55 *ns* peak width and repetition rate of 6.85 *kHz* is a sufficient light source for the fluorescence measurements. This optical configuration (Fig.7.4) can be used for a further step, such as the fluorescence detection of labelled DNA probe immobilised in the hydrogel inside the fibre.

### 7.3.3 DNA detection within hydrogel in HC-PCFs

This section presents the fluorescence measurements for labelled DNA immobilised in the hydrogel. The fluorescence measurements for the fibre filled with Alexa-750 fluorochrome in water solution shows the prospect of the optical configuration in Fig.7.4 with the supercontinuum. It can be successfully used for the fluorescence measurements. In addition, we may expect to detect the fluorochrome molecules concentrations at *nM* magnitude order using this set-up (Fig.7.4). However, in this section we present DNA labelled with Cy-5 fluorochrome. The DNA probe was originally labelled by this fluorochrome in Metabion International, Germany in order to test this DNA immobilisation for future DNA hybridisation measurements. In addition, the Cy-5 fluorescence can be observed using the epi-fluorescence microscope. As presented in Section 7.2.3, we tested these fibres in order to establish DNA probe immobilisation.



Figure 7.10: *The peak counts for a* 10 *μM Cy-5 DNA immobilised in the hydrogel grown on a glass slide*

The experiments are carried out with the arranged Cy-5 filters set, as detailed in Table 7.1 in the optical configuration (Fig.7.4). Similar to testing the optical set-up with a

128

high concentration of Alexa-750 in slide before analysing the fibre samples, we used a high concentration of 10 $\mu M$ of Cy-5 DNA immobilised in the hydrogel grown on the slide. This drop of hydrogel was positioned in front of the lens (no.5) in the optical setup. Instead of using the *x,y,z*-stage (i.e the fibre input), the slide was attached to a round stage with a steel groove slide. Fig.7.10 shows the fluorescence signal (green circles line) for 10 $\mu M$ concentration of Cy-DNA molecules in the hydrogel.

The initial portion of Fig.7.10 shows a low level of counts, and corresponds to the laser beam being blocked using a laser shutter. When the supercontinuum was unblocked (at approximately 4 *s*) the signal increased to a level of $\approx 600$ *counts*. This level was maintained without any observable decay throughout the 95 *s* while the laser light was turned on. It is worth noticing here that a drop 1 *mm* in diameter of the hydrogel has a volume close to 4 $\mu L$. It is not comparable to the volume of the hydrogel in the fibre. 10 *cm* of the fibre length contains 8 *nL* of hydrogel. Furthermore, the detection set-up abilities were determined, and the measurement shown (Fig.7.10) also confirms that the Cy-5 DNA probe was properly attached to the hydrogel.



Figure 7.11: *Graph of peak counts for a leaked supercontinuum signal (black line)*

Here, the test for fluorescence detection was provided for the fibres. In the previous section of this chapter, we demonstrated the immobilisation of Cy-5 labelled DNA in hydrogel grown in the fibre. Here, these fibres (Fig.7.3d) were analysed in terms of the detection of various DNA concentrations as a function of fibre length. According to the approximation of the optimum fibre length discussed in Chapter 6, we tested approximately 10 *cm* of the fibre filled with the hydrogel. At the first stage, instead of filtering the supercontinuum beam with the input filters (no.2) the alignment filter

was used (see Table 7.1). The fibre was attached with fibre clamps to the *x,y,z* stages at both ends, while maintaining the alignment by observing the near-field of the fibre. The supercontinuum beam was blocked, and the alignment filter was changed for the input filters. However, it was found that the average power using the full set of *input* filters for a wavelength of 650 *nm* was only 14 $\mu W$. As a consequence we could not detect any fluorescence coming out of the fibre. In order to increase the power a low-pass filter (i.e. one of the input filters (no.2 in Fig.7.4)) was removed. The supercontinuum beam was filtered with a bandwidth filter (see Table 7.1) and the dichroic (no.3) filter. As a result, the average power increased. However, the supercontinuum light leaked through this set of filters to the detection arm and the measurements were hindered. One example of a high noise signal is shown in Fig.7.11a. The noise (black line) has a peak of around 100 counts. This noise line is not linear, but it did not decay for a long period of time (i.e. longer than 30 *min*). In this graph, 10 *min* of the measurement is presented.



(a) *Empty fibre*  (b) *Hydrogel fibre*

(c) *Water fibre*  (d) 570 *nm*-100 *ms*

Figure 7.12: *The fibres' cross-sections, (a) to measure noise level for a glass reflection, (b) to measure noise level from hydrogel fibre without fluorochrome, and (c) an example of the CCD image during the fluorescence measurements*

Because of such a high noise level, the set of input filters was changed. In this scenario, only the low-pass filter and the dichroic filter were reversed in the set-up and the bandwidth filter was taken out. The average power achieved was 260 $\mu W$. Additional tests to determine the noise level were obtained. As is shown in Fig.7.12, there are three examples of fibres for which the noise level was investigated. The first (Fig.7.12a) is an

empty fibre where the supercontinuum was aligned to a solid cladding fibre to achieve as many reflections as possible. The second is Fig.7.12b which shows the cross-section of the fibre with the hydrogel grown in the fibre core and randomly in the cladding area (without any DNA probe). Fig.7.12c shows the cross-section of the fibre fully filled with water, which is the third tested example. These fibres were aligned in the set-up (Fig.7.4) and the filtered supercontinuum was launched into the fibres.



Figure 7.13: *Graph of noise level, which was used for the further experiments (blue line)*

The detected signal is a noise level for further fluorescence measurements and is shown in Fig.7.13. All of the detected noise was the same for three examples of fibres (Fig.7.12a, Fig.7.12b, and Fig.7.12c). At this stage of the experiment, we could continue the fluorescence detection for Cy-5 DNA probe in the hydrogel grown in the fibre.

Fig.7.12d presents the near-field of the fibre, which was continuously monitored. Four measurements for different Cy-5 DNA concentrations were chosen to be presented in this section: 0.4 $\mu M$, 1 $\mu M$, 6 $\mu M$ and 10 $\mu M$. Fig.7.14 shows the results of Cy-5 DNA probe decays, for three of these concentrations as 1 $\mu M$ (green triangles line), 6 $\mu M$ (blue squares line), and 10 $\mu M$ (red circles line) using HC-PCF 1060 lengths of approximately 10 $cm$ [196]. Due the discussion for the optimum length in Chapter 6, 8 $cm$ should be enough to achieve the best results of the back fluorescence detection. However, according to analysis of the hydrogel distribution from Chapter 5 using 10 $cm$ of the fibre with the polymerisation at both fibre ends may guarantee the complete hydrogel filling along the fibre. It is worth noting here that we do not present the complete line decay. These three lines observed achieved the noise level,

Figure 7.14: *Fluorescence measurements as a function of concentration for a Cy-5 DNA probe incorporated into a fibre filled with hydrogel for concentrations:* 1 *μM green triangles line,* 6 *μM blue squares line, and* 10 *μM red circles line*



Figure 7.15: *The graph of the lowest detected Cy-5 DNA concentration of* 0.4 *μM immobilised within the hydrogel inside the HC PCf 1060*

however, after a long observation time. For example, 6 *min* of measurement for 6 *μM* concentration. Here, we chose to present the highest measured counts. We can also observe that concentrations of 6 *μM* and 10 *μM* have sharp peaks and decay is shorter in comparison to the 1 *μM* concentration line. The fluorescence decay lines intersect at 24 *s* point on the *x-axis*. It is probably associated to a non-linearity of the photo-

bleaching and the intensity dependence. The decay results for the hydrogel are not as smooth as the decay for water results. This may be attributed to the porosity of the hydrogel structure.

However, it was possible to detect much lower concentrations than these presented. Fig.7.15 illustrates a time decay (pink diamonds line) for a 0.4 $\mu M$ Cy-5 DNA concentration diluted in the PVT solution. The highest peak of this measurement was 37 counts. This example of the 0.4 $\mu M$ Cy-5 DNA fluorescence detection in the hydrogel grown in the fibre has been published by our group (the PSG in Tyndall National Institute) for the first time [196]. It is worth to noticing, that the 25% concentration of the PEGDA hydrogel efficiency (i.e. percentage of encapsulated molecules within the gel) was estimated as close to $91\% \pm 5\%$, and these results can be found in the literature [50]. Taking into calculations our results that 400 $nM$ of Cy-5 DNA concentration was diluted in the PVT solution, then we may expected that $364 \pm 20$ $nM$ of Cy-5 labelled DNA probes were encapsulated within the hydrogel and detected using the optical configuration shown in Fig.7.4.

## 7.4 Summary

The Cy5-labelled DNA oligonucleotide detection within the 3D hydrogel matrix grown inside the holes of a HC-PCF was demonstrated here. The lowest measurable concentration of DNA probes diluted in PEG solution was 0.4 $\mu M$, for an applied 260 $\mu W$ average power and excitation wavelength $\lambda = 650$ $nm$.

However, the potential applications to measure fluorescence within water-based solution in the holes of HC-PCF was successfully demonstrated for the lowest concentration of 0.5 $nM$, with the excitation wavelength at $\lambda = 750$ $nm$, and average power of 62 $\mu W$. This concentration is not the minimal possible detectable value. The window to improve results is quite wide, as the pulse counts were 25 times greater than the noise level.

# The suspended-core optical fibre

## 8.1 Introduction

Suspended-core optical fibres belong to a class of photonic crystal fibres, and are commonly called microstructured optical fibres (MOF) [25, 56]. The fibre core is surrounded by three air-capillaries within the solid cladding. It is called a *suspended-core* due to the impression that the core is not connected with any part of the fibre. In this chapter, two types of suspended-core optical fibres are investigated. Both fibres were fabricated in the Laboratory of Optical Fibre Technology in Maria Curie-Skłodowska University, Lublin, Poland and they were named P3 and P7. Fig.8.1a presents suspended-core fibre (P7) which is characterised with large cladding holes 25 $\mu m$ wide. The left panel of Fig.8.1a shows the core area linked with thin silica connection *(struts)*. Fig.8.1b shows the cross-section of P3. This fibre has smaller holes with a width around 11 $\mu m$ a larger core and wider struts compared to the P7 fibre.



(a) *P7*                    (b) *P3*

Figure 8.1: *The suspended-core optical fibres with zoomed-in section of the microstructure cladding, where (a) is P7 and (b) is P3*

Recently, microstructured optical fibres have been proposed for sensing [6, 25, 29, 149, 180, 197]. They can have a vast number of new applications due to their unique cladding structure. Just like HC-PCFs, a sample can be introduced into the fibre air-channels.

The main advantage of the suspended-core fibre is the ability to propagate a broad spectrum of light in its silica core. When inserting samples to its cladding holes, the evanescent field interacts with the sample [149, 179, 197, 198]. The fibre sensor length

can also be tailored.

In this work, the use of hydrogel for anchoring the biosample within the PCF was proposed. It was demonstrated, that the PEGDA hydrogel grows within the HC-PCF [46, 199]. In Chapter 6, we found that the hydrogel has a similar refractive index to water and contains a significant amount of water inside its structure. However, the hydrogel attenuation coefficient is higher than water. The hydrogel porous structure causes light scattering. For these reasons, the suspended-core optical fibre has been proposed for integration with the hydrogel. By introducing the hydrogel within cladding holes, and not in the core like in HC-PCFs, the effect of attenuation due to the hydrogel would be minimal, and hence possible long interaction lengths may be used. The suspended-core fibre would propagate excitation and emission wavelengths along its silica core. In particular, the hydrogel initiating process may be more accurate. This is because the photo-initiating signal may be guided by the core. The excitation of the Eosin Y and the resulting polymerisation of the PVT solution would be more uniform. Consequently, the hydrogel matrix should grow over a greater length of fibre compared to HC-PCFs. Moreover, due to incomplete filling of the holes in the fibre caused by polymerisation the hydrogel close to the core should promote access to the DNA-target. This may improve the efficiency of DNA probe hybridisation.

Overall, in this chapter the suspended-core optical fibre, its light guidance properties, hydrogel growth and DNA immobilisation are investigated.

## 8.2 Numerical modelling of light propagation



(a) *Fibre Structure*      (b) *Applied Mesh*

Figure 8.2: *The fibre structure (a) applied in a numerical modelling (b) applied mesh for the fibre structure*

In order to characterise light propagation in the suspended-core optical fibre, numerical modelling in the Comsol Multiphysics package was performed. Details about

this modelling can be found in Chapter 2 and in [198]. Fig.8.2a presents the drawn part of the fibre (using AutoCad package), where orange areas indicate the silica part such as struts, and at the centre is the core with refractive index $n_{silica} = 1.45$. A white area surrounding the three orange arms indicates air holes in the cladding, with a refractive index $n_{air} = 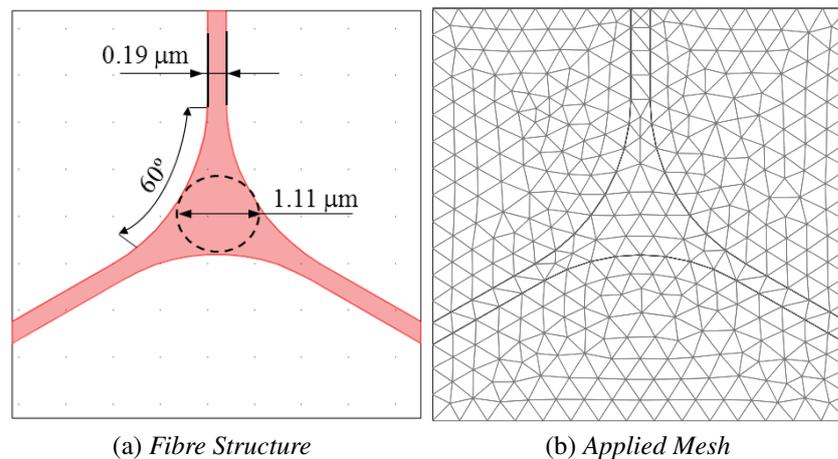1.00$. The fibre core is extremely small and is marked with a black dashed line. The diameter of the in-circle core is estimated as close to 1.1 $\mu m$; the silica struts have a width of 0.19 $\mu m$, and are placed at a $60°$ angle to each other. On the right side, Fig.8.2b, the applied mesh in the numerical model is shown. The number of elements is 680. The structure is invariable in the *z*-direction. Here, we focus on the effective index value for a certain wavelength and its diagram, which is then attributed to an optical mode for this fibre (see Chapter 2).



|     |     |     |     |     |
|:---:|:---:|:---:|:---:|:---:|
| (a) | (b) | (c) | (d) | (e) |

Figure 8.3: *Field patterns for the suspended-core optical fibre*

Similar to HC-PCFs, an optical field pattern analysis was investigated for the super-continuum. The analysis begins at wavelength $\lambda = 350$ *nm* and finishes at wavelength $\lambda = 1700$ *nm*. The analysis started at wavelength $\lambda = 350$ and for this wavelength, ten different values for the effective index were calculated (see Chapter 2). The applied interval of the effective index number was close to 1.449. Each effective index illustration either gave no solution or field patterns were formed, some of them are shown in Fig.8.3. Afterwards, calculations were repeated for the start wavelength with successive increments of 50 *nm* steps (i.e. the scanned wavelength was 400 *nm*) until wavelength $\lambda = 1700$ *nm* was achieved. For each wavelength, ten different numbers for the effective index were calculated. Fig.8.3a for example, resembles a centralised the *fundamental-like mode*, with the highest intensity localised at the centre. We could also observe different light confinement. Fig.8.3b demonstrates some of examples of light confinement in one strut, or in two (Fig.8.3c). Fig.8.3d shows for example three light intensity maxima close to the centre of the core, where Fig.8.3e shows the light spread to three struts and a low intensity light in the core.

During this analysis, it was observed that at wavelengths as short as $\lambda = 650$ *nm*, the field pattern was tightly confined in the core as is shown in Fig.8.4a. Using Nikon software we could approximate the area of field (i.e. the area of the triangle). Due to this, the optical field at wavelength 650 *nm* in Fig.8.4a was close to 1.62 $\mu m^2$. In

Figure 8.4: *Field patterns distribution generated for wavelengths: (a-b) 650 nm and (c-d) 1550 nm - unfilled and filled with water, respectively*

comparison, Fig.8.4c shows the field pattern for $\lambda = 1550 \ nm$. Here, we can observe that this field has spread out of the core and the evanescent field is present. When the refractive index of the cladding holes was changed to 1.33 instead of 1.00, the field pattern spread out from the core even more. Fig.8.4b resembles the *fundamental mode* due to the highest intensity at the centre, at $\lambda = 650 \ nm$. However, it leaked out of the silica part. This field increased as shown in Fig.8.4b around 30% compared to that shown in Fig.8.4a. Fig.8.4d presents a wider evanescent field for the changed refractive index in the cladding holes at the longer wavelength $\lambda = 1550 \ nm$. Comparing the field of Fig.8.4c to that in Fig.8.4d, there is a 50% increase. Similar effects were previously published in [197, 198, 200]. It can be assumed that filling the fibre with water ($n_{water} = 1.33$) affects light confinement in the core. This causes a stronger evanescent field.

As was described in Chapter 2, using the effective indices as a function of wavelength we could estimate the fibre transmission region. Fig.8.5 shows a collection of effective indices only of the field pattern confined at the centre of the core as a function of wavelength ($LP_{01}$-*like* - red dot). The range of effective index was quite broad at $1.20 < n_{eff} < 1.40$ for the range of spectrum $350 \ nm < \lambda < 1700 \ nm$. Thus, this fibre should have a broad transmission spectrum.

Figure 8.5: *Graph of effective index against wavelength, for the field pattern with the highest intensity centred at the core*

## 8.3 Optical characterisation



Figure 8.6: *The optical setup to detect transmission spectra, with the suspended-core optical fibre, and CCD- camera, PC-desktop, SM-spectrometer, MM-multimode fibre*

In this section, we present the near-field images and the transmitted spectra of suspended-core optical fibres. We investigate a propagation for wavelengths $\lambda = 530\ nm$, which are responsible for the hydrogel photo-polymerisation process (as explained in Chapter 5). The same is done for $\lambda \approx 650\ nm$, which is needed to excite the attached fluorochrome to the DNA probe (also described in Chapter 7). Fig.8.6 demonstrates a schematic of the experimental set-up. A similar optical set-up was constructed for HC-PCFs as explained in Chapter 2. However, both fibre cores (P7 and P3) are ten times smaller in comparison to HC-PCFs. Therefore, the lens focusing light into the fibre (no.4) was replaced with a microscope objective lens (Newport, $M \times 60$, $NA = 0.85$, $FL = 2.9\ mm$). To place the fibre (no.5) at the focal point of this lens, the fibre end-face should be positioned 0.3 *mm* from the lens. In practice, it was useful to connect the $x,y,z$-stage to piezo-controllers and control the short distance between the

138

fibre and the lens with an electronics controller. In addition, light transmitted through the fibre was collected with an infinity corrected lens (no.6) (see Chapter 3) with the parameters (Newport, $M \times 60$, $NA = 0.85$). Then the lens was attached to an $x,y,z$-stage with an objective mount (Newport, 561-OBJ) with $\sim 0.3$ *mm* distance from the fibre end-facet. Since the image of the fibre end-facet was still very small, the fibre image was magnified by a factor of two in CCD. In order to record the transmitted light, the set-up was connected to a spectrometer (Ocean-Optics HR4000) with an aspherical lens and multimode fibre (see Chapter 2). The spectrometer detects a range of wavelengths from 200 *nm* to 1100 *nm*.



Figure 8.7: *Near-field images for supercontinuum propagation for the P7 (upper row) and P3 (lower row) suspended-core fibres*

Fig.8.7a presents near-field image of the suspended-core fibre (P7) when the supercontinuum signal was fully launched into the fibre. Although the collecting lens has insufficient numerical aperture we observe a strong intensity spot at the centre of the fibre, indicating strong confinement in the core. Fig.8.7b-e show near-field images when the filtered supercontinuum light was launched into the fibre. By adjusting the coupling distance from the lens to the fibre, the launching conditions obviously changed, enabling different wavelengths to be propagated with different intensities as seen through Fig.8.7b-e. In order to reduce the lens effects, a set of collecting lenses was employed. For example, a lens of $NA \approx 0.66$ and $Mx40$ and another lens of $NA \approx 0.40$ and $Mx20$ were used to repeat the same measurement. However, in all cases, the image of the core was still not clear due to the decreased magnification of the lens and the very small dimensions of the core. We also experimentally tested the suspended-core fibre named: P3 (Fig.8.7f-j) which has larger dimensions than P7. The same effects were observed. However, the pictures show strong core confinement for many wavelengths for fully launched supercontinuum (Fig.8.7f) and for the case of filtered light ( Fig.8.7f-j).

Figure 8.8: *The supercontinuum propagation profile for the P7 suspended-core optical fibre*



Figure 8.9: *The supercontinuum propagation profile for the P3 suspended-core optical fibre*

Fig.8.8 and Fig.8.9 present the transmitted spectra for the fibres P7 and P3, respectively. Both spectra are similar, showing a broadband propagation around the visible and near-IR regions. However, a much broader range of wavelengths was expected [25, 197]. The inconsistencies probably happened experimentally due to the small cores size and non-optimal optics.

140

### 8.3.1 Fibre filling

Here, filling of the suspended-core fibre is demonstrated. The theory behind the filling process is identical to that presented for HC-PCFs in Chapter 4. At the first stage of filling tests, the fibre P7 was chosen.



(a) *unfilled*       (b) *water*       (c) *damaged fibre*

Figure 8.10: *The cross-section of P7 suspended-core fibre during a filling with water*

Fig.8.10a shows the cross-section of the fibre, which was connected by a fibre clamp to an optical microscope bench. The other end of the fibre was put into a beaker filled with water. The fibre filling process took place without any applied external pressure. Fig.8.10b shows the end-facet of the fibre, which is filled by water (white shapes in the fibre holes). When the fibre lost contact with a liquid in the beaker, water flowed down. Unfortunately, it was found that the microstructure part of the fibre was damaged. The capillary force was strong enough to break fragile silica struts and displace the core as demonstrated in Fig.8.10c (the core area is marked with a red dashed line). We did not use P7 fibre for any further tests of fibre fillings and integration of this type of fibre with the hydrogel.



(a) *unfilled*       (b) *water*       (c) *near field 1*

Figure 8.11: *The cross-section of P3 suspended-core fibre, (a) unfilled and (b) filled with water, (c) near-field image for supercontinuum propagation*

In the second order of the filling process, the P3 fibre was tested. Fig.8.11a shows the image of the fibre end-facet before the filling process. Fig.8.11b shows the cross-section of the fibre filled with pure water. No evidence of broken struts were found for

this fibre, even when the external pressure was applied. The filling of the fibre with an external pressure was identical to that shown in Chapter 4 for the HC-PCF. The fibre was connected to the syringe set-up (i.e. a syringe with a complex of plastic tubing connected to a syringe pump).

In addition, the filled P3 fibre was tested in the experimental set-up as that described in Fig.8.6. The full supercontinuum was launched into the fibre. The focusing of light into the core of the filled fibre was possible without any disturbance of the presence of water in the fibre holes. Fig.8.11c shows the near-field of the filled fibre. Here, we can observe the intense yellow dot at the centre of the fibre. It can be assumed, that the supercontinuum is propagated in the core of the fibre. Afterwards, the CCD camera was removed from the set-up and the transmitted light was analysed in the spectrometer (no.12 in Fig.8.6).

Figure 8.12: *The supercontinuum propagation profile in suspended-core optical fibre, where a dark cyan line represents unfilled fibre, a blue line that filled with water*

Fig.8.12 shows the transmitted light (blue-line) of the filled fibre. In order to compare spectra of filled and unfilled fibres, in Fig.8.12 the transmitted light of the unfilled fibre spectrum (green line) is added. The water attenuation has a minimal impact for propagating wavelengths 500 *nm* to 700 *nm* (i.e. both lines of spectra overlap). At the right side of the spectrum for wavelengths from 750 *nm* to 1000 *nm*, we can observe a reduced intensity for the filled fibre (i.e. blue line in this region lays lower than the green line). This intensity decay is attributed to water attenuation (see Chapter 2).

Note that this fibre (P3) has been qualified for further tests, such as the hydrogel growth process.

## 8.4 Hydrogel growing process

The silanisation process and the hydrogel photo-polymerisation are carried out for a suspended-core optical fibre using the same chemical protocol and experimental configuration that was previously applied for HC-PCFs (described in Chapter 2 and Chapter 5) [46, 199, 201].

### 8.4.1 Silanisation process

For HC-PCFs, it was possible to investigate the presence of Eosin Y attached to the fibre glass. The fibre was tested in the optical microscope (Nikon Eclipse ME600) and the epi-fluorescence microscope (Olympus IX81) with the set of filters determined in Chapter 7. The suspended-core fibre end-facet has been tested using an identical procedure. Fig.8.13 presents a selection of fibre cross-section images. In its left panel (Fig.8.13a, Fig.8.13c, Fig.8.13e) are images for the fibre before the silanisation process. On the right panel (Fig.8.13b, Fig.8.13d, Fig.8.13f) are corresponding images after the silanisation process. Fig.8.13a and Fig.8.13b show the fibre cross-section which was observed in an optical microscope. When the bright light is used, the particular green reflection from the silanised part of fibre is present (green colour around the core in Fig.8.13b). This is attributed to the Eosin Y presence inside the fibre. A similar effect was observed for HC-PCFs and was presented in Chapter 6). The other two images, Fig.8.13c and Fig.8.13d, present the fibre end-facet taken in a fluorescence microscope using the FITC dichroic filter (see Chapter 7). The fibre before silanisation has a green reflection from the silica glass in the cladding and the core is difficult to see. When the fibre was silanised, a green reflection was observed in the core area (a green triangle at the centre of the fibre). This reflection is much more intense, compared to that from the cladding glass. It is a mixture of exciting and emitting light of Eosin Y (see Chapter 7). The last example, Fig.8.13e and Fig.8.13f, are images of the fibre as observed in a fluorescence microscope, with a Cy-3 dichroic filter (see Chapter 7). Similar to the above examples for the fibre before the silanisation process (Fig.8.13e) there is an orange colour reflecting from the solid cladding. When this fibre was silanised, in Fig.8.13f, we observed a much brighter reflection from the core than from the solid cladding (shown as yellow triangle). This is the light emitted from Eosin Y. In summary, we could observe reflections of Eosin Y from the core area and the photo-initiation process should be possible.

(a) *1*        (b) *1*





(c) *2*        (d) *2*





(e) *3*        (f) *3*

Figure 8.13: *The suspended-core fibre with the grown hydrogel in the cladding holes and around the core, the first (1) row are imaged in an optical microscope, in the second (2) row are images for a fluorescence microscope using FITC dichroic filter, and the third (3) row are images for a fluorescence microscope using a Cy-3 dichroic filter*

## 8.4.2 DNA immobilisation within the PEGDA hydrogel

In this section, hydrogel grown with DNA immobilisation for the suspended-core fibre is demonstrated. In order to immobilise the labelled DNA probe within the hydrogel, the procedure was repeated as for HC-PCFs [201]. The Cy5-DNA was first diluted in the PVT solution using various concentrations. Next, the silanised fibre as shown in Fig.8.13b, Fig.8.13d and Fig.8.13f was filled with this solution. The process of photopolymerisation of the hydrogel with bonded DNA probe molecules was initiated. This

process and the experimental set-up are described in Chapter 5. Fig.8.14a shows the fibre end-facet with the presence of hydrogel. Here, we can observe the hydrogel attached to the outer part of the cladding holes (shown with red arrows in Fig.8.14a) using an optical microscope. In the next stage, this fibre was tested using the epi-fluorescence microscope. The hydrogel matrix incorporates Eosin Y molecules with fluorescence in the wavelength range $520\,nm < \lambda < 580\,nm$. This enables its structural composition to be examined with a fluorescence microscope using the FITC filter and the Cy-3 filter (see Chapter 7). Fig.8.14b and Fig.8.14c also show the hydrogel (directed with red arrows) grown in the outer part of the cladding holes. The matrix was observed with FITC and Cy-3 filters, respectively. Therefore, in order to analyse DNA probe immobilisation within the hydrogel, it is necessary to use fluorochrome operating above wavelengths $\lambda > 570\,nm$. The DNA is labelled with Cy-5 fluorochrome, identical to that used for HC-PCFs (see Chapter 7). The specifications of the Cy-5 fluorochrome and fluorescence processes can be found in Chapter 2.



Figure 8.14: *The suspended-core fibre with the hydrogel grown in the cladding holes and around the core, observed through (a) optical microscope, (b,c,d) fluorescence microscope, with (b) FITC dichroic filter, (c) Cy-3 filter, (d) Cy-5 filter*

Fig.8.14d demonstrates successful immobilisation of Cy5-DNA in the hydrogel grown inside the fibre. The DNA is present in the hydrogel in the cladding holes. The DNA concentration was $400\,nM$. We can observe the hydrogel grown in the upper part of the holes, as in Fig.8.14a to Fig.8.14c. However, for these images we could not

see the hydrogel around the core. When the filter was changed above the hydrogel sensitivity range, the fluorescence signal appeared additionally in the core of the fibre. The hydrogel matrix around the core was probably so thin that we could not see it before. However, for the fluorescence signal one can see that it was confined in the silica core. The core of suspended-core fibre is extremely small. Here, we assumed that the emitted photons of fluorochrome were trapped in the core of the fibre. Thus, we do not observe the fluorescence signal around the core where the hydrogel matrix is, but rather from the core [201]. On one side, this fibre example confirms our preliminary condition of proposing this fibre for integration with the hydrogel. On the other side, this fibre shows that the hydrogel has grown, but not only around the core. This can be attributed to the focusing lens which launched the laser beam into the fibre for the photo-initiating process. This lens had a larger light spot size than, the core area. Not only Eosin Y attached to the core area was excited. In addition, these molecules attached to silica walls in the fibre were also excited. It is difficult to technically avoid the problem of growing the hydrogel outside the core area. Unfortunately, the fluorescence from those regions would not provide the fluorescence signal in the core.



(a) *Bright light*          (b) 520 *nm*

Figure 8.15: *The suspended-core fibre with the grown hydrogel, (a) no evidence of DNA probe, (b) Cy-5 labelled DNA are trapped in the core of fibre*

We further analysed the fibre example of immobilised DNA within the hydrogel, and its cross-section is presented in Fig.8.15. Here, Fig.8.15a shows the fibre in the absence of DNA molecules being tested in the fluorescence microscope using the Cy-5 filter. The image is black, showing no Cy-5 labelled DNA probe. There is no reflection from the solid glass at these wavelengths. However, Fig.8.15b shows the fibre cross-section for which DNA was immobilised in the hydrogel with a 1 $\mu M$ concentration. The fluorescence signal is transmitted in the silica core of the fibre, instead of being transmitted in the hydrogel structure. For this example, a good agreement with the theoretical assumption is also achieved.

The suspended-core optical fibres were subjected to preliminary tests to improve the

(a) *Bright light*     (b) *Polarised light*     (c) *Near-field*

Figure 8.16: *The suspended-core fibre with the grown hydrogel, (a) with a bright light, (b) linearly polarised, labelled bright light, (c) the near-field image*

hydrogel growth process. This is according to the hydrogel distribution for the HC-PCF and technical difficulties with the hydrogel growth for the longer fibre length than 5 *cm* (see Chapter 5). It was demonstrated that Eosin Y molecules are responsible for the polymerisation of the hydrogel. Then, an increase in the number of Eosin Y molecules may achieve more efficient hydrogel growth. In this test, 17 *mg* of Eosin Y were added to 1.5 *mL* of the PVT solution (see Chapter 5). The photo-initiation process may excite Eosin Y attached to the core and silica struts of the fibre. In addition, Eosin Y inside the PVT solution may also be excited. It was expected to observe the improved volumetric structure of the hydrogel. Fig.8.16a demonstrates the cross-section of 16 *cm* of the fibre, after the polymerisation. The hydrogel structure is marked with a red-arrow. Here, we can observe the hydrogel growing around the core. In comparison to Fig.8.14a, it is possible to see the hydrogel using an optical microscope. The air channel diameter was measured at 11 $\mu m$. The hydrogel has an ellipse shape of $r_1 \approx 1.5$ $\mu m$ and $r_2 \approx 5$ $\mu m$. Then, it is estimated using the ratio of the hole area to the hydrogel area, that 25% of each hole is filled by the hydrogel. In the previous results the width measurements were not possible. Fig.8.16b shows the same fibre cross-section, now illuminated with polarised light. The use of polarised light in a microscope helps to distinguish reflection from the glass and any other surfaces, such as water or hydrogel. We can see here that the hydrogel *glows* (bright yellowish triangle at the centre of the fibre). Moreover, this fibre was tested using side-view scanning and the presence of the hydrogel was verified along the whole fibre. Finally, Fig.8.16c presents the near-field image of our fibre, tested with the supercontinuum signal in the optical set-up (Fig.8.6), where the fibre length was 16 *cm*. To conclude, the increment of Eosin Y concentration during the silanisation process and adding these molecules to the PVT solution improve the hydrogel growth within the fibre.

## 8.5   Summary

In conclusion, the suspended-core optical fibre was presented and its light propagation characteristics were discussed. It was observed that the fibre transmits the full supercontinuum signal in the core. The theoretical field pattern analysis utilized with the numerical model package agreed with the experimental results provided for the optical field analysis and transmission spectra.

The successful hydrogel matrix growing process and immobilisation of the DNA probe for the suspended-core optical fibre was also demonstrated. The propagation of the fluorescence signal in the core of the fibre makes this fibre a promising candidate for use in labelled DNA sensors, with enhanced sensitivity. The preliminary tests to improve the hydrogel filling percentage using Eosin Y in the PVT solution also been shown.

# Conclusions and further development

Hollow-core photonic crystal fibres and suspended-core optical fibres have been demonstrated for use in biosensing. There are many advantages of using these fibres as sensors. They have a quick and simple fibre filling process and show good interaction between light and sample, with a fibre length that can be tailored. In addition, a major benefit of using HC-PCF in biosensing is the possibility of controlling the propagation region with the introduction of materials of different refractive indices. On the other hand, suspended-core optical fibres offer light propagation at any wavelength over a broad spectrum range in the tiny silica core. It has been presented that these fibres can be integrated with the hydrogel material. The hydrogel material immobilising the DNA probe has been verified using both fibres. Thus, both of these fibres are successful candidates for a new DNA device, which may be applied for a point-of-care method.

## 9.1   Conclusions

This thesis includes the introduction of photonic crystal fibres, their popularity and most importantly, their novelty in biosensing applications. Their periodic microstructure cladding emphasis guidance of a certain wavelength along the fibre in the air-core. It was shown that the complexity of microstructure cladding creates a narrow propagation band in its spectrum. Interestingly, in HC-PCFs certain wavelengths propagate within this region through air. Thus, importantly, HC-PCFs support propagation of high intensities through the air-core.

We have also shown the analysis of field patterns using the finite element numerical method (Comsol Multiphysics v.3.5a). For the HC-PCF which has a periodic cladding in a triangular lattice (consisting of curved corner hexagons with a pitch of 2.75 $\mu m$) the region where the fundamental-like modes were observed was found for the wavelengths region: 950 $nm$ to 1300 $nm$. The change of refractive index to a value of 1.33 instead of 1.00 for the internal channels has been investigated for two scenarios. When the refractive index is changed within all channels of the fibre, the propagation

band is shifted to a new wavelength region of 450 *nm* to 650 *nm*. This shift was found using a numerical method and also using the transmitted spectrum for the filled fibre with water. When the refractive index is changed selectively (i.e only within the core of the fibre), it was determined with numerical modelling and the use of the transmitted spectrum for case when only the fibre core is filled with water, that index-guiding dominates light guidance. Thus, the proposed model of the fibre structure and numerical solver is in good agreement with the experimental tests and also with referenced publications.

The HC-PCF has been presented as a biosensor with the possibility of filling this fibre with a liquid sample. The number of filled cladding capillaries can be controlled with different techniques presented here. In this thesis, the fusion splicing method has been adopted. The physics behind the filling process was found using a comparison to filling a glass capillary by capillary action and laminar flow parameters. The experimental presentation of filling the fibre non-selectively and selectively has been investigated using water and isopropyl alcohol. In addition, a technique of filling the fibre has been demonstrated with and without the use of external pressure. Herein, we have presented a sequence of microfluidic devices to connect the fibre to a syringe. For the first time, it was presented, that the hydrophobic properties of the glass causes delayed filling time of the fibre [30]. This presentation was completed with a description of a novel application of HC-PCFs as a new device, to determine fluid viscosity. In order to calculate viscosity, we proposed recording the time required to fill a certain fibre length [44].

The HC-PCF was integrated with a special filling material in order to develop the DNA detector. The chosen material was the PEGDA hydrogel. The applications of three-dimensional biomaterial, and related chemistry and morphology have been investigated in this work. The hydrogel used was a polymer formed by two polymers poly(ethylene) glycol and 1-vinyl-2-pyrrolidinone, cross-linked with free-radicals: Eosin Y and triethanolamine. The hydrogel was found to be a nanoporous material. Studies have shown that changing the chemical component proportions can tailor the porosity of the hydrogel [195, 199].

The integration of the hydrogel with the PCF offered the stability of filling without leakage of the material, demonstrated mobility for filled fibres and the potential for repeating the optical tests. The hydrogel has been demonstrated to be covalently attached to the silica internal surface of the fibre. It was necessary to chemically prepare the internal fibre surface with the silane agent: APTMS and Eosin Y, which are bond to the internal fibre walls. Therefore, the silanisation and photo-initiation techniques have been adapted and improved for HC-PCFs. It was observed, that the polymerisation begins from the silica part of the fibre core circumference. However, due to the hydrogel distribution analysis, it has been observed that the hydrogel was grown irreg-

ularly inside the fibre. Two techniques: cleaving and side-view scanning methods have been developed. The side-view scanning method has demonstrated that the hydrogel was grown in the first 4 *cm* of the fibre at both ends [46].

For the HC-PCF, the hydrogel acts as a waveguide material. Thus, the optical properties of hydrogel, refractive index and attenuation were investigated. The refractive index of hydrogel has been approximated as close to that of water (1.33). This analysis was provided for wavelength 650 *nm*. This discussion has been supported with comparison of the results for a water solution. The attenuation was assumed to be a combination of absorption and scattering effects and the hydrogel attenuation was approximated as $0.46 \pm 0.16 \ cm^{-1}$. This number has been established by input and output power measurements of different fibre samples filled with the hydrogel.

In order to detect the fluorescence signal within the filled fibre by water and the hydrogel with fluorochrome such as Alexa-750 and Cy-5 the optimum fibre length was investigated. It was calculated that it should be possible to detect 1 $\mu M$ concentration with the highest back-fluorescence intensity for the fibre filled with water longer than 50 *cm*. For the fibre filled with the hydrogel, the optimum fibre length should be longer than 10 *cm* in order to detect the back-fluorescence with highest intensity for 1 $\mu M$ concentrations [46, 195].

As proof of concept for this project, labelled DNA probe immobilisation and detection has been demonstrated within the hydrogel matrix grown inside HC-PCFs. At first, DNA immobilisation has been demonstrated with the assistance of a fluorescence microscope. This was successfully verified for the hydrogel grown inside fibre HC-PCF 1060 and for hydrogel grown on the microscope slides. Next, the immobilised DNA within the hydrogel bonded to the inner surface of HC-PCF 1060 has been tested in the optical setup as a function of the fibre length and the labelled DNA probes concentrations. The lowest measurable concentration of DNA probes diluted in the PVT was 0.4 $\mu M$, for an applied 260 $\mu W$ average power at the excitation wavelength $\lambda = 650$ *nm* [196].

In addition, the potential applications for measuring fluorescence within water based solutions for the HC-PCF has been successfully demonstrated for the lowest concentration of 0.5 *nM* at the excitation wavelength $\lambda = 750$ *nm* and average power of 62 $\mu W$. Here we used a 30 *cm* length of fibre. This result established the sensitivity of our set-up. However, these results can even be improved, due to the fact that the minimal detectable number was twenty-five times greater than the noise level [196].

In the last part of this work, the suspended-core optical fibre was tested for integration with the PEGDA hydrogel matrix. Here, the suspended-core has been demonstrated and verified. Transmission spectra and optical field pattern analysis have been performed using a numerical model and optical set-up. Guidance of excitation and emission wavelengths for commonly-used dyes and Eosin Y has been observed in the

silica core. This may allow for improvement of the hydrogel polymerisation and propagate the fluorescence signal in the core of the fibre instead of though the hydrogel. Due to this fact, the hydrogel attenuation may not have such a strong impact as it does for a HC-PCF. The filling process of suspended-core fibre has been tested and the silanisation process has been completed. The successful hydrogel growth and labelled DNA probe immobilisation within the hydrogel for suspended-core optical fibre has been demonstrated. At the end, a preliminary result in order to improve the hydrogel distribution has been provided. It was presented that increasing the concentration of Eosin Y molecules present on the glass surface and adding Eosin Y molecules to the PVT solution before the photo-initiation process strongly improves hydrogel coverage inside the fibre [201].

Generally, all techniques and methods used for light propagation analysis such as numerical modelling and optical set-up, and also the silanisation process and the hydrogel polymerisation were cross-checked for the suspended-core optical fibre. The suspended-core optical fibre was successfully adapted into these procedures. Thus, it can be concluded, that the developed methods for the integration of photonic crystal fibre with the hydrogel in order to develop a new biosensor have been presented with success and may be universally adapted into any PCFs [195].

## 9.2 Future work

At the end of this thesis, 'Biosensors using a photonic crystal fibre' future research is proposed. Most definitely, the hydrogel biomaterial fulfils criteria for integration with PCFs. Considering the hydrogel abilities to immobilise biomolecules within its internal structure, the advantages (chemical bonding to the internal part of the fibre, avoiding leakage and improving fibre transportability) make the hydrogel a good candidate for a fibre filling material. However, hydrogel attenuation has been found to be $0.46/cm$. There is a possibility to improve the optical hydrogel properties with optimisation of the PVT concentrations. All of the presented results were obtained using a standard 25% PVT solution. We propose to optimise the concentration of the PVT chemical compounds. Re-optimisation of the PVT to a concentration of 12.5% may alter the permeability of the hydrogel. This may improve guidance at the fluorescence wavelength within the hydrogel. Thus, a higher sensitivity of the immobilised probes within hydrogel may be expected.

The hydrogel distribution and capacity within fibres may be improved with the additional presence of Eosin Y in the PVT solution and applying a higher concentration of Eosin Y during the silanisation process. Thus, the uniformity of the hydrogel

distribution inside the fibre may be better tuned for improving fluorescence sensitivity. It is recommended to test the hydrogel growing process for different Eosin Y concentrations.

The DNA probe immobilisation within the hydrogel was prepared not only for the DNA detection, but in particular for a DNA probe selection, known as DNA hybridisation. Inside the hydrogel, labelled-ssDNA target (single strand DNA) is immobilised. Another ssDNA, which is called the signalling probe, is complementary to the target ssDNA. The signalling probe is positioned outside of the hydrogel. Due to the porous hydrogel characterisation, the ssDNA can penetrate the hydrogel. If both of the complementary DNA strands unite, the fluorescence profile will verify the presence of the target DNA. Hybridisation of DNA within the hydrogel has been designed for the identification of mutations and diagnosis of genetic diseases [49, 202]. Hydrogel optical properties and distribution should be improved. This is of primary importance. Subsequently, it is proposed that a test for DNA hybridisation using the PEGDA hydrogel be performed with PCFs.

# Appendix to chapter 3

In this appendix we shall presents another two hollow-core photonic crystal fibre, such as HC-PCF 800 and HC-PCF 1550. In addition are presented calculations to find Helmholtz equation as solution of four Maxwell's equations.

**Hollow-core PCF 800 and hollow-core PCF 1550**

Hollow-core photonic crystal fibres have various structure geometries. The HC-PCF used in this project was mainly HC-PCFs 1060, whose specifications are presented in Chapter 3. During this project another two fibres were investigated: HC-PCFs 800 and HC-PCFs 1550 with following specifications:



(a) *HC-PCF 800*        (b) *HC-PCF 1550*

Figure A.1: *The cross-section images of (a) HC-PCF 800 and (b) HC-PCF 1550 courtesy of NKT Photonics A/S*

Fig.A.1a shows the HC-PCF 800. It had the core diameter $D_c = 7.5$ $\mu m$ and the pitch $\Lambda = 2.3$ $\mu m$. The holey region had a diameter $d_{holey} = 45$ $\mu m$ and the fibre diameter $d_{fibre} = 130$ $\mu m$. In fact this fibre guided the range of wavelengths, close to $\lambda \approx 800$ $nm$, with a transmission band $\gg 100$ $nm$.

Fig.A.1b shows the HC-PCF 1550. Here, the core diameter was $D_c = 10.9$ $\mu m$ and the pitch $\Lambda = 3.8$ $\mu m$. The holey region had a diameter $d_{holey} = 70$ $\mu m$ and the fibre diameter $d_{fibre} = 120$ $\mu m$. In fact this fibre guided the range of wavelengths, close to $\lambda \approx 1550$ $nm$, with a transmission band $\gg 200$ $nm$. The fraction of light in air was greater than 95%.

# Appendix to chapter 2 and 4

In this appendix we shall show the steps taken to derive an equation of fibre length as a function of filling time. Finally the calculations to find the fraction of viscosity to surface tension are presented from the filling equation.

## 1. Details of calculations for Chapter 2

### Equation of length as a function of filling time

For the first step capillary action, Poiseuille flow and overpressure are redefined as functions of force.

(a) the capillarity was recalculated as the capillary force $\vec{F}_c$, where capillarity is expressed with the following equation [91]:

$$L \;=\; \frac{2\sigma \cdot \cos\theta}{r \cdot g \cdot \rho} \tag{B.1}$$

Then, $L$ is multiplied by the denominator of a right side fraction.

$$L \cdot r \cdot \rho \cdot g \;=\; 2\sigma \cdot \cos\theta \tag{B.2}$$

Both sides of the equation are multiplied by $\pi$

$$\pi \cdot r^2 \cdot L \cdot \rho \cdot g \;=\; 2 \cdot \pi \cdot r \cdot \sigma \cdot \cos\theta \tag{B.3}$$

Then, at the left side we see that $L\pi r^2$ can be expressed as the volume

$$V \cdot \rho \cdot g \;=\; 2\pi \cdot r \cdot \sigma \cos\theta \tag{B.4}$$

Again at the left side, $V\rho$ can be expressed in terms of mass, which is volume multiplied by density

$$m \cdot g \;=\; 2 \cdot \pi \cdot r \cdot \sigma \cdot \cos\theta \tag{B.5}$$

where mass multiplied by a gravitational constant is defined to be a force. Here we have equation for capillary force ($\vec{F_c}$).

$$\vec{F_c} = 2 \cdot \pi \cdot r \cdot \sigma \cdot \cos\theta \tag{B.6}$$

where for a filled capillary, $\sigma$ is the surface tension, $\theta$ is the angle between the liquid and the surface of the capillary, $r$ is the radius of the capillary, $g$ is a gravitational constant, which equals $g = 9.81 \ m/s^2$, $\rho$ is the liquid density, $\pi$ is a constant and equals $\pi \approx 3.14$, $V$ is volume and $m$ is the mass.

(b) Poiseuille flow gives us information about the friction force $F_f$ with the following equations - Poiseuille's Law formula is described as [91]:

$$Q = \frac{\pi \cdot r^4 \cdot P_p}{8 \cdot \mu \cdot L} \tag{B.7}$$

$Q$ is multiplied by the denominator of the right side fraction in order to find $P_p$

$$Q \cdot 8 \cdot \mu \cdot L = \pi \cdot r^4 \cdot P_p \tag{B.8}$$

Then the left and right sides of the above equation are replaced and divided by $\pi$ and radius. Pressure equals:

$$P_p = \frac{A \cdot \vec{v} \cdot 8 \cdot \mu \cdot L}{\pi \cdot r^4} \tag{B.9}$$

Pressure is a force, which acts on a particular area:

$$\vec{F_f} = \frac{A^2 \cdot \vec{v} \cdot 8 \cdot \mu \cdot L}{\pi \cdot r^4} \tag{B.10}$$

Right side is divided by area in order to find formula for friction force:

$$\vec{F_f} = \frac{\pi^2 \cdot r^4 \cdot \vec{v} \cdot 8 \cdot \mu \cdot L}{\pi \cdot r^4} \tag{B.11}$$

Dividing the common factors gives,

$$\vec{F_f} = 8 \cdot \pi \cdot \mu \cdot L \cdot \vec{v} \tag{B.12}$$

where $\vec{v}$ is velocity, $\mu$ is dynamic viscosity, $Q$ is flow rate.

(c) Here we consider that an external pressure is applied and pressure equals to force, which acts on an circle area (i.e. circular capillary) is a product of radius square and $\pi$. Then, the external pressure force equals:

$$\vec{F_p} = \pi r^2 \cdot P_p \tag{B.13}$$

**Newton's dynamic equation for the filling time of a capillary**:

The equation that describes the filling time of a capillary can be found by balancing the forces working onto capillary ($\vec{F_c}$, $\vec{F_f}$, and $\vec{F_p}$) [87, 90, 91]. According to the Newton's second law the forces acting on an object equals to the product of the mass and velocity of an object $\sum \vec{F} = \frac{d(m \cdot \vec{v})}{dt}$. Then:

$$\frac{d(m \cdot \vec{v})}{dt} = 2\pi \cdot r \cdot \sigma \cdot \cos\theta - 8 \cdot \pi \cdot \mu \cdot L \cdot \vec{v} + \pi \cdot r^2 \cdot P_p \qquad (B.14)$$

The mass is presented as the product of volume and density, where again volume is expressed as the area of circle multiplied by the length of the capillary and the equation can be found as:

$$\frac{d}{dt}(\pi \cdot r^2 \cdot \rho \cdot L \cdot \vec{v}) = 2 \cdot \pi \cdot r \cdot \sigma \cdot \cos\theta - 8\pi \cdot \mu \cdot L \cdot \vec{v} + \pi \cdot r^2 \cdot P_p \qquad (B.15)$$

Left and right side of equation are divided by $(\pi \cdot \rho \cdot r^2)$, then

$$\frac{d}{dt}(L \cdot \vec{v}) = \frac{2 \cdot \sigma \cdot \cos\theta + r \cdot P_p}{r \cdot \rho} - \frac{8 \cdot \mu}{r^2 \cdot \rho} \cdot L \cdot \vec{v} \qquad (B.16)$$

The velocity of the liquid equal to the first differential of capillary length as a function of time ($\vec{v} = \frac{dL}{dt}$).

$$\frac{d}{dt}(L \cdot \frac{dL}{dt}) + \frac{8 \cdot \mu}{r^2 \cdot \rho} \cdot (L \cdot \frac{dL}{dt}) = \frac{2 \cdot \sigma \cdot \cos\theta + r \cdot P_p}{r \cdot \rho} \qquad (B.17)$$

The product of $(L \cdot \frac{dL}{dt})$ can be substituted by $(\frac{1}{2} \cdot \frac{d(L^2)}{dt})$:

$$\frac{d}{dt}(\frac{1}{2} \cdot \frac{d(L^2)}{dt}) + \frac{8 \cdot \mu}{r^2 \cdot \rho} \cdot (\frac{1}{2} \cdot \frac{d(L^2)}{dt}) = \frac{2 \cdot \sigma \cdot \cos\theta + r \cdot P_p}{r\rho} \qquad (B.18)$$

The equation is multiplied by two and all coefficients are substituted by two general letters $A$ and $B$:

$$\frac{d^2(L^2)}{dt^2} + B \cdot \frac{d(L^2)}{dt} = A \qquad (B.19)$$

where:

$$A = \frac{4\sigma\cos\theta + 2rP_p}{r\rho} \text{ and } B = \frac{8\mu}{r^2\rho} \qquad (B.20)$$

**Units of constants A and B**

$$A = \frac{4\sigma\cos\theta + 2rP_p}{r\rho} \qquad (B.21)$$

$$A = \frac{4\sigma\cos\theta}{r\rho} + \frac{2rP_p}{r\rho} \qquad (B.22)$$

Unit for the left fraction of $A_1$:

$$A_1 = \frac{4\sigma \cos \theta}{r\rho} \tag{B.23}$$

$$\frac{\frac{dyn}{m}}{\frac{m \cdot kg}{m^3}} = \frac{\frac{m \cdot kg}{s^2 \cdot m}}{\frac{kg}{m^2}} = \frac{\frac{kg}{s^2}}{\frac{kg}{m^2}} = \frac{m^2}{s^2} \tag{B.24}$$

Unit for the right fraction of $A_2$:

$$A_2 = \frac{2rP_p}{r\rho} \tag{B.25}$$

$$\frac{m \cdot Pa}{\frac{kg \cdot m}{m^3}} = \frac{\frac{kg \cdot m}{s^2 \cdot m^2}}{\frac{kg}{m^2}} = \frac{\frac{kg}{s^2}}{\frac{kg}{m^2}} = \frac{m^2}{s^2} \tag{B.26}$$

Then, the unit of the constant A is $\frac{m^2}{s^2}$.

Unit for the constant B:

$$B = \frac{8\mu}{r^2\rho} \tag{B.27}$$

$$\frac{Pa \cdot s}{\frac{m^2 \cdot kg}{m^3}} = \frac{\frac{kg \cdot s}{m \cdot s^2}}{\frac{kg}{m}} = \frac{1}{s} \tag{B.28}$$

Then, the unit of the constant B is $\frac{1}{s}$ and the equation is expressed as a second order differential equation in terms of $L$, with respect to time:

$$\frac{d^2(L^2)}{dt^2} + B \cdot \frac{d(L^2)}{dt} = A \tag{B.29}$$

In order to solve this equation we substitute the square of L (coordinate) for $a(t)$:

$$\frac{d^2a}{dt^2} + B\frac{da}{dt} = A \tag{B.30}$$

For example, this equation can be solved using Euler's and Wronskwian's methods [203], when one of solution equals:

$$a_1(t) = \frac{A}{B^2}e^{-Bt} \tag{B.31}$$

then, all solutions equal:

$$a(t) = \frac{A}{B^2}e^{-B \cdot t} + \frac{A}{B} \cdot t - \frac{A}{B^2} \tag{B.32}$$

Coming back to substitution of $L^2 = a$ we find:

$$L^2(t) = \frac{A}{B^2}e^{-B \cdot t} + \frac{A}{B} \cdot t - \frac{A}{B^2} \tag{B.33}$$

And the function $L(t)$ is expressed as follows:

$$L(t) = \sqrt{\frac{A}{B^2}e^{-B\cdot t} + \frac{A}{B}\cdot t - \frac{A}{B^2}} \tag{B.34}$$

Then, the $(1 - e^{-Bt})\frac{A}{B^2}$ part of Equation B.33 tends to zero value due to much greater value of constant $B$ in comparison to constant $A$. Then, Equation B.34 can be simplified to following form:

$$L(t) = \sqrt{\frac{A}{B}t} \tag{B.35}$$

## Calculation of unit of L

And according to shown unit for constants A and B, we find:

$$L(t) = \sqrt{\frac{A}{B}t} \tag{B.36}$$

$$\sqrt{\frac{\frac{m^2}{s^2}}{\frac{1}{s}}\cdot s} = \sqrt{m^2} = m \tag{B.37}$$

## 2. Details of calculations for Chapter 4

## Viscosity calculations:

In order to calculate the viscosity using a filling time equation we take the equation:

$$L^2(t) = \frac{A}{B^2}e^{-B\cdot t} + \frac{A}{B}\cdot t - \frac{A}{B^2} \tag{B.38}$$

Here the exponential is neglected due to the fact, that the $B$ coefficient has a high value and thus the exponential term approaches zero. Then:

$$L^2(t) = \frac{A}{B}\cdot t - \frac{A}{B^2} \tag{B.39}$$

Both sides are multiplied by the square of the $B$ coefficient:

$$L^2(t)\cdot B^2 = A\cdot B\cdot t - A \tag{B.40}$$

This equation is a quadratic function, which for a discriminant greater than zero has two coefficients such as:

$$B = \frac{A\cdot t \pm \sqrt{(A\cdot t)^2 - 4\cdot t\cdot L^2}}{2\cdot L^2} \tag{B.41}$$

Here it is assumed that part of $(A\cdot t)^2$ is much greater that another part of a square root $4\cdot t\cdot L^2$, then the equation is simplified to:

$$B = \frac{A\cdot t}{L^2} \tag{B.42}$$

Then taking the coefficients of $A$ and $B$ as shown in equation B.20 we find a ratio of viscosity to surface tension such as:

$$\frac{\mu}{\sigma} = \frac{t\cdot r}{2\cdot L^2} \tag{B.43}$$

# Appendix to chapter 5

This Appendix demonstrates examples of integrating the hydrogel with a different HC-PCF, than HC-PCF 1060.

The silanisation and photo-initiation processes were performed with identical chemical steps and the same optical tests and optical configurations as for the HC-PCF 1060. The purpose to test other fibres, was to establish the complete filling of the fibre with the hydrogel and characterise the homogenous distribution for a minimum 10 *cm* of the fibre length.



<div align="center">

(a) *New fibre*    (b) *AMPTS filling*    (c) *Cured fibre*    (d) *Eosin Y filling*

(e) *Dried Eosin*    (f) *Eosin Y evidence*    (g) *Water filling*    (h) *Silanised fibre*

</div>

Figure C.1: *The array of cross section portrays of HC-PCF 1550 for a silanisation process*

First, Fig.C.1a presents the cross-section images of HC-PCF 1550 (with the core diameter $d = 10.8 \ \mu m$) during the silanisation process. The chemical surface coverage was controlled in an optical microscope, where an input of the fibre was connected to a syringe setup and output was connected to a microscope. The silanisation begins with filling the fibre with APTMS solution (Fig.C.1b). Due to the presence of a silanising agent, a particular green colour appeared. However in Fig.C.1c for the fibre, which was cured in the oven, cooled down and cleaved, the green colour is not so strong.

However, we can observe some changes at the inner fibre surfaces. Fig.C.1d shows an example of a fully filled fibre, and any air-bubbles are coming out of fibre. Air bubbles had been found to disrupt a uniform surface of APTMS inside capillaries and consequently disrupts hydrogel growth. At the second part of the silanisation, the fibre was refilled with Eosin Y solution. After this filling we can observe a magenta colour in the fibre as is presented in Fig.C.1e. Next, the fibre was left for 90 minutes in this solution, Eosin Y and EDAC dried at the surface of fibre and blocked the output of fibre, as shown in Fig.C.1f. In this case it was necessary to cleave the fibre, and flush the fibre with water. In Fig.C.1f the magenta colour is clearly seen. Probably due to the capillaries size in the fibre or reduced air exposure, the Eosin Y did not dry out inside the fibre. Then, refilling the fibre with water was run without any disturbance and was repeated few times to ensure that all Eosin Y solution is removed. Fig.C.1g shows a cross section of the fibre washed with water. At the last stage of silanisation the fibre was kept in the oven to be dried. At this stage the silanisation process was complete. Fig.C.1h shows an example of the silane HC-PCF 1550 with green uniformly distributed colour in the fibre.



(a) *HC-PCF 800*    (b) *HC-PCF 1550*    (c) *Silanised core*

Figure C.2: *The cross-section of fibre: HC-PCF 1550 and HC-PCF 800 with examples of non-uniform surface coverage, (a,b) in the optical microscope; (c) when only core is silanised*

Fig.C.2 present examples of non-uniform surface coverage for fibres HC-PCF 1550 and HC-PCF 800 (with the core diameter $d = 8.2$ $\mu m$) which were tested using a fluorescence microscope.

Herein examples of the hydrogel grown in the core of fibres: HC-PCF 800 and HC-PCF 1550 are presented. Fig.C.3a shows a cross-section of silanised HC-PCF 800 and Fig.C.3b shows hydrogel grown in the fibre core. Fig.C.3c presents HC-PCF 1550 with hydrogel grown partially in the fibre core. Fig.C.3d illustrates the hydrogel grown in the fibre core and arbitrarily grown in the fibre cladding. The evidence of hydrogel was found only in the first millimeters of the fibre length. Thus it can be concluded that the HC-PCF 800 was presented to be a good candidate to be integrated with the PEGDA hydrogel matrix. The HC-PCF 800 is recommended for further tests for hydrogel

(a) *HC-PCF 800*  (b) *HC-PCF 800*

(c) *HC-PCF 1550*  (d) *HC-PCF 1550*

Figure C.3: *The cross-section of fibre: HC-PCF 800 (a) the silanised fibre, (b) hydrogel in the fibre core, (c) example of hydrogel grown in the core of HC-PCF 1550 and (d) hydrogel evidence in the fibre cladding channels and in the core*

growing process, and equally the HC-PCF 1060.

However HC-PCF 1550 shows poor abilities to grow the hydrogel inside its capillaries. Even though the silanisation was completed and the fibre was found with a good surface coverage. This fibre HC-PCF 1550 should be disqualified in terms of using this fibre with PEGDA hydrogel polymerisation due to observation that the hydrogel is hardly ever grown in the core. This is due to the shifting primary wavelength ($\lambda = 1550$ *nm*) in the filled fibre with the PVT solution to wavelength $\lambda \approx 870$ *nm*. It is assumed that the refractive index of PVT solution is close to 1.33. The shifted wavelength is much longer, than wavelengths required to excite Eosin Y and begin the photo-polymerisation of the hydrogel.

# List of symbols

For the reader's convenience, symbols are re-defined in following lists:

- List of Latin's symbols

  $a$ - acceleration

  $aff$ - air filling fraction

  $A$ - absorbance

  $c$ - speed of light in vacuum

  $C$ - concentration

  $d$ - diameter

  $d_c$ - curvature of corner of the cladding hole

  $d_{sc}$ - width of silica surrounding the core

  $D_c$ - diameter of the core of the fibre

  $D_{cv}$ - inter curvature of corner of the fibre core

  $D'_{cv}$ - outer curvature of corner of the fibre core

  $D_1$ - diameter of the first element

  $D_2$ - diameter of the second element

  $e$ - constant $\approx 2.718$

  $E$ - energy

  $E_{pulse}$ - pulse energy

  $\vec{E}$ - electric field vector

  $f$ - frequency

  $F$ - force

  $F_c$ - capillary force

  $F_f$ - friction force

  $F_p$ - external pressure force

  $f_{pulse}$ - pulse frequency

  $g$ - gravitational constant ($g = 9.81 \ m/s^2$)

  $h$ - height

  $h_r$ - recommended height

  $\vec{H}$ - magnetic field vector

  $I$ - intensity

  $I_0$ - input intensity

  $k_0$ - free space wave number $2\pi/\lambda$)

  $\vec{k}$ - wave vector

  $ln$ - natural logarithm, logarithmic function to the base $e$

$L$ - length

$L_n$ - length for element number $n$

$\Delta L_n$ - length of difference between elements at $n$ point

$L_1$ - length of the first element

$L_2$ - length of the second element

$L_t$ - total length

$m$ - mass

$m_i$ - diffraction pattern order integer

$m_r$ - resonance order integer

$M$ - magnification

$n$ - refractive index

$n_{eff}$ - effective index

$P$ - power

$P_p$ - pressure

$P_{average}$ - average power

$P_{peak}$ - peak power

$r$ - radius

$Re$ - Reynold's number

$Q$ - flow rate

$t$ - time

$T_{pulse}$ - pulse repetition rate

$v$ - velocity

$\times$ - times

$W$ - width

- List of Greek's symbols

$\alpha$ - attenuation coefficient

$\alpha_i$ is an inclination angle

$\beta$ - constant propagation in $z$ direction

$\delta$ - the phase difference of travelling wavelengths

$\Delta t$ - peak width

$\phi$ - molar extinction coefficient

$\lambda$ - wavelength

$\Lambda$ - pitch (lattice spacing)

$\mu$ - absolute viscosity

$\mu_k$ - kinematic viscosity

$\mu_d$ - dynamic viscosity

$(\Delta\mu)$ - error of viscosity

$\pi$ - constant $\approx 3.14$

$\Pi$ - auxiliary constant

$\Psi$ - attenuation

$\rho$ - density

$\sigma$ - surface tension

$\sum$ - sum

$\theta$ - angle

$\omega$ - angular frequency

$\varphi$ - fraction of light, which penetrates the sample

# List of acronyms and synonyms

For the reader's convenience, acronyms and synonyms are re-defined in a following list:

**AF** - alignment filter

**APTMS** - (3-aminopropyl)triethoxysilane

**ARROW** - anti-resonant reflecting optical waveguide

**BBM** - biorthonormal basis method

**BPM** - beam propagation method

**CA** - clear aperture

**DAQ** - analogue to digital converter

**CCD** - charge coupled device

**Cy-3** - cyanine dyes yellow-green

**Cy-5** - cyanine dyes orange-red

**CW** - continuous wave

**DF** - dichroic filter

**DNA** - (nucleic) deoxyribonucleic acid

**EDAC** - N-(3-Dimethylaminopropyl)-N'-ethylcarbodiimide hydrochloride

**Eosin Y** - 2',4',5',7'-Tetrabromofluorescein Acid Red 87 Bromo acid

**Fig** - figure

**FDM** - Fourier decomposition method

**FDTD** - finite difference method

**FEM** - finite element method

**FITC** - fluorescein isothiocyanate

**FL** - focal length

**FWHM** - full width at half maximum

**GVD** - group velocity dispersion

**H** - magnetic

**HC-PCF** - hollow-core photonic crystal fibre

**HNL-PCF** - highly nonlinear photonic crystal fibre

**HR** - high resolution

**IF** - input filter

**IPA** - isopropyl alcohol

**IR** - infra red

**LED** - light emitting diode

**LP** - linearly polarised

**MM** - multimode fibre

**MOF** - microstructure optical fibre

**MPM** - multipole method

**NA**- numerical aperture

**NOA** - norland optical adhensive

**OBJ** - objective

**OF** - output filter

**OD** - optical density

**OT** - optical transmission

**OPTL** - optimum length

**OSA** - optical spectrum analyser

**PBG** - photonic bandgap

**PBS** - phosphate buffered saline

**PD** - photo-diode

**PDB** - pendant double bonds

**pH** - potential hydrogen

**PEG** - polyethylene glycol

**PEGDA** - poly(ethylene glycol) diacrylate

**P3** - suspended-core optical fibre type: P3

**P7** - suspended-core optical fibre type: P7

**PC** - computer

**PCF** - photonic crystal fibre

**PVT** - PEG/VP/TEOA solution

**PWM** - plane wave method

**QBP** - quaternary branch point

**SC** - supercontinuum

**SEM** - scanning electron microscope

**SM** - spectrometer

**SOP** - standard optical fibre

**TEOA** - tetraethylammonium chloride

**TIR** - total index-reflection

**VIS** - visible range

**VP** - 1-vinyl-2-pyrrolidinone

**WD** - working distance

# References

[1] T. Birks, P. Roberts, P. Russell, D. Atkin, and T. Shepherd, "Full 2-d photonic bandgaps in silica/air structures," *Electronics Letters*, vol. 31, no. 22, pp. 1941–1942, 1995.

[2] M. Grogan, S. Leon-Saval, R. England, and T. Birks, "Silica aerogel core waveguide," *Optics Express*, vol. 18, no. 21, pp. 22497–22502, 2010.

[3] T. Larsen, A. Bjarklev, D. Hermann, and J. Broeng, "Optical devices based on liquid crystal photonic bandgap fibres," *Optics Express*, vol. 11, no. 20, pp. 2589–2596, 2003.

[4] L. Scolari, S. Gauza, H. Xianyu, L. Zhai, L. Eskildsen, T. Alkeskjold, S. Wu, and A. Bjarklev, "Frequency tunability of solid-core photonic crystal fibers filled with nanoparticle-doped liquid crystals," *Optics Express*, vol. 17, no. 5, pp. 3754–3764, 2009.

[5] O. Frazao, J. Santos, F. Araujo, and L. Ferreira, "Optical sensing with photonic crystal fibers," *Laser and Photonics Reviews*, vol. 2, no. 6, pp. 449–459, 2008.

[6] M. Petrovich, A. van Brakel, F. Poletti, K. Mukasa, E. Austin, V. Finazzi, P. Petropoulos, E. O'Driscoll, M. Watson, T. DelMonte, T. Monro, J. Dakin, and D. Richardson, "Microstructured fibres for sensing applications," *Proceedings of SPIE, Conference on Photonic Crystal Fibers for Sensing Applications*, vol. 6005, no. 60050E, pp. 1–15, 2005.

[7] R. Cregan, B. Mangan, J. Knight, T. Birks, P. Russell, P. Roberts, and D. Allan, "Single-mode photonic band gap guidance of light in air," *Science*, vol. 285, pp. 1537–1539, 1999.

[8] J. Knight, "Photonic crystal fibres," *Nature*, vol. 424, no. 6950, pp. 847–851, 2003.

[9] J. Knight, T. Birks, P. Russell, and D. Atkin, "All-silica single-mode optical fiber with photonic crystal cladding: errata," *Optics Letters*, vol. 22, no. 7, pp. 484–485, 1997.

[10] P. Russell, "Photonic crystal fibers," *Science Review Applied Physics*, vol. 299, pp. 358–362, 2003.

[11] J. Jones, P. Russell, J. Knight, and T. Birks, "Photonic crystal fibres for sensors applications," *Proceedings of IEEE, Conference on 19th Optical Fiber Sensors (OFS)*, vol. FB1, pp. 565–568, 2002.

[12] J. Jensen, L. Pedersen, P. Hoiby, L. Nielsen, T. Hansen, J. Folkenberg, J. Riishede, D. Noordegraaf, K. Nielsen, A. Carlsen, and A. Bjarklev, "Photonic crystal fiber based evanescent-wave sensor for detection of biomolecules in aqueous solutions," *Optics Letters*, vol. 29, no. 17, pp. 1974–1976, 2004.

[13] F. Benabid, "Hollow-core photonic bandgap fibre: new light guidance for new science and technology," *Philosophical Transactions of the Royal Society A: Mathematical, Physical and Engineering Sciences*, vol. 364, no. 1849, pp. 3439–3462, 2006.

[14] G. Chunying and Y. Libo, "Analysis of the characteristics of photonic crystal fibers used in liquid sensors," *Proceedings of SPIE, International Conference on Smart Materials and Nanotechnology in Engineering*, vol. 6423, no. 64234Y, pp. 1–6, 2007.

[15] C. Cordeiro, C. de Matos, E. dos Santos, A. Bozolan, J. Ong, T. Facincani, G. Chesini, A. Vaz, and C. Brito-Cruz, "Towards practical liquid and gas sensing with photonic crystal fibres: side access to the fibre microstructure and single-mode liquid-core fibre," *Measurement Science and Technology*, vol. 18, pp. 3075–3081, 2007.

[16] F. Cox, A. Argyros, and M. Large, "Liquid-filled hollow core microstructured polymer optical fiber," *Optics Express*, vol. 14, pp. 4135–4140, 2006.

[17] J. Fini, "Microstructure fibres for optical sensing in gases and liquids," *Measurement Science and Technology*, vol. 15, pp. 1120–1128, 2004.

[18] T. Monro, W. Belardi, K. Furusawa, J. Baggett, N. Broderick, and D. Richardson, "Sensing with microstructured optical fibres," *Measurement Science and Technology*, vol. 12, pp. 854–858, 2001.

[19] J. Chen, T. Euser, N. Farrer, P. Sadler, and P. Russell, "Photochemistry in photonic crystal fibers," *Proceedings of IEEE, European Conference on Lasers and Electro-Optics and the European Quantum Electronics Conference CLEO - EQEC Europe 2009*, 2009.

[20] C. Cordeiro, E. dos Santos, C. Brito-Cruz, C. de Matos, and D. Ferreiira, "Lateral access to the holes of photonic crystal fibers-selective filling and sensing applications," *Optics Express*, vol. 14, no. 18, pp. 8403–8412, 2006.

[21] A. Duval, M. Lhoutellier, J. Jensen, P. Hoiby, V. Missier, L. Pedersen, T. Hansen, A. Bjarklev, and O. Bang, "Photonic crystal fiber based antibody detection," *Proceedings of IEEE, Sensors*, vol. 3, pp. 1222–1225, 2004.

[22] G. Emiliyanov, J. Jensen, O. Bang, P. Hoiby, L. Pedersen, E. Kjaer, and L. Lindvold, "Localized biosensing with topas microstructured polymer optical fiber," *Optics Letters*, vol. 32, no. 5, pp. 460–462, 2007.

[23] J. Jensen, P. Hoiby, G. Emiliyanov, O. Bang, L. Pedersen, and A. Bjarklev, "Selective detection of antibodies in microstructured polymer optical fibers," *Optics Express*, vol. 13, no. 15, pp. 5883–5889, 2005.

[24] C. D. Matos, C. Cordeiro, E. dos Santos, J. Ong, A. Bozolan, and C. B. Cruz., "Liquid-core, liquid-cladding photonic crystal fibers," *Optics Express*, vol. 15, no. 18, pp. 11207–11212, 2007.

[25] T. Monro, S. Warren-Smith, E. Schartner, A. Franois, S. Heng, H. Ebendorff-Heidepriem, and S. A. V, "Sensing with suspended-core optical fibers," *Optical Fiber Technology*, vol. 16, no. 6, pp. 343–356, 2010.

[26] M. Myaing, J. Ye, T. Norris, T. Thomas, J. Baker, W. Wadsworth, G. Bouwmans, J. Knight, and P. Russell, "Enhanced two-photon biosensing with double-clad photonic crystal fibers," *Optics Letters*, vol. 28, no. 14, pp. 1224–1226, 2003.

[27] M. Naji, A. Khetani, N. Lagali, R. Munger, and H. Anis, "A novel method of using hollow-core photonic crystal fiber as a raman biosensor," *Proceedings of SPIE, Conference on Nanoscale Imaging, Sensing and Actuation for Biomedical Applications*, vol. 6865, pp. 68650E(1–8), 2008.

[28] C. Rosberg, F. Bennet, D. Neshev, P. Rasmussen, O. Bang, W. Krolikowski, A. Bjarklev, and Y. S. Kivshar, "Tunable diffraction and self-defocusing in liquid-filled photonic crystal fibers," *Optics Express*, vol. 15, no. 19, pp. 12145–12150, 2007.

[29] Y. Ruan, T. C. Foo, S. Warren-Smith, P. Hoffmann, R. Moore, H. Ebendorff-Heidepriem, and T. Monro, "Antibody immobilization within glass microstructured fibers: a route to sensitive and selective biosensors," *Optics Express*, vol. 16, no. 22, pp. 18514–18523, 2008.

[30] M. Rutowska, L.Horan, and F. G. Gunning, "Photonic crystal fibres: Selective fillings delays," *Proceedings of IEEE, European Conference on Lasers and Electro-Optics and the European Quantum Electronics Conference (CLEO - EQEC Europe)*, vol. CH3, 2009.

[31] E. Schartner, H. Ebendorff-Heidepriem, and T. Monro, "Low concentration fluorescence sensing in suspended-core fibers," *Proceedings of SPIE, 21st International Conference on Optical Fibers Sensors,*, vol. 7753, pp. 77534Q–(1–4), 2011.

[32] N. Churayev, V. Sobolev, and Z. Zorin, "Measurement of viscosity of liquids in quartz capillaries," *Special Discussions of the Faraday Society*, vol. 1, pp. 213–220h, 1970.

[33] I. Bloomfield, I. Johnston, and L. Bilston, "Effects of proteins, blood cells and glucose on the viscosity of cerebrospinal fluid," *Pediatric Neurosurgery*, vol. 28, no. 5, pp. 246–251, 1998.

[34] A. Sharma, R. Khanna, and G. Reiter, "A thin film analog of the corneal mucus layer of the tearfilm: an enigmatic long range non-classical ( dlvo) interaction in the breakup of thin polymer films.," *Colloids and Surfaces B: Biointerfaces*, vol. 14, pp. 223–235, 1999.

[35] G. Boas, "Measuring viscosity with fluorescence lifetime imaging," *Biophotonics International*, vol. 07, pp. 46–47, 2008.

[36] P. Wilding, J. Pfahler, H. Bau, J. Zemel, and L. Kricka, "Manipulation and flow of biological fluids in straight channels micromachined in silicon," *Clinical Chemistry*, vol. 40, no. 1, pp. 43–47, 1994.

[37] K. Yeleswarapu, M. Kameneva, K. Rajagopal, and J. Antaki, "The flow of blood in tubes: theory and experiment," *Mechanics Research Communications*, vol. 25, no. 3, pp. 257–262, 1998.

[38] R. Fahraeus and T. Lindqvist, "The viscosity of the blood in narrow capillary tubes," *American Journal of Physiology*, vol. 96, no. 3, pp. 562–568, 1931.

[39] G. Pop, D. Duncker, M. Gardien, P. Vranckx, S. Versluis, D. Hasan, and C. Slager, "The clinical significance of whole blood viscosity in (cardio)vascular medicine.," *Netherlands Heart Journal*, vol. 10, no. 12, pp. 512–516, 2002.

[40] A. Bron, J. Tiffany, S. Gouveia, N. Yokoi, and L. Voon, "Functional aspects of the tear film lipid layer," *Experimental Eye Research*, vol. 78, pp. 347–360, 2004.

[41] M. Rolando and M. Zierhut, "The ocular surface and tear film and their dysfunction in dry eye disease," *Survey of Ophthalmology*, vol. 45, no. 2, pp. s203–s210, 2001.

[42] J. Smith, H. Irving, and R. Simpson, "An automatic capillary viscometer," *Analyst*, vol. 95, pp. 743–750, 1970.

[43] E. Washburn, "The dynamics of capillary flow," *The Physical Review*, vol. XVII, no. 3, pp. 273–283, 1921.

[44] M. Rutowska, L. Horan, G. Khara, and F. G. Gunning, "Nano-litre fibre viscometer device, university college cork , national university of ireland, uk 1104547.3," March 2012.

[45] F. Kivlehan, M. Paolucci, J. Ragoussis, and P. Galvin, "The fabrication of 3d hydrogel structures by photo-polymerization for the detection of specific dna sequences," *Manuscript in preparation*.

[46] M. Rutowska, P. Galvin, and F. G. Gunning, "Optical properties of hydrogel-filled hollow core photonic crystal fibres," *Proceedings of SPIE, Fourth European Workshop on Optical Fiber Sensors*, vol. 7653, pp. 76531P–4, 2010.

[47] P. Charles, E. Goldman, J. Rangasammy, C. Schauer, M. Chen, and C. Taitt, "Fabrication and characterization of 3d hydrogel microarrays to measure antigenicity and antibody functionality for biosensor applications," *Biosensors and Bioelectronics*, vol. 20, no. 4, pp. 753–764, 2004.

[48] V. Lin, K. Motesharei, K. Dancil, M. Sailor, and M. Ghadiri, "A porous silicon-based optical interferometric biosensor," *Science*, vol. 278, no. 5339, pp. 840–843, 1997.

[49] G. Yershov, V. Barsky, A. Belgovskiy, E. Kirillov, E. Kreindlin, I. Ivanov, S. Parinov, D. Guschin, A. Drobishev, S. Dubiley, and A. Mirzabekov, "Dna analysis and diagnostics on oligonucleotide microchips," *Proceedings of the National Academy of Sciences of the United States of America*, vol. 93, no. 10, pp. 4913–4918, 1996.

[50] G. Cruise, O. Hegre, D. Scharp, and J. Hubbell, "A sensitivity study of the key parameters in the interfacial photopolymerization of poly(ethylene glycol) diacrylate upon porcine islets," *Biotechnology and Bioengineering*, vol. 57, no. 6, pp. 655–665, 1998.

## References

[51] A. Hoffman, "Hydrogels for biomedical applications," *Advanced Drug Delivery Reviews*, vol. 54, no. 0169-409X, pp. 3–12, 2002.

[52] E. Moore, D. O'Connell, and P.Galvin, "Surface characterisation of indium-tin oxide thin electrode films for use as a conducting substrate in dna sensor development," *Thin Solid Films*, vol. 515, no. 4, pp. 2612–2617, 2006.

[53] J. Savage, "Materials for infrared fibre optics," *Materials Science Reports*, vol. 2, no. 3, pp. 99–137, 1987.

[54] X. Jiang, T. Euser, A. Abdolvand, F. Babic, N. Joly, and P. Russell, "Sf6 glass hollow-core photonic crystal fibre," *Proceedings of IEEE, European Conference on Lasers and Electro-Optics and the European Quantum Electronics Conference (CLEO - EQEC Europe)*, vol. CE 4.2 WED, 2011.

[55] T. Monro, D. Richardson, N. Broderick, and P. Bennett, "Holey optical fibers: An efficient modal model," *Journal of Lightwave Technology*, vol. 17, no. 6, pp. 1093–1102, 1999.

[56] A. Bjarklev, J. Broeng, and A. Bjarklev, *Photonic Crystal Fibers*. Kluwer Academic Publishers, 2003.

[57] G. Bouwmans, L. Bigot, Y. Quiquempois, F. Lopez, L. Provino, and M. Douay, "Fabrication and characterization of an all-solid 2d photonic bandgap fiber with a low-loss region (less than 20 db/km) around 1550 nm," *Optics Express*, vol. 13, no. 21, pp. 8452–8459, 2005.

[58] N. Mortensen and M. Nielsen, "Modeling of realistic cladding structures for air-core photonic bandgap fibers," *Optics Letters*, vol. 29, no. 4, pp. 349–351, 2004.

[59] J. Lyngso, C. Jakobsen, H. Simonsen, and J. Broeng, "Single-mode 7-cell hollow core photonic crystal fiber with increased bandwidth," *Proceedings of SPIE, 21th International Conference on Optical Fibers Sensors*, vol. 7753, p. 77533Q, 2011.

[60] N. Litchinitser, A. Abeeluck, C. Headley, and B. Eggleton, "Anitiresonant reflecting photonic crystal optical waveguides," *Optics Letters*, vol. 27, no. 18, pp. 1592–1594, 2002.

[61] D. Meschede, *Optics, Light and Lasers*. Wiley Subscription Services, Inc., A Wiley Company, 2004.

[62] F. Gerome, R. Jamier, J. Auguste, G. Humbert, and J. Blondy, "Simplified hollow-core photonic crystal fiber," *Optics Letters*, vol. 35, no. 8, pp. 1157–1159, 2010.

[63] P. Roberts, D. Williams, B. Mangan, H. Sabert, F. Couny, W. Wadsworth, T. Birks, J. Knight, and P. Russell, "Realizing low loss air core photonic crystal fibers by exploiting an antiresonant core surround," *Optics Express*, vol. 13, no. 20, pp. 8277–8285, 2005.

[64] A. Argyros, S. Leon-Saval, J. Pla, and A. Docherty, "Antiresonant reflection and inhibited coupling in hollow-core square lattice optical fibres," *Optics Express*, vol. 16, no. 8, pp. 5642–5648, 2008.

[65] A. Argyros, T. Birks, S. Leon-Saval, C. Cordeiro, F. Luan, and P. Russell, "Photonic bandgap with an index step of one percent," *Optics Express*, vol. 13, no. 1, pp. 309–314, 2005.

[66] N. Litchinitser, S. Dunn, B. Usner, B. Eggleton, T. White, R. McPhedran, and C. de Sterke, "Resonances in microstructured optical waveguides," *Optics Express*, vol. 11, no. 10, pp. 1243–1251, 2003.

[67] T. White, R. McPhedran, C. M. de Sterke, N. Lichinitser, and B. Eggleton, "Resonance and scattering in microstructured optical fibers," *Optics Letters*, vol. 27, no. 22, pp. 1977–1979, 2002.

[68] J. Knight, J.Broeng, T. Birks, and P. Russell, "Photonic band gap guidance in optical fibres," *Science*, vol. 282, pp. 1476–1478, 1998.

[69] G. Pearce, J. Pottage, D. Bird, P. Roberts, J. Knight, and P. Russell, "Hollow-core photonic crystal fiber for guidance in the mid to far infra-red," *Optics Express*, vol. 13, no. 18, pp. 6937–6946, 2005.

[70] G. Renversez, P. Boyer, and A. Sagrini, "Antiresonant reflecting optical waveguide microstructured fibers revisited a new analysis based on leaky mode coupling," *Optics Express*, vol. 14, no. 12, pp. 5682–5686, 2006.

[71] G. Agrawal, *Nonlinear fiber optics*. Elsevier, Academic Press, 2007.

[72] J. Joannopoulos, S. Johnson, J. Winn, and R. Meade, *Photonic Crystals: Molding the flow of light*. Princeton University Press, 2008.

[73] F. Couny, P. Roberts, T. Birks, and F. Benabid, "Square-lattice large pitch hollow-core photonic crystal fiber," *Optics Express*, vol. 16, no. 25, pp. 20626–20636, 2008.

[74] E. Yablonovitch, "Photonic band-gap structures," *Journal of the Optical Society of America B*, vol. 10, no. 2, pp. 283–295, 1993.

[75] C. Kittel, *Introduction to Solid State Physics 4th Edition*. John Wiley & Sons, Inc., 1971.

[76] K. Leung and Y. Liu, "Full vector wave calculation of photonic band structures in face-centered-cubic dielectric media," *Physical Review Letters*, vol. 65, no. 21, pp. 2646–2649, 1990.

[77] K. Saitoh, N. Mortensen, and M. Koshiba, "Air-core photonic band-gap fibers: the impact of surface modes," *Optics Express*, vol. 12, no. 3, pp. 394–400, 2004.

[78] F. Benabid and P. Roberts, "Guidance mechanisms in hollow-core photonic crystal fiber," *Proceedings of SPIE, Conferrence on Photonic Crystal Materials and Devices VII*, vol. 6901, p. 69010U, 2008.

[79] F. Luan, A. George, T. Hedley, G. Pearce, D. Bird, J. Knight, and P. Russell, "All-solid photonic bandgap fiber," *Optics Letters*, vol. 29, no. 20, pp. 2369–2371, 2004.

[80] D. Mogilevtsev, T. Birks, and P. Russell, "Localized function method for modeling defect modes in 2d photonic crystals," *Journal of Lightwave Technology*, vol. 17, no. 11, pp. 2078–2081, 1999.

[81] N. Mortensen, M. Nielsen, J. Folkenberg, C. Jakobsen, and H. Simonsen, "Photonic crystal fiber with a hybrid honeycomb cladding," *Optics Express*, vol. 12, no. 3, pp. 468–472, 2004.

[82] T. Birks, D. Bird, T. Hedley, J. Pottage, and P. Russell, "Scaling laws and vector effects in bandgap-guiding fibres," *Optics Express*, vol. 12, no. 1, pp. 69–74, 2004.

[83] G. Antonopoulos, F. Benabid, D. Bird, J. Knight, and P. Russell, "Experimental demonstration of the frequency shift of bandgaps in photonic crystal fibers due to refractive index scaling," *Optics Express*, vol. 14, no. 7, pp. 3000–3006, 2006.

[84] J. Fini, "Water-core microstructure fiber for optical sensing," *Proceedings of IEEE, Conference on Optical Fiber Communication*, p. MF3, 2004.

[85] P. Prasad, *Introduction to Biophotonics*. John Wiley & Sons, Inc., 2003.

[86] G. Hale and M. Querry, "Optical constants of water in the 200-nm to 200-um wavelength region," *Applied Optics*, vol. 12, no. 3, pp. 555–563, 1973.

[87] K. Nielsen, D. Noordegraaf, T. Sorensen, A. Bjarklev, and T. Hansen, "Selective filling of photonic crystal fibres," *Journal of Optics A: Pure and Applied Optics*, vol. 7, no. 8, pp. L13–L20, 2005.

[88] F. Tiberg, B. Zhmud, K. Hallstensson, and M. von Bahr, "Capillary rise of surfactant solutions," *Physical Chemistry Chemical Physics*, vol. 2, pp. 5189–5196, 2000.

[89] C. Crowe, D. Eiger, and J. Roberson, *Engineering Fluid Mechanics*. John Wiley & Sons, Inc., 2005.

[90] B. Zhmud, F. Tiberg, and K. Hallstensson, "Dynamics of capillary rise," *Journal of Colloid and Interface Science*, vol. 228, pp. 263–269, 2000.

[91] F. White, *Viscous Fluid Flow 2nd edition*. New York: McGraw-Hill Education, 1991.

[92] V. Sobolev, N. Churayev, M. Velarde, and Z. Zorin, "Surface tension and dynamic contact angle of water in thin quartz capillaries," *Journal of Colloid and Interface Science*, vol. 222, pp. 51–54, 2000.

[93] R. Finn, "The contact angle in capillarity," *Physics of Fluids*, vol. 18, no. 047102, pp. 1–7, 2006.

[94] R. Glaser, *Biophysics*. Springer Netherlands, 1999.

[95] W. Smith and P. Foote, "Capillary phenomena in non-circular cylindrical tubes," *Industrial and Engineering Chemistry*, vol. 21, pp. 567–568, 1929.

[96] M. D. Nielsen and N. A. Mortensen, "Photonic crystal fiber design based on the v-parameter," *Optics Express*, vol. 11, no. 21, pp. 2762–2768, 2003.

[97] W. Mizerski, *Tablice matematyczno-fizyczno-astronomiczno-chemiczne 2nd edition*. Wydawnictwo Adamantan, 1997.

[98] J. Kestin, M. Sokolov, and W. Wakeham, "Viscosity of liquid water in the range -8 to 150 (celcius degree)," *Journal of Physical and Chemical Reference Data*, vol. 7, no. 3, pp. 941–947, 1978.

[99] J. Kopecek, "Hydrogels: From soft contact lenses and implants to self-assembled nanomaterials," *Journal of Polymer Science Part A: Polymer Chemistry*, vol. 47, pp. 5929–5946, 2009.

[100] G. Bardajee, A. Pourjavadi, and R. Soleyman, "Novel highly swelling nanoporous hydrogel based on polysaccharide/protein hybrid backbone," *Journal of Polymer Research*, vol. 18, pp. 337–346, 2011.

[101] J. He, Y. Du, J. Villa-Uribe, C. Hwang, D. Li, and A. Khademhosseini, "Rapid generation of biologically relevant hydrogels containing long-range chemical gradients," *Advanced Functional Materials*, vol. 20, no. 1, pp. 131–137, 2010.

[102] K. Lee and D. Mooney, "Hydrogels for tissue engineering," *Chemical Reviews*, vol. 101, no. 0009-2665, pp. 1869–1880, 2001.

[103] C. Schwarz, V. Klein, G. Davidson, J. Graham, M. Ruth, F. McDonald, F. McGauran, A. Seaton, and H. Sargeant, eds., *Chambers Concise Dictionary*. R & W Chambers Ltd., 1991.

[104] A. Revzin, R. Russell, V. Yadavalli, W. Koh, C. Deister, D. Hile, M. Mellott, and M. Pishko, "Fabrication of poly(ethylene glycol) hydrogel microstructures using photolithography," *Langmuir*, vol. 17, no. 18, pp. 5440–5447, 2001.

[105] S. Foulger, P. Jiang, A. Lattam, D. Smith, and J. Ballato, "Mechanochromic response of poly(ethylene glycol) methacrylate hydrogel encapsulated crystalline colloidal arrays," *Langmuir*, vol. 17, no. 19, pp. 6023–6026, 2001.

[106] M. Byrne, K. Park, and N. Peppas, "Molecular imprinting within hydrogels," *Advanced Drug Delivery Reviews*, vol. 54, pp. 149–161, 2002.

[107] M. Byrne and V. Salian, "Molecular imprinting within hydrogels ii: Progress and analysis of the field," *International Journal of Pharmaceutics*, vol. 364, no. 0378-5173, pp. 188–212, 2008.

[108] J. Chen, H. Park, and K. Park, "Synthesis of superporous hydrogels: Hydrogels with fast swelling and superabsorbent properties," *Journal of Biomedical Materials Research*, vol. 44, no. 1, pp. 53–62, 1999.

[109] V. Dyukova, E. Dementieva, D. Zubtsov, O. Galanina, N. Bovin, and A. Rubina, "Hydrogel glycan microarrays," *Analytical Biochemistry*, vol. 347, pp. 94–105, 2005.

[110] A. Koponen, M. Kataja, and J. Timonen, "Tortuous flow in porous media," *Physical Review E*, vol. 54, no. 1, pp. 406–410, 1996.

[111] N. Padmavathi and P. Chatterji, "Structural characteristics and swelling behavior of poly(ethylene glycol) diacrylate hydrogels," *Macromolecules*, vol. 29, no. 6, pp. 1976–1979, 1996.

[112] M. Pradny, P. Lesny, K. Smetana, J. Vacik, M. Slouf, J. Michalek, and E. Sykova, "Macroporous hydrogels based on 2-hydroxyethyl methacrylate," *Journal of Materials Science: Materials in Medicine*, vol. 16, pp. 767–773, 2005.

[113] R. Kishi, H. Kihara, T. Miura, and H. Ichijo, "Microporous poly(vinyl methyl ether) hydrogels prepared by gamma-ray irradiation at different heating rates," *Radiation Physics and Chemistry*, vol. 72, no. 0969-806X, pp. 679–685, 2005.

[114] R. Taribagil, M. Hillmyer, and T. Lodge, "Hydrogels from aba and abc triblock polymers," *Macromolecules*, vol. 43, no. 12, pp. 5396–5404, 2010.

[115] H. Lee, D. Kim, S. Park, Y. Lee, and W. Koh, "Micropatterning of a nanoporous alumina membrane with poly(ethylene glycol) hydrogel to create cellular micropatterns on nanotopographic substrates," *Acta Biomaterialia*, vol. 7, no. 3, pp. 1281–1289, 2011.

[116] J. Ehrick, S. Deo, T. Browning, L. B. M. Madou, and S. Daunert, "Genetically engineered protein in hydrogels tailors stimuli-responsive characteristics," *Nature Materials*, vol. 4, no. 4, pp. 298–302, 2005.

[117] S. Bryant, T. Chowdhury, D. Lee, D. Bader, and K. Anseth, "Crosslinking density influences chondrocyte metabolism in dynamically loaded photocrosslinked poly(ethylene glycol) hydrogels," *Annals of Biomedical Engineering*, vol. 32, pp. 407–417, 2004.

[118] M. Mellott, K. Searcy, and M. Pishko, "Release of protein from highly cross-linked hydrogels of poly(ethylene glycol) diacrylate fabricated by uv polymerization," *Biomaterials*, vol. 22, no. 0142-9612, pp. 929–941, 2001.

[119] K. Nguyen and J. West, "Photopolymerizable hydrogels for tissue engineering applications," *Biomaterials*, vol. 23, no. 0142-9612, pp. 4307–4314, 2002.

[120] A. Sawhney, C. Pathak, and J. Hubbell, "Bioerodible hydrogels based on photopolymerized poly(ethylene glycol)-co-poly(alpha-hydroxy acid) diacrylate macromers," *Macromolecules*, vol. 26, pp. 581–587, 1993.

[121] S. Kizilel, "Mathematical model for microencapsulation of pancreatic islets within a biofunctional pegda hydrogel," *Macromolecular Theory and Simulations*, vol. 19, no. 8-9, pp. 514–531, 2010.

[122] S. Kizilel, V. Perez-Luna, and F. Teymour, "Photopolymerization of poly(ethylene glycol) diacrylate on eosin-functionalized surfaces," *Langmuir*, vol. 20, no. 20, pp. 8652–8658, 2004.

[123] S. Kizilel, V. Perez-Luna, and F. Teymour, "Mathematical model for surface-initiated photopolymerization of poly(ethylene glycol) diacrylate," *Macromolecular Theory and Simulations*, vol. 15, no. 9, pp. 686–700, 2006.

[124] S. Kizilel, V. Perez-Luna, and F. Teymour, "Modeling of pegda hydrogel membranes for biomedical applications," *Macromolecular Reaction Engineering*, vol. 3, no. 5-6, pp. 271–287, 2009.

[125] S. Kizilel, E. Sawardecker, F. Teymour, and V. Perez-Luna, "Sequential formation of covalently bound hydrogel multilayers through surface initiated photopolymerization," *Biomaterials*, vol. 27, no. 8, pp. 1209–1215, 2006.

[126] Z. Sun, V. Nicolosi, S. Bergin, and J. Coleman, "Efficient dispersion and exfoliation of single-walled nanotubes in 3-aminopropyltriethoxysilane and its derivatives," *Nanotechnology*, vol. 19, no. 485702, pp. 1–9, 2008.

[127] E. Schulman and C. Walling, "Triplet-state phosphorescence of adsorbed ionic organic molecules at room temperature," *The Journal of Physical Chemistry*, vol. 77, no. 7, pp. 902–905, 1973.

[128] G. Cruise, D. Scharp, and J. Hubbell, "Characterization of permeability and network structure of interfacially photopolymerized poly(ethylene glycol) diacrylate hydrogels," *Biomaterials*, vol. 19, no. 14, pp. 1287–1294, 1998.

[129] R. Brewster and W. McEwen, *Podstawy Chemii Organicznej - Organic Chemistry*. Panstwowe Wydawnictwo Naukowe PWN, 1967.

[130] R. W. Bauman, *Microbiology*. Pearson Eductation Inc., 2004.

[131] J. Lichtman and J. Conchello, "Fluorescence microscopy," *Nature Methods*, vol. 2, no. 12, pp. 910–919, 2005.

[132] J. Berlier, A. Rothe, G. Buller, J. Bradford, D. Gray, B. Filanoski, W. Telford, S. Yue, J. Liu, C. Cheung, W. Chang, J. Hirsch, J. Beechem, R. Haugland, and R. Haugland, "Quantitative comparison of long-wavelength alexa fluor dyes to cy dyes: Fluorescence of the dyes and their bioconjugates," *The Journal of Histochemistry and Cytochemistry*, vol. 51, no. 12, pp. 1699–1712, 2003.

[133] T. Birks, G. Pearce, and D. Bird, "Approximate band structure calculation for photonic bandgap fibres," *Optics Express*, vol. 14, no. 20, pp. 9483–9490, 2006.

[134] A. Ferrando, E. Silvestre, J. Miret, P. Andres, and M. Andres, "Full-vector analysis of a realistic photonic crystal fiber," *Optics Letters*, vol. 24, no. 5, pp. 276–278, 1999.

[135] J. Lee, D. Sun, and Z. Cendes, "Full-wave analysis of dielectric waveguides using tangential vector finite elements," *IEEE Transactions on Microwave Theory and Techniques*, vol. 39, no. 8, pp. 1262–1271, 1991.

[136] F. Brechet, J. Marcou, D. Pagnoux, and P. Roy, "Complete analysis of the characteristics of propagation into photonic crystal fibers, by the finite element method," *Optical Fiber Technology*, vol. 6, no. 2, pp. 181–191, 2000.

[137] R. Amezcua-Correa, N. Broderick, M. Petrovich, F. Polett, and D. Richardson, "Optimizing the usable bandwidth and loss through core design in realistic hollow-core photonic bandgap fibers," *Optics Express*, vol. 14, no. 17, pp. 7974–7985, 2006.

[138] F. Poletti, N. Broderick, D. Richardson, and T. Monro, "The effect of core asymmetries on the polarization properties of hollow core photonic bandgap fibers," *Optics Express*, vol. 13, pp. 9115–9124, 2005.

[139] P. Roberts, F. Couny, H. Sabert, B. Mangan, D. Williams, L. Farr, M. Mason, A. Tomlinson, T. Birks, J. Knight, and P. Russell, "Ultimate low loss of hollow-core photonic crystal fibres," *Optics Express*, vol. 13, no. 1, pp. 236–244, 2005.

[140] C. Smith, N. Venkataraman, M. Gallagher, D. Muller, J. West, N. Borrelli, D. Allan, and K. Koch, "Low-loss hollow-core silica/air photonic bandgap fibre," *Nature*, vol. 424, no. 6949, pp. 657–659, 2003.

[141] P. Roberts, D. Williams, H. Sabert, B. Mangan, D. Bird, T. Birks, J. Knight, and P. Russell, "Design of low-loss and highly birefringent hollow-core photonic crystal fiber," *Optics Express*, vol. 14, no. 16, pp. 7329–7341, 2006.

[142] R. Amezcua-Correa, N. Broderick, M. Petrovich, F. Poletti, D. Richardson, V. Finazzi, and T. Monro, "Realistic designs of silica hollow-core photonic bandgap fibers free of surface modes," *Proceedings of IEEE, Conference on Optical Fibre Communication (OFC)*, p. OFC1, 2005.

[143] L. Xiao, W. Jin, and M. Demokan, "Photonic crystal fibers confining light by both index-guiding and bandgap-guiding: hybrid pcfs," *Optics Express*, vol. 15, no. 24, pp. 15637–15647, 2007.

[144] R. Ramaswani and K. Sivarajan, *Optical Networks: A practical perspective*. Academic Press, 1998.

[145] J. Senior, *Optical Fiber Communication: Principles and Practice*. Pearson Eductation Ltd, Prentice Hall Europe, 1992.

[146] J. Broeng, S. Barkou, T. Sondergaard, and A. Bjarklev, "Analysis of air-guiding photonic bandgap fibers," *Optics Letters*, vol. 25, no. 2, pp. 96–98, 2000.

[147] G. Bouwmans, F. Luan, J. Knight, P. Russell, L. Farr, B. Mangan, and H. Sabert, "Properties of a hollow-core photonic bandgap fiber at 850 nm wavelength," *Optics Express*, vol. 11, no. 14, pp. 1613–1620, 2003.

[148] K. Saitoh, N. Florous, T. Murao, and M. Koshiba, "Design of photonic band gap fibers with suppressed higher-order modes: Towards the development of effectively single mode large hollow-core fiber platforms," *Optics Express*, vol. 14, no. 16, pp. 7342–7352, 2006.

[149] T. Euser, G. Whyte, M. Scharrer, J. Chen, A. Abdolvand, J. Nold, C. Kaminski, and P. Russell, "Dynamic control of higher-order modes in hollow-core photonic crystal fibers," *Optics Express*, vol. 16, no. 22, pp. 17972–17981, 2008.

[150] H. K. Kim, M. Digonnet, G. Kino, J. Shin, and S. Fan, "Simulations of the effect of the core ring on surface and air-core modes in photonic bandgap fibers," *Optics Express*, vol. 12, no. 15, pp. 3436–3442, 2004.

[151] M. Hu, C. Wang, Y. Song, Y. Li, and L. Chai, "A hollow beam from a holey fiber," *Optics Express*, vol. 14, no. 9, pp. 4128–4134, 2006.

[152] J. Hermann, U. Griebner, N. Zhavoronkov, A. Husakou, D. Nickel, J. Knight, W. Wadsworth, P. Russell, and G. Korn, "Experimental evidence for supercontinuum generation by fission of higher-order solitons in photonic fibers," *Physical Review Letters*, vol. 88, no. 17, pp. 173901–(1–4), 2002.

[153] A. Husakou and J. Hermann, "Supercontinuum generation of higher-order solitions by fission in photonic crystal fibres," *Physical Review Letters*, vol. 87, no. 20, pp. 203901–(1–4), 2001.

[154] S. Coen, A. H. L. Chau, R. Leonhardt, J. Harvey, J. Knight, W. Wadsworth, and P. Russell, "Supercontinuum generation by stimulated raman scattering and parametric four-wave mixing in photonic crystal fibers," *Journal of the Optical Society of America B*, vol. 19, no. 4, pp. 753–764, 2002.

[155] A. Yulin, D. Skryabin, and P. Russell, "Four-wave mixing of linear waves and solitons in fibers with higher-order dispersion," *Optics Letters*, vol. 29, no. 20, pp. 2411–2413, 2004.

[156] A. Bozolan, C. de Matos, C. Cordeiro, E. dos Santos, and J. Travers, "Supercontinuum generation in a water-core photonic crystal fiber," *Optics Express*, vol. 16, no. 13, pp. 9671–9676, 2008.

[157] J. Dudley, L. Provino, N. Grossard, H. Maillotte, R. Windeler, B. Eggleton, and S. Coen, "Supercontinuum generation in air silica microstructured fibers with nanosecond and femtosecond pulse pumping," *Journal of the Optical Society of America B*, vol. 19, no. 4, pp. 765–771, 2002.

[158] G. Genty, S. Coen, and J. Dudley, "Fiber supercontinuum sources (invited)," *Journal of the Optical Society of America B*, vol. 24, no. 8, pp. 1771–1785, 2007.

[159] K. Hilligsoe, T. Andersen, H. Paulsen, C. Nielsen, K. Molmer, S. Keiding, R. Kristiansen, K. Hansen, and J. Larsen, "Supercontinuum generation in a photonic crystal fiber with two zero dispersion wavelengths," *Optics Express*, vol. 12, no. 6, pp. 1045–1054, 2004.

[160] J. Knight and D. Skryabin, "Nonlinear waveguide optics and photonic crystal fibers," *Optics Express*, vol. 15, no. 23, pp. 15365–15376, 2007.

[161] F. Poletti and P. Horak, "Dynamics of femtosecond supercontinuum generation in multimode fibers," *Optics Express*, vol. 17, no. 8, pp. 6134–6147, 2009.

[162] W. Wadsworth, A. Ortigosa-Blanch, J. Knight, T. Birks, T. Man, and P. Russell, "Supercontinuum generation in photonic crystal fibers and optical fiber tapers: a novel light source," *Journal of the Optical Society of America B*, vol. 19, no. 9, pp. 2148–2155, 2002.

[163] J. Stone and J. Knight, "Visibly "white" light generation in uniform photonic crystal fibre using a microchip laser," *Optics Express*, vol. 16, no. 4, pp. 2670–2675, 2008.

[164] G. Humbert, J. Knight, G. Bouwmans, P. Russell, D. Williams, P. Roberts, and B. Mangan, "Hollow core photonic crystal fibers for beam delivery," *Optics Express*, vol. 12, no. 8, pp. 1477–1484, 2004.

[165] T. Murao, K. Saitoh, and M. Koshiba, "Detailed theoretical investigation of bending properties in solid-core photonic bandgap fibers," *Optics Express*, vol. 17, no. 9, pp. 7615–7629b, 2009.

[166] Y. Huang, Y. Xu, and A. Yariv, "Fabrication of functional microstructured optical fibers through a selective-filling technique," *Applied Physics Letters*, vol. 85, no. 22, pp. 5182–5184, 2004.

[167] L. Xiao, W. Jin, M. Demokan, H. Ho, Y. Hoo, and C. Zhao, "Fabrication of selective injection microstructured optical fibers with a conventional fusion splicer," *Optics Express*, vol. 13, no. 22, pp. 9014–9022, 2005.

[168] C. Martelli, J. Canning, K. Lyytikainen, and N. Groothoff, "Water-core fresnel fiber," *Optics Express*, vol. 13, no. 10, pp. 3890–3895, 2005.

[169] W. Young, "Analysis of capillary flows in non-uniform cross-sectional capillaries," *Colloids and Surfaces A: Physicochemical and Engineering Aspects*, vol. 234, pp. 123–128, 2004.

[170] M. Apel-Paz and A. Marmur, "Spreading of liquids on rough surfaces," *Colloids and Surfaces A: Physicochemical and Engineering Aspects*, vol. 146, pp. 273–279, 1999.

[171] Y. Gu, D. Li, and P. Cheng, "A novel contact angle measurement technique by analysis of capillary rise profile around a cylinder (acrpac)," *Colloids and Surfaces A: Physicochemical and Engineering Aspects*, vol. 122, pp. 135–149, 1997.

[172] K. Trumble, "Spontaneous infiltration on non-cylindrical porosity: close-packed spheres," *Acta Mater*, vol. 46, no. 7, pp. 2363–2367, 1998.

[173] B. Law, "Wetting, absorption and surface critical phenomena," *Progress in Surface Science*, vol. 66, pp. 159–216, 2001.

[174] T. Ransohof and C. Radke, "Laminar flow of a wetting liquid along the corners of a predominantly gas-occupied noncircular pore," *Journal of Colloid and Interface Science*, vol. 121, no. 2, pp. 392–401, 1987.

[175] H. Nakanishi and M. Fisher, "Multicriticality of wetting,prewetting and surface transitions," *Physical Review Letters*, vol. 49, no. 21, pp. 1565–1568, 1982.

[176] L. Horan, G.Khara, M. Rutowska, A. Ellis, and F. G. Gunning *Proceedings of SPIE, 21st International Conference on Optical Fibers Sensors*, 2011.

[177] M. Bosh, A. Sanchez, F. Rojas, and C. Ojeda, "Recent development in optical fiber biosensors," *Sensors*, vol. 7, pp. 797–859, 2007.

[178] T. Euser, M. Garbos, J. Chen, and P. Russell, "Precise balancing of viscous and radiation forces on a particle in liquid-filled photonic bandgap fiber," *Optics Letters*, vol. 34, no. 23, pp. 3674–3676, 2009.

[179] S. Afshar, S. Warren-Smith, and T. Monro, "Enhancement of fluorescence-based sensing using microstructure optical fibres," *Optics Express*, vol. 15, no. 26, pp. 17891–17901, 2007.

[180] Y. Ruan, E. Schartner, H. Ebendorff-Heidepriem, P. Hoffmann, and T. Monro, "Detection of quantum-dot labeled proteins using soft glass microstructured optical fibers," *Optics Express*, vol. 15, no. 26, pp. 17819–17826, 2007.

[181] D. Yong, X. Yu, C. Chan, Y. Zhang, and P. Shum, "Photonic crystal fiber integrated microfluidic chip for highly sensitive real-time chemical sensing," *Proceedings of SPIE, 21th International Conference on Optical Fibers Sensors*, vol. 7753, p. 775343, 2011.

[182] E. Schartner, R. White, S. Warren-Smith, and T. Monro, "Practical sensitive fluorescence sensing with microstructured fibers," *Proceedings of SPIE, 20th International Conference on Optical Fibers Sensors*, vol. 7503, p. 7503X, 2009.

[183] J. Ye, M. Myaing, T. Norris, T. Thomas, and J. Baker, "Biosensing based on two-photon fluorescence measurements through optical fibers," *Optics Letters*, vol. 27, no. 16, pp. 1412–1414, 2002.

[184] L. Rindorf, J. Jensen, M. Dufva, L. Pedersen, P. Hoiby, and O. Bang, "Photonic crystal fiber long-period gratings for biochemical sensing," *Optics Express*, vol. 14, no. 18, pp. 8224–8231, 2006.

[185] L. Rindorf, P. Hoiby, J. Jensen, L. Pedersen, O. Bang, and O. Geschke, "Towards biochips using microstructured optical fiber sensors," *Analytical and Bioanalytical Chemistry*, vol. 385, no. 8, pp. 1370–1375, 2006.

[186] A. Hoffman, "Hydrogels for biomedical applications," *Annals of the New York Academy of Sciences*, vol. 944, no. 1, pp. 62–73, 2001.

[187] J. Deng, Q. He, Z. Wu, and W. Yang, "Using glycidyl methacrylate as cross-linking agent to prepare thermosensitive hydrogels by a novel one-step method," *Journal of Polymer Science Part A: Polymer Chemistry*, vol. 46, no. 6, pp. 2193–2201, 2008.

[188] J. Debs, H. Ebendorff-Heidepriem, J. Quinton, and T. Monro, "A fundamental study into the surface functionalization of soft glass microstructured optical fibers via silane coupling agents," *Journal of Lightwave Technology*, vol. 27, no. 5, pp. 576–582, 2009.

[189] T. Forster, C. Strohhofer, K. Bock, P. Kasak, M. Danko, Z. Kronekova, T. Nedelcev, I. Krupa, and I. Lacik, "Biosensors for calcium based on a hydrogel optical waveguide with integrated sensor proteins," *Proceedings of IEEE, International Conference on Solid-State Sensors, Actuators, and Microsystems*, vol. T3P.085, pp. 1218–1221, 2009.

[190] K. Murthy and N. Ravi, "Hydrogels as potential probes for investigating the mechanism of lenticular presbyopia," *Current Eye Reasearch*, vol. 22, no. 5, pp. 384–393, 2001.

[191] S. Morel, *Optical properties of Pure Water and Pure Sea Water*. Optical Aspects of Oceanography, N. G. Jerlov and E. S. Nielson, 1974.

[192] Y. Wang, X. Tan, W. Jin, S. Liu, D. Ying, and H. Lai, "Improved bending property of half-filled photonic crystal fiber," *Optics Express*, vol. 18, no. 12, pp. 12197–12202, 2010.

[193] D. Walker, "A fluorescence technique for measurement of concentration in mixing liquids," *Journal Physics E: Scientific Instruments*, vol. 20, pp. 217–224, 1987.

[194] F. Helmchen and W. Denk, "Deep tissue two-photon microscopy," *Nature Methods*, vol. 2, no. 12, pp. 932–940, 2005.

[195] M. Rutowska, F. Kivlehan, E. Moore, D. Brennan, P. Galvin, and F. G. Gunning, "Integration of a 3d hydrogel matrix within a hollow core photonic crystal fibre for dna probe immobilization," *Measurement Science and Technology*, vol. 21, no. 9, p. 094016, 2010.

[196] M. Rutowska, J. Lu, F. G. Gunning, and A. Ellis, "Dna probe detection within 3d hydrogel matrix in a hollow-core photonic crystal fibre," *Proceedigs of SPIE, 21st Conference on Optical Fiber Sensors,*, vol. 7753-417, 2011.

[197] A. Webb, F. Poletti, D. Richardson, and J. Sahu, "Suspended-core holey fiber for evenescent-field sensing," *Optical Engineering Letters*, vol. 46, no. 1, pp. 010503–(1–3), 2007.

[198] S. Warren-Smith, S. A. V, and T. Monro, "Theoretical study of liquid-immersed exposed-core microstructured optical fibres for sensing," *Optics Express*, vol. 16, no. 12, pp. 9034–9044, 2008.

[199] M. Rutowska, F. Kivlehan, E. Moore, D. Brennan, P. Galvin, and F. G. Gunning, "Dna probe immobilisation using 3d hydrogel matrix in a hollow core photonic crystal fibre," *Proceedings of SPIE, 20th International Conference on Optical Fiber Sensors*, no. PDP 08, 2009.

[200] T. Euser, J. Chen, N. Farrer, M. Scharrer, P. Sadler, and P. Russell, "Quantitative broadband chemical sensing in air-suspended-core fibers," *Proceedings of IEEE, Conference on Lasers and Electro-Optics (CLEO), OSA*, vol. CMZ6, 2008.

[201] M. Rutowska, F. G. Gunning, W. Urbanczyk, and A. Ellis, "Dna immobilisation and hydrogel matrix formation in suspended-core optical fibre," *Proceedings of IEEE, Conference on Lasers and Electro-Optics (CLEO Europe)*, vol. CH4.2, 2011.

[202] B. Foultier, L. Moreno-Hagelsieb, D. Flandre, and J. Remacle, "Comparison of dna detection methods using nanoparticles and silver enhacement," *IEE Proceedings Nanobiotechnology*, vol. 152, no. 1, pp. 3–12, 2005.

[203] W. Krysicki and L. Wlodarski, *Analiza matematyczna w zadaniach, II*. Wydawnictwo Naukowe PWN, 1994.